

THE ELASTIC SCATTERING OF
DEUTERONS BY Li^7

Thesis by
James L. C. Ford, Jr.

In Partial Fulfillment of the Requirements
For the Degree of
Doctor of Philosophy

California Institute of Technology
Pasadena, California
1962

ACKNOWLEDGMENTS

The author wishes to express his gratitude to the members of the professional and technical staffs of the Kellogg Radiation Laboratory for their assistance and guidance during the course of this experiment. In particular, the supervision, advice, and patience of Professor C. A. Barnes have been appreciated. The author is also indebted to Professors R. F. Christy, W. A. Fowler, R. W. Kavanagh, T. Lauritsen, H. A. Weidenmuller, and W. Whaling for helpful discussions and advice concerning many aspects of this work.

The aid of Mrs. B. A. Zimmerman in the programming and operation of the electronic computer used for many of the calculations is gratefully acknowledged. Thanks are extended for the financial assistance furnished by the California Institute of Technology by means of Institute Tuition Scholarships. The experimental work was supported in part by the joint program of the Office of Naval Research and the U. S. Atomic Energy Commission.

ABSTRACT

The elastic scattering of deuterons by lithium-7 nuclei has been investigated in the energy region from 0.400 to 1.800 Mev. Three excitation functions, and twenty angular distributions have been measured in the energy range studied. The scattering cross sections tend to be lower than the Rutherford value below about 0.850 Mev and then rise to values several times the Rutherford value for higher energies. A prominent anomaly occurs in the scattering cross section near one Mev where the reaction cross sections also show resonance, while there is no obvious anomaly corresponding to the reaction resonances near 0.800 Mev.

The entire energy region investigated shows evidence of many broad overlapping energy levels in the compound nucleus. It was therefore not possible to make a detailed analysis of the elastic scattering over the entire region, from which level parameters might have been obtained. An s-wave analysis provides an adequate fitting of the angular distributions up to about one Mev, and the relatively sharp anomaly near one Mev appears to be due to p-wave deuterons.

TABLE OF CONTENTS

| <u>PART</u> | <u>TITLE</u> | <u>PAGE</u> |
|-------------|---|-------------|
| I. | INTRODUCTION | 1 |
| II. | EXPERIMENTAL ANALYSIS | 7 |
| | 1. General Discussion | 7 |
| | 2. Particle Detection Equipment | 8 |
| | 3. The Electrostatic Analyzer Calibration | 12 |
| | 4. The Magnetic Spectrometer Calibration | 12 |
| | 5. The Magnetic Spectrometer Solid Angle Calibration | 14 |
| III. | THE SCATTERING CROSS SECTION MEASUREMENT | 17 |
| | 1. Thick Target Calculations | 17 |
| | 2. Experimental Procedure | 23 |
| | 3. Target Preparation | 28 |
| | 4. Corrections to the Experimental Data | 30 |
| | 5. Target Contamination | 34 |
| | 6. Error Analysis | 38 |
| | 7. Summary of the Experimental Data | 40 |
| IV. | THEORY | 42 |
| | 1. General Formulae | 42 |
| | 2. Broad Level Analysis | 48 |
| | 3. Narrow Level Analysis | 52 |
| | 4. Application of the Theoretical Expressions to Li ⁷ (d, d) Scattering | 55 |
| | (a) General Discussion | 55 |
| | (b) Analysis Procedure | 57 |
| | (c) Conclusions | 63 |
| | APPENDIX I: Thick Target Yield for a Non-Uniform Target | 65 |
| | APPENDIX II: Sample Calculations of the Elastic Scattering Differential Cross Section from Experimental Thick Target Data | 70 |
| | REFERENCES | 74 |
| | TABLES | 76 |
| | FIGURES | 79 |

I. INTRODUCTION

One of the most fruitful techniques for obtaining information concerning the properties of excited states in nuclei has been that of elastic scattering. This is due to the interference between the amplitudes for Rutherford and nuclear scattering which, in principle, allows the phase and magnitude of the nuclear amplitude to be determined since the Coulomb amplitude is known. A large amount of experimental data has been accumulated concerning the properties of excited levels from neutron, proton, and alpha-particle scattering.

The scattering of deuterons, however, has mainly been studied at energies at which optical model parameters could be obtained. In view of the successful use of proton, neutron, and alpha-particle scattering at low energies to obtain level parameters, it might be hoped that deuteron scattering in the low energy region would similarly yield useful information concerning nuclear levels.

The observation of resonant structure corresponding to discrete states would in itself be interesting due to the high excitation energy of the compound levels formed in deuteron bombardment. These excitation energies range from nine to about twenty Mev for most light nuclei. At the time the present experiment was begun no previously published work on the elastic scattering of deuterons of energy below 2 Mev was available for target nuclei other than the isotopes of hydrogen and helium.

Reactions produced by deuterons form one of the most interesting and informative classes of reactions available to the experimenter, and

presented the first case of an observed and recognized direct reaction. The low binding energy of the deuteron which produces these interesting reactions might be expected to produce anomalous features in the elastic scattering as well. In addition, the diffuse charge distribution of the deuteron and its polarizability may cause the scattering to deviate from that given by the Rutherford cross section (French and Goldberger 1952; Guth 1960; Morinigo 1961a). Further, the fact that deuteron reactions are very prolific might be expected to affect the scattering data strongly due to the unitarity of the collision matrix (Morinigo 1961b).

Since the present experiment was undertaken a paper dealing with the elastic scattering of deuterons by C^{12} , from 0.500 Mev to 2.00 Mev, has appeared (Kashy et al. 1960). Relatively sharp resonant structure was observed, and the data analysis was performed by use of dispersion theory. The analysis displayed no details resulting from the deuteron structure. *

In the present experiment the elastic scattering of deuterons from lithium-7 was studied to investigate the possible presence of the above effects, as well as to attempt to obtain information concerning the excited states formed in the compound nucleus, Be^9 . Below 2 Mev, the deuteron bombardment of lithium-7 can proceed through states in Be^9 with excitation energies from 16.69 to 18.23 Mev, by means of the following reactions:

* The elastic scattering of deuterons by Be^9 , under investigation at this laboratory by James Renken when the present experiment was conducted, shows no resonant structure below 2 Mev.



In the region below 2 Mev, the integrated (d, p) cross section indicates resonances near 0.8, 1.0, and 2.0 Mev (Baggett and Bame 1952; Bashkin 1954; Kavanagh 1960; Sellschop 1960). The very distinct level at 1.4 Mev observed by Sellschop (1960) is only slightly discernible in the data of Baggett and Bame (1952), while no level is apparent at this energy in the measurements of Bashkin (1954) or Kavanagh (1960). The values of the integrated cross section as measured by the various observers are not in good agreement, and neither are the quoted positions of the resonances.

Angular distributions have been measured for the (d, p) reaction by Sellschop (1960). These angular distributions show unexpectedly good stripping patterns at all energies, including the regions of the 1.0 and 1.4 Mev resonances.

The deuteron bombardment of Li^7 can produce two alpha-particles and a neutron by means of the three reactions 4, 5, and 6. The reactions can be distinguished by means of the energy distribution of the reaction products. The $\text{Li}^7(d, \alpha)\text{He}^5$ reaction produces a monoenergetic alpha-particle group corresponding to the ground state of He^5 ,

and a neutron continuum. Reaction 5 results in broad neutron groups due to the excited states of Be^8 , as well as an alpha-particle continuum.

The angular distribution of the alpha-particles from the $\text{Li}^7(d, \alpha)\text{He}^5$ reaction has been measured by Riviere and Treacy (1957) at 0.900 Mev, and found to be isotropic to within 2% indicating formation by s-wave deuterons. The angular correlation, at the same energy, of the ground state alpha-particles with the alpha-particles from the He^5 breakup indicates $J = 5/2^-$ for the state of Be^9 in question (Riviere 1956/57). At a bombarding energy of 0.160 Mev, an angular correlation measurement between the ground state alpha-particles and the neutrons from the He^5 breakup indicates that $J = 3/2^-$ for the state concerned (Farley and White 1957). At 0.900 Mev reactions 5 and 6 are responsible for less than 10% of the disintegrations (Riviere 1956/57).

The measured (d, n) excitation functions include the neutron yields from the three neutron producing reactions 4, 5, and 6. This composite (d, n) cross section has been measured at 90° by Baggett and Bame (1952), and in the forward direction by Slattery et al. (1957). Resonances were observed near 0.7, 1.0, and 1.8 Mev. Angular distributions of the neutron groups corresponding to the various excited levels in Be^8 have been also measured (Catala et al. 1958; Trail 1956). But as the reaction $\text{Li}^7(d, n)\text{Be}^8$ appears to contribute only a small portion of the neutrons observed below 1 Mev (Riviere 1956/57), the contribution of the neutron producing reactions to the total reaction cross section cannot be determined very well from the published data.

The $\text{Li}^7(d, t)$ cross section rises steeply from the threshold to

2.4 Mev, and then continues to rise more slowly to at least 4.1 Mev. It has been suggested that the initial steep ascent may at least partially be due to a level in Be^9 corresponding to a deuteron bombarding energy of about 2 Mev (Macklin and Banta 1955).

Further information concerning the excited states in Be^9 in question has been obtained from the scattering of 40 Mev electrons by Be^9 reported by Barber et al. (1960). A level in Be^9 is observed at an excitation energy of 16.9 ± 0.4 Mev. However, no decision concerning the parameters of this level can be made from the data. An indication of a level in Be^9 at an excitation energy of 17.5 Mev is also observed in the inelastic proton scattering from Be^9 measured by Benveniste et al. (1956).

In summary, therefore, the reaction data indicates resonances at incident deuteron energies near 0.8, 1.0, and 1.8 Mev, whose widths are estimated as 200, 50, and 300 kev, respectively (Ajzenberg-Selove and Lauritsen 1959). These resonances correspond to excited levels in Be^9 at excitation energies of approximately 17.3, 17.5, and 18.1 Mev. There is less positive evidence of a resonance at 1.4 Mev deuteron energy. These levels in Be^9 , and some of the observed cross sections are shown in figure 1 (Ajzenberg-Selove and Lauritsen 1959).

The values of the spins and parities of these levels are unknown, except that there is a suggestion that the 0.8 Mev level may be formed by s-wave deuterons. Further, insufficient information is available even to allow an accurate value of the total reaction cross section to be determined. It was hoped that the present experiment would yield additional information concerning the existence, resonant energies and other

parameters of the levels in this energy region, as well as possibly showing some indications of new effects due to the loosely bound nature of the deuteron.

II. EXPERIMENTAL APPARATUS

1. General Discussion

The Kellogg Radiation Laboratory 1.8-Mv electrostatic generator was used to accelerate the charged particles used in the present experiment. This machine and its auxiliary analyzing equipment and scattering chamber have been described previously (Fowler et al. 1947; Milne 1953; Mozer 1956; Snyder et al. 1950; Wartens 1953).

After being produced in the high voltage terminal of the machine by an r-f ion source and accelerated through an adjustable potential difference, the various mass components of the ion beam are separated by a cross field magnet. In addition to the H^+ and D^+ beams usually employed in nuclear investigations the HH^+ and DD^+ beams were also used in order to reach the lower energies covered in the present work. The desired mass beam then enters, and is deflected by, an 80° -electrostatic analyzer. A horizontal slit system at the exit of the analyzer not only regulates the generator voltage, but also, in conjunction with the entrance slits of the analyzer, defines the beam energy to within about 0.2%.

Upon entering the scattering chamber the beam is incident upon the target, and the total quantity of charge collected is determined by discharging a capacitor whose voltage is set at a known value by a bank of mercury cells. When the capacitor is discharged the beam is deflected off the target by a magnet, and the scalers stopped. In order to insure accurate charge collection it is necessary to avoid loss or collection of secondary electrons produced in the target and slit systems. Therefore,

the target was raised to a potential of 300 volts above ground, and a screen 300 volts below ground was placed at the entrance to the scattering chamber.

The particles emerging from the target were analyzed by a high resolution double-focusing magnetic spectrometer. Since the beam enters 10° above the horizontal and exits 10° below the horizontal, the laboratory scattering angle can be set at any angle from 0° to 160° . The present magnet is able to deflect protons of energies up to about 1.8 Mev, or deuterons up to about 0.9 Mev. The magnetically analyzed reaction products were then detected at the focal plane of the spectrometer.

2. Particle Detection Equipment

Detection apparatus with good energy resolution was necessary in order to perform the present experiment. The bombardment of lithium by deuterons produces a large number of different reaction products. Since the magnetic spectrometer selects particles with a given momentum to charge ratio, particles with several different masses and charges will be passed by the identical magnetic field. For deuterons of a given energy, E , protons and doubly-charged alpha-particles of energy, $2E$, singly charged alpha-particles of energy, $\frac{1}{2} E$, and singly charged tritons and helium-three particles of energy, $\frac{2}{3} E$, will be detected at the same magnet setting. The alpha-particle continua from the Li^7 reactions, and the (d,p), (d,t), and (d,He³) reactions with Li^6 , will produce particles, at some depth in the thick natural lithium target, of the required energy to pass through

the magnet at nearly all bombarding energies, and these particles must be distinguished from the elastic deuteron group.

In addition the large neutron background produced in the deuteron bombardment of lithium requires a detector which is insensitive to neutrons and to neutron capture gamma-radiation. The above two problems are made critical by the low energy of the elastically scattered deuterons due to the large center-of-mass motion resulting from lithium plus deuteron reactions. If the relation between the incident and scattered particle energies is written as

$$E_2 = \alpha E_1 \tag{1}$$

then for $\theta_{c.m.}$ between 90° and 160° , α varies from 0.6535 to 0.3276, resulting in scattered particles of only a few hundred kev for incident energies less than 1 Mev.

The detector in use with the spectrometer when the experiment was begun was a 0.008-inch Cesium Iodide scintillator which proved to be unsatisfactory. A 0.002-inch Cesium Iodide crystal improved the neutron and gamma-ray backgrounds but failed to resolve the various particle groups.

The advent of solid state counters with their high resolution, linearity of response, and low neutron and gamma-ray sensitivity presented a solution to the problem. A gold-germanium surface barrier counter, constructed in the Kellogg Radiation Laboratory by E. M. Nordberg, appeared to have sufficient resolution to be applicable. However, as this counter had to be operated at liquid nitrogen temperatures

in order to reduce thermal noise, it proved to be a sink for N^{13} produced by deuteron bombardment of carbon throughout the accelerator. The positron decay of the N^{13} produced a band of irregularly-shaped, low pulses as the β -particles passed through the counter depletion region at various angles. Upon turning off the electrostatic generator the 10 minute half-life of the N^{13} could be observed in the decrease of the counting rate due to these pulses. This problem made the clear separation of the deuteron pulses impossible below a bombarding energy of one Mev.

A silicon n-p diffused junction counter was then obtained from the Hughes Aircraft Corporation* and as it could be used at room temperature, the above difficulty was eliminated. The solid state counter was approximately 3/16 inches square, and so mounted that it could be easily exchanged with other counters used with the magnetic spectrometer. The resolution of the counter was sufficient to resolve the various particle groups detected and was of the order of 7% at 0.657 Mev (figure 2), and 20% at 0.171 Mev (figure 3). As the width of the particle group is mainly due to the counter and electronic noise, the above values for the resolution correspond to a resolution of the order of 1% for alpha-particles from the decay of Po^{210} , an alpha-particle source which is often used as a test of the resolution of solid state counters. This counter was used for a period of over two years with satisfactory operation. Occasionally after being in the vacuum system for a number of weeks the counter would become noisy; however, after being exposed

*Through the courtesy of Dr. James W. Mayer.

to air for a day or so its original properties would be restored. The only noticeable sign of irreversible deterioration of the counter over the length of the experiment was a steady decrease in the maximum bias which could be applied before a prohibitive amount of noise was produced. When the counter was first obtained 45 V bias could be applied without a significant contribution to the noise, while at the end of the experiment only 3 V bias could be used. This effect is probably due to the deterioration of the exposed edges of the counter.

In order to detect the deuterons of a few hundred kilovolts energy or less, produced at many bombarding energies and angles in the experiment, the noise level of the associated electronics had to be reduced as much as possible. A charge integrating pre-amplifier was used in which the filament voltages were produced by a d-c power supply. This plus the use of noise filters on all power inputs to the electronics served to reduce the electronic noise level to that corresponding to about 0.1 Mev particles. It was then possible to distinguish 0.126 Mev particles from the electronic noise (figure 3), while 0.170 Mev particles were well resolved from the noise (figure 3).

A conventional amplifier followed the pre-amplifier, and the deuteron pulses were then selected from the other particle groups by means of a differential discriminator and recorded on a scaler. An RIDL 100-channel pulse height analyzer was used to record many of the spectra, particularly at low energies, to determine the position and number of deuterons relative to the other particle groups, and also as a check on the bias settings of the differential discriminator.

3. The Electrostatic Analyzer Calibration

The voltage across the plates of an electrostatic analyzer determines the energy at which a particle of given charge, Z , follows the central orbit of the analyzer. By measuring a small fraction of this voltage with a potentiometer, the particle energy, E_{1B} , can be determined. The relation between E_{1B} and the potentiometer reading V_e in terms of the electrostatic analyzer constant, k_e , is

$$E_{1B} \approx Zk_e V_e \left(1 + \frac{E_{1B}}{2Mc^2} \right). \quad (1)$$

The second term in this expression is a relativistic correction.

The electrostatic analyzer constant is usually obtained by observing some reaction with a resonance or threshold occurring at an energy which has been accurately determined by an absolute measurement. The $Al^{27}(p, \gamma)Si^{28}$ resonance at 992.0 ± 0.5 kev (Marion 1961) was used to calibrate the electrostatic analyzer by means of a thick aluminum target evaporated onto a clean glass microscope slide. Further calibrations were made utilizing the $F^{19}(p, \alpha\gamma)O^{16}$ resonance taken as 871.7 kev. A thick CaF_2 target, as well as thin fluoride targets were used for the measurements. The gamma-rays were detected by a sodium iodide crystal and photomultiplier.

Including the correction for the target potential an average value of 1.0036 ± 0.0006 Mev/decivolt was obtained for the electrostatic analyzer constant.

4. The Magnetic Spectrometer Calibration

The magnetic field of the spectrometer was measured, in the

region adjacent to the accepted particle orbits, by balancing a torque supplied by a quartz fibre against the torque on a current-carrying coil (Milne 1953). The field in this region was assumed to be proportional to the field in the region of the particle orbits. This assumption appears to be justified by the field measurements of Wartors (1953), and by the calibration of the fluxmeter against the electrostatic analyzer.

The current in the coil produces a voltage across a precision resistor which is measured by a potentiometer. The energy E_{20} of a particle of mass M and charge Z which traverses the spectrometer at a setting V_m measured in volts is then,

$$E_{20} \simeq \frac{Z^2 k_m M p}{M V_m^2} \left(1 - \frac{E_{20}}{2Mc^2} \right). \quad (1)$$

The magnetic spectrometer constant, k_m , can be determined by the elastic scattering of particles from targets of a given composition once the electrostatic analyzer has been calibrated. The relation between the energies of the scattered particle immediately before and after scattering is

$$E_2 = \alpha E_1, \quad (2)$$

where

$$\alpha^{1/2} = \frac{M_1}{M_1 + M_2} \cos \theta_L \pm \left[\left(\frac{M_1}{M_1 + M_2} \right)^2 \cos^2 \theta_L + \frac{M_2 - M_1}{M_1 + M_2} \right]^{1/2} \quad (3)$$

for the case of elastic scattering. The laboratory scattering angle is represented by θ_L , and M_1 and M_2 are the masses of the incident and target nuclei respectively. These relations can be used to obtain k_m in terms of the energy of the incident particle and the magnet

setting, including a correction for the target potential (Mozer 1956).

The elastic scattering of protons and deuterons from thick copper targets was used to calibrate the magnet. Profiles, which are defined as plots of the number of counts as a function of the spectrometer setting, are shown in figures 4 and 5 for protons scattered from a thick copper target. The mid-point of the rise of such a profile is determined by the energy of the particles scattered from the target surface. At the beginning of each experimental run a Cu(p, p) profile was taken and this gave a continual check on the magnet constant and solid angle. Further checks of k_m were obtained from the proton and deuteron scattering from lithium. The value of k_m obtained in a series of runs covering a period of about three months, and involving a wide range of energies and angles, had a mean and standard deviation of

$$k_m = 0.3844 \pm 0.0012 \text{ Mev-volt}^2 .$$

5. The Magnetic Spectrometer Solid Angle Calibration

The measurement of a cross section requires that the magnetic spectrometer solid angle be well determined. It is usual to scatter particles from a heavy nucleus such as copper and obtain the solid angle by assuming that the cross section is given accurately by the Rutherford cross section. However, to obtain accurate values for either the magnetic spectrometer constant or solid angle the scattering angle must be known. The technique of using a mask with a small aperture to scan the incoming and scattered beams was used to determine the scattering angle (Bardin 1961; Overley 1961a). The mask with a

0.040-inch aperture was mounted on a rotatable arm 0.750 inches in length. By scanning successively the scattering chamber entrance aperture and magnetic spectrometer entrance window, and noting the angular difference between the centroids of the two counting peaks, the scattering angle was determined at 80° and 160° as measured on the spectrometer protractor. The uncertainty in the determination of the position of the centroids was of the order of 15 minutes.

At 0° a second method was used to determine the correct spectrometer angle. The beam was passed directly into the spectrometer and observed on a quartz plate at the focal point of the magnet. The size of the beam spot was measured as the magnet was moved about the 0° setting on the spectrometer protractor. After inspecting the results of these three measurements, it was decided that a subtraction of 40 ± 30 minutes from the desired horizontal angle was necessary to obtain the proper setting of the spectrometer protractor corresponding to the required laboratory scattering angle. *

The elastic scattering of protons and deuterons from thick copper targets evaporated onto microscope slides was used to obtain the magnetic spectrometer solid angle. It was found that great care had to be taken in the cleaning of these slides, and in the vacuum evaporation of the copper, to insure that a uniform, clean target surface was produced. When the data was taken the beam current was kept at a low value to reduce electronic dead-time corrections, and prevent

*The help of James McCray on the first and James Renken in the second measurement is gratefully acknowledged.

the formation of blisters due to local heating by the beam. As the solid-state counter had to be interchanged frequently with a cesium-iodide crystal used in another experiment, the value of the solid angle was checked before most experimental runs, due to the difficulty in precisely positioning the solid-state counter. The Cu(p, p) profile taken at the beginning of each days run provided a measurement of the ratio of the spectrometer solid angle to the spectrometer resolution. An average value of 5.49×10^{-6} steradians was obtained for Ω_{sp}/R with a standard deviation of the order of 2% for measurements extending over the period of a typical series of experimental runs, or one month. The resolution of the magnet was determined by a slit of width 0.1394 inches located immediately in front of the counter.

III. THE SCATTERING CROSS SECTION MEASUREMENT

1. Thick Target Calculations

When a beam of particles is incident on a thick target, a continuum of reaction products is formed extending down in energy from those energies corresponding to reactions at the surface of the target, as seen in figure 4. A magnet of high resolution can be used to select those reaction products produced in a thin lamina whose width is determined by the resolution of the magnet and the kinematics of the reaction under study, and which is located at any desired depth in the target. Thus, many of the undesirable features involved in the use of thin targets, such as the uncertainty in the target thickness, can be avoided. However, the interpretation of the yield obtained from a thick target requires careful consideration of the energy relations involved, especially when data is taken at a considerable depth within the target. In addition the energy and angular variations over the magnetic spectrometer solid angle may need to be included, particularly if the target should be non-uniform.

The necessary relations to obtain cross sections from thick target yields have been discussed in a number of articles (Bardin 1961; Brown et al. 1951; Mozer 1956; Powers 1962). The following discussion will follow the notation and procedure of Bardin (1961), and will include only the salient features of the derivation.

The particles are incident on the target with an energy E_{1B} , and due to energy losses in the target have an energy E_1 at the midpoint of a lamina of thickness ds at a target depth s , measured along

the normal to the surface of the target. The particle produced in the reaction has an energy E_2 , which is then reduced by energy loss in the target to a value of E_{20} at the surface. The values for these energies are given in the laboratory system throughout the text, unless specified otherwise. The relation between these energies as determined by the target depth can be seen in figure 6. The yield from the lamina ds is then

$$Y = \frac{CV}{eZ} \int \sigma(E_1, \theta_L) \left| \frac{n}{\cos \theta_1} ds \right| d\Omega, \quad (1)$$

where the integration is carried over the solid angle subtended by the target at the magnet, and over the energy acceptance window of the magnet. The charge of the incident particle is eZ , and the beam discharges a capacitor C whose initial voltage is V . The term between the absolute value signs depending on θ_1 , the angle between the incident beam and s , and on n , the number of target nuclei per unit volume, is a function of the distribution of the elements comprising the target. The following discussion will assume a uniform target. The stopping power of the target material is defined by

$$\epsilon = - \frac{1}{N_s} \frac{dE}{dx} \quad (2)$$

where N_s is the number of stopping atoms per unit volume. The stopping relation provides two equations for s ,

$$\frac{1}{N_s} \int_{E_{1B}}^{E_1} \frac{dE}{\epsilon(E)} = - \frac{s}{\cos \theta_1} \quad (3)$$

and

$$\frac{1}{N_s} \int_{E_2}^{E_{20}} \frac{dE}{\epsilon(E)} = - \frac{s}{\cos \theta_2} \quad (4)$$

These equations assume that ϵ is not a function of s , or, in other words, that the target is uniform in composition. As E_{1B} is constant and $s = s(E_{1B}, E_{20})$ we have for the yield,

$$Y = \frac{CV}{eZ} \frac{n}{\cos \theta_1} \int \sigma(E_1, \theta_L) \left| \frac{\partial s}{\partial E_{20}} dE_{20} \right| d\Omega \quad (5)$$

By solving equations III-1.3 and III-1.4 for s , we can obtain two relations for $\partial s / \partial E_{20}$ which can be equated. Noting that

$$\frac{\partial E_2}{\partial E_{20}} = \frac{\partial E_2}{\partial E_1} \frac{\partial E_1}{\partial E_{20}}, \quad (6)$$

and holding the angular coordinates of the solid angle constant, we obtain

$$\frac{\partial E_1}{\partial E_{20}} = \frac{1}{\epsilon(E_{20}) \left[\frac{1}{\epsilon(E_2)} \frac{\partial E_2}{\partial E_1} + \frac{\cos \theta_1}{\cos \theta_2} \frac{1}{\epsilon(E_1)} \right]} \quad (7)$$

and

$$\frac{\partial s}{\partial E_{20}} = - \frac{\cos \theta_1}{N_s \epsilon(E_{20}) \left[\frac{\epsilon(E_1)}{\epsilon(E_2)} \frac{\partial E_2}{\partial E_1} + \frac{\cos \theta_1}{\cos \theta_2} \right]} \quad (8)$$

The yield is then

$$Y = \frac{CV}{eZ} \frac{n}{N_s} \int \frac{\sigma(E_1, \theta_L) dE_{20} d\Omega}{\epsilon(E_{20}) \left[\frac{\epsilon(E_1)}{\epsilon(E_2)} \frac{\partial E_2}{\partial E_1} + \frac{\cos \theta_1}{\cos \theta_2} \right]} \quad (9)$$

In integrating over the angle and energy acceptance windows of the magnet the transmission function of the magnet must be included. The magnet used in the present experiment was assumed to have a rectangular energy window, and a parabolic window in angle. In integrating over these windows, the fact that the surface of the target places an upper limit on the energy of the detected particles must be also remembered, and it is this condition which produces the shape of the face, or rise, of the profile.

If the magnet setting is located on the plateau of the profile, and if $\sigma(E_1, \theta_1)$, $\epsilon(E_1)$, $\epsilon(E_2)$, $\epsilon(E_{20})$, $\partial E_2 / \partial E_1$ and $\cos \theta_2$ vary slowly over the range of angles and energies accepted by the magnet, we can write

$$Y = \frac{CV}{eZ} \frac{n}{N_s} \frac{\overline{\sigma(E_1, \theta_L)} \Omega_{sp} \Delta E_{20}}{\left[\frac{\overline{\epsilon(E_1)}}{\overline{\epsilon(E_2)}} \frac{\partial E_2}{\partial E_1} + \frac{\cos \theta_1}{\cos \theta_2} \right] \overline{\epsilon(E_{20})}}, \quad (10)$$

where the bars indicate averages over the range of the variables as determined by the magnet window. The scattering cross section in the laboratory system was then obtained from the relation,

$$\sigma_L(E_1, \theta_L) = \frac{eZ}{2CV} \frac{N_s R}{n \Omega_{sp}} \frac{\epsilon(E_{20})}{E_{20}} \left[\frac{\cos \theta_1}{\cos \theta_2} + \frac{\epsilon(E_1)}{\epsilon(E_2)} \frac{\partial E_2}{\partial E_1} \right] Y, \quad (11)$$

where the magnetic spectrometer energy resolution is defined as

$$R = \frac{2E_{20}}{\Delta E_{20}}. \quad (12)$$

In the above equation the averages have been replaced by the values of E_1 and E_2 at the mid-point of the lamina, and by the values of E_{20} and θ_L at which the magnet is set.

Equation III-1.7 can be used to obtain approximate values for E_1 and E_2 .

$$E_1 \approx E_{1B} + \frac{E_{20} - E_{2B}}{\bar{\epsilon}(E_{20}) \left[\frac{1}{\bar{\epsilon}(E_2)} \frac{\partial E_2}{\partial E_1} + \frac{\cos \theta_1}{\cos \theta_2} \frac{1}{\bar{\epsilon}(E_1)} \right]} \quad (12)$$

where the bars now indicate averages of the stopping cross sections from the energy corresponding to reactions at the surface of the target to the energy corresponding to reactions occurring in the lamina.

These averages were approximated in the following manner:

$$E_1 \approx E_{1B} + \frac{E_{20} - E_{2B}}{\bar{\epsilon}\left(\frac{E_{20} + E_{2B}}{2}\right) \left[\frac{1}{\bar{\epsilon}\left(\frac{E_2 + E_{2B}}{2}\right)} \alpha + \frac{\cos \theta_1}{\cos \theta_2} \frac{1}{\bar{\epsilon}\left(\frac{E_1 + E_{1B}}{2}\right)} \right]} \quad (13)$$

where α is defined in II-4.2, and equals $\partial E_2 / \partial E_1$ for elastic scattering.

The other quantities appearing are defined by the equations

$$E_{2B} = \alpha E_{1B} \quad (14)$$

and

$$E_{20} = \alpha E_{10} \quad (15)$$

The energies E_{1B} and E_{20} are measured by the electrostatic analyzer and magnetic spectrometer respectively. In the present work the first approximations for E_1 and E_2 to be inserted in the above equation

were taken to be

$$E_1 \approx \frac{E_{10} + E_{1B}}{2} \quad (16)$$

and

$$E_2 \approx \frac{E_{20} + E_{2B}}{2} \quad (17)$$

The target was so positioned that θ_1 , the angle between the normal to the target and the incident beam, was equal to θ_2 , the angle between the normal and the scattered beam.

To transform the differential cross section to the center-of-mass coordinate system, the laboratory cross section is multiplied by the ratio of the laboratory to the center-of-mass solid angle which is

$$\frac{\Omega_L}{\Omega_{cm}} = \frac{[1 - X^2 \sin^2 \theta_L]^{1/2}}{[(1 - X^2 \sin^2 \theta_L)^{1/2} + X \cos \theta_L]^2} \quad (18)$$

The quantity X appearing in this equation is given by the relation

$$X^2 = \frac{M_1 M_2}{M_0 M_3} \left[1 + \frac{M_0 + M_1}{M_0} \frac{Q}{E_1} \right]^{-1} \quad (19)$$

where particle 1 incident on particle 0 produces particles 2 and 3.

The relation between the center-of-mass and laboratory angles is given by

$$\cot \theta_L = \frac{\frac{M_1}{M_0} + \cos \theta_{cm}}{\sin \theta_{cm}} \quad (20)$$

The geometry of the scattering chamber, in which the incoming and

scattered beams are 10° above and below the horizontal plane, respectively, results in the following relation between the laboratory angle and the angle in the horizontal plane:

$$\cos \theta_H = 1.031 \cos \theta_L - 0.0311. \quad (21)$$

The magnitude of the nuclear scattering occurring can most easily be seen by taking the ratio of the experimental differential cross section in the center-of-mass system to the Rutherford differential cross section,

$$\begin{aligned} \frac{d\sigma_R}{d\Omega} &= 1.296 \left[\frac{Z_1 Z_o}{E_1} \left(\frac{M_o + M_1}{M_o} \right) \csc^2 \frac{\theta_{cm}}{2} \right]^2 \times 10^{-3} \frac{\text{barns}}{\text{steradian}} \\ &= \frac{0.01932}{E_1^2 \sin^4 \frac{\theta_{cm}}{2}} \frac{\text{barns}}{\text{steradian}} \text{ for } \text{Li}^7(d, d), \quad (22) \end{aligned}$$

where E_1 is the reaction energy in Mev in the laboratory system.

2. Experimental Procedure

The experimental procedure was governed by the need to make a lithium target as free as possible of contaminants, to determine the nature and extent of any contaminants within it, and to obtain the maximum amount of data before the target became unusable due to the deterioration caused by oxidation under bombardment by the beam. The slit systems of the Van de Graaff accelerator were lined up by running a proton beam in the accelerator. The copper layer to be used as a backing for the lithium target was bombarded with protons, and the

Cu(p, p) profile was used as a check on the magnetic spectrometer solid angle and energy calibrations. The lithium target was then prepared as described in the next section. The proton beam was used to obtain a profile of the target including the carbon and oxygen peaks to determine the distribution and magnitude of possible contaminants. The deuteron beam was then extracted from the accelerator and a Li^7 (d, d) profile taken. This profile was used to determine a "following" point in the manner to be described shortly. Either excitation functions, which give the cross sections as a function of the energy, or angular distributions, which give the cross sections as a function of the scattering angle, were then taken.

Excitation functions were measured at the zeros of the second, third, and fourth Legendre Polynomials, at center-of-mass angles 90° , $125^\circ 16'$, and $140^\circ 46'$, respectively. Data were taken at intervals of 20 keV from below 0.400 MeV to 1.800 MeV, except at 90° where the fact that the magnet could only bend deuterons with energies less than 0.900 MeV required an incident deuteron energy below 1.400 MeV.

Instead of running a Li^7 (d, d) profile for each data point, the required magnet settings were computed for each angle and at 20 keV intervals in energy. Due to the large value of $\partial E_2/\partial\theta$ in the present experiment, the variation with angle of the energy of the particles scattered from the target surface results in a Li^7 (d, d) profile with a slowly rising edge. The point on the plateau of the profile at which the data were taken was therefore selected as 2% back in momentum from the mid-point of the profile rise, and it was this magnet setting that was

calculated as the "following" point. The $\text{Li}^7(d, d)$ profile taken at the beginning of a particular run was used to adjust this "following" point if such a correction seemed to be necessary. Changes in $\partial E_2/\partial\theta$ as the angle was varied, the varying effects of contaminants with energy, and variations in the magnet constant were among the effects which required small modifications of the "following" point for a particular run. Data were taken at points located the same percentage in momentum from the mid-point of the profile edge, as the incident beam energy was varied with constant magnet angle, by means of

$$V'_m = \left[\frac{E_{1B}}{E'_{1B}} \right]^{1/2} V_m. \quad (1)$$

If E_{1B} is held constant, while the spectrometer angle is changed, the "following" points are calculated from the relation

$$V'_m = \left[\frac{a}{a'} \right]^{1/2} V_m, \quad (2)$$

where again $E_2 = aE_1$. E_{1B} and V_m represent the beam energy and spectrometer setting corresponding to the point on the profile used to obtain the "following" point, while the primes represent these quantities after the change of energy or scattering angle.

The yield that is entered in equation III-1.11 for the cross section is the yield after correction for the background. This background is primarily due to particles scattered from contaminants within the target and electronic noise. The background was of the order of one to four percent of the total number of counts at the angles at which the excitation

functions were taken. A "following" point was also selected, for each run, in front of the $\text{Li}^7(d, d)$ profile step where the background had a typical value. The number of counts was then determined, at various energy intervals as the excitation function or angular distribution measurement proceeded, at magnet settings located the same percentage in momentum in front of the profile step by use of equations III-21 and 22. The energy interval selected between such measurements depended on how rapidly the background seemed to vary, but usually was 100 kev.

Angular distributions were taken at a total of 20 energies emphasizing the regions of suspected resonances. The angles at which data were obtained were so chosen as to give even intervals of $\cos \theta_{\text{cm}}$. The limit on the field obtainable in the magnetic spectrometer placed an increasingly severe restriction as the bombarding energy was increased, on how far forward in angle data could be taken. The surface condition of a thick target, particularly one which is so easily contaminated, as lithium, also limits how far forward data can be measured. The angular distribution points were generally determined at intervals of 0.1 in $\cos \theta_{\text{cm}}$ from +0.4 to -0.9, corresponding to spectrometer angles from $54^{\circ}1'$ to $150^{\circ}36'$. These distributions contain 13 angles below 1.200 Mev, 11 angles at 1.200, 1.300, and 1.350 Mev, and 10 angles at 1.400, 1.450, and 1.500 Mev.

As an angular distribution is a measurement of the scattering cross section at constant E_1 , as a function of the scattering angle, it is important that as the angle at which the cross section is measured is varied, that the bombarding energy or "following" point be also varied

to insure that the magnet selects a lamina within the target at all angles which corresponds to the desired reaction energy E_1 . It was decided that, in addition to keeping E_1 constant as the angle was varied, the location of the "following" point with respect to the profile edge would also be held constant. Equation III-1.13 written in the following simplified form can be used to satisfy these conditions,

$$E_1 \approx \frac{E_{20} + \left(\frac{\epsilon(E_2)}{\epsilon(E_1)} \right) E_{1B}}{a + \left(\frac{\epsilon(E_2)}{\epsilon(E_1)} \right)} \quad (3)$$

As the "following" point on the profile was taken 2% back in momentum, we have for the required bombarding energy at a given E_1 ,

$$E_{1B} = \frac{a + \left(\frac{\epsilon(E_2)}{\epsilon(E_1)} \right)}{\frac{a}{1.04} + \left(\frac{\epsilon(E_2)}{\epsilon(E_1)} \right)} E_1 \quad (4)$$

The detected energy E_{20} , and therefore the magnetic spectrometer setting is then determined by equation III-2.3. The settings of the electrostatic analyzer and magnetic spectrometer were then varied at each point on the angular distributions in accordance with the previous equations.

Most of the data points measured in these angular distributions include from 5000 to 10,000 counts, except at the most backward angles where the total number of counts was usually lower. The background yield generally varied from 1% to 4% of the total yield over the range of angles at which measurements were taken, and was always less than 10% of the yield.

3. Target Preparation

The preparation of the uncontaminated targets necessary to obtain accurate cross section measurements was a major source of difficulty in the present experiment. The problem of contaminants is a more serious one when deuterons are used as the incident particles than when protons are used for a number of reasons. The greater stopping power of the target for deuterons as compared to protons means that when the magnet setting is located a certain percentage back on the target profile the deuterons will be scattered from a layer of the target located nearer the surface of the target, where the contaminants are most likely to be, than for the case of proton scattering. The change in the target stopping cross section due to contaminants, which alters the measured yield, will also be larger when deuterons are used as the projectile. Further, as the center-of-mass motion is greater, the heavier the bombarding particle, scattered deuterons have a greater energy variation with angle than do protons. A wider range of laminae in the target can then scatter particles into the spectrometer when the incident particles are deuterons. Therefore, even when the magnet is set at a momentum corresponding to a point well back on the profile, deuterons from laminae close to the target surface can often still be detected. These effects of the contaminants in the targets are considered in more detail in the next section.

The bottom of the scattering chamber was fitted with a toroidal cold trap, through which the target could be dropped into position facing the furnace located below the cold trap. A diagram of the furnace-cold

trap apparatus appears in figure 7. With the use of this cold trap, which was kept filled with liquid nitrogen at all times, the vacuum attained a value of about 10^{-6} mm Hg. The evaporating furnace consisted of a block of carbon, into which a hole had been drilled to contain the lithium, wound with a wire heater. As it appeared that the most contaminant-free targets were produced when no part of the furnace or wire was heated more than was necessary to evaporate the lithium, molybdenum wire was used instead of tungsten as it was more easily wound tightly about the carbon furnace.

The furnace was carefully outgassed for about one hour, with the carbon heated to a bright orange color, until the pressure dropped to at least 2×10^{-6} mm Hg. The lithium was then cut under kerosene so that the bright metal was exposed, placed in the furnace, and the system was then usually pumped overnight. Natural lithium, consisting of 92.5% lithium-7, was employed as the target material.

The lithium was evaporated onto a section of a glass microscope slide on which a copper layer had been previously evaporated to help dissipate the heat caused by the deuteron bombardment. The target was held in a target holder which could be swung from side to side, to enable as much of the target to be utilized as possible, by means of a sliding rod passed into the scattering chamber through an O-ring. The target mounting was equipped with a protractor to determine the angle of the target to the beam, and with 14 reproducible vertical positions. The target holder was dropped into a cup in the bottom of the scattering chamber which positioned the target in front of the furnace.

At the beginning of the evaporation procedure the copper-plated glass slide was situated above the cold trap so that no lithium could be deposited upon it. The furnace heater current was slowly increased until lithium began to appear on the bottom of the scattering chamber. The target holder was then lowered into position facing the furnace, and the lithium target made. By evaporating at a low temperature for about half an hour the pressure could be kept below 2×10^{-6} mm of Hg, producing a target with a bright mirror surface. The evaporation was controlled by noting the furnace current applied and the elapsed time, and by observing the lithium deposited on the bottom of the chamber, since the target itself was unobservable during the evaporation. Targets produced with this procedure had a sufficiently low amount of contamination to be satisfactory at all bombarding energies except below about 0.4 Mev. The subsequent slow oxidation of the surface while in the target chamber required that a target not be kept longer than one day. The rapid buildup of carbon and oxygen when the target was bombarded necessitated the frequent change of target spots.

4. Corrections to the Experimental Data

The experimental data usually require a number of corrections besides the subtraction of the background. These corrections are related to the sensitivity of the analyzing, detecting, and scaling equipment to the type, energy, and number of particles scattered from the target. The magnitude of the corrections is usually small, except for a few extreme cases.

The dead-time of the electronic circuitry must be considered

when the magnitude of the beam current is selected. By observing the number of counts obtained as the beam current was varied, an electronic dead-time of 10^{-5} sec was determined. Over the period of the experiment the beam currents were kept sufficiently low so that the dead-time correction was $\leq 1\%$, except for the low energy scattering at forward angles from copper. The time for each current integration was nevertheless recorded, and the dead-time correction was calculated from the relation

$$N_T = \frac{N}{1 - N \frac{\tau}{t}}, \quad (1)$$

where τ is the dead-time, t the beam integration time, and N and N_T the observed and corrected yields respectively.

The dead-time of the 100-channel pulse height analyzer is about 4 times that of the decade scaler, so an increased correction was necessary when the multichannel analyzer was used to record the data. These corrections were usually a few percent. However, in obtaining Cu(d, d) data below 0.400 Mev corrections as large as 10% were necessary.

Charged particles may gain and lose electrons from the material through which they are passing. Therefore, when a scattered beam emerges from the target surface it frequently contains particles in a number of charge states. Those particles without the correct ratio of momentum to charge to traverse the magnet will not be detected. The ratio of the particles in the various charge states must be known in order to correct for this loss of particles. Charge equilibrium ratios

for beams emerging from a variety of solid materials have been investigated by Hall (1950) and Phillips (1955) and summarized by Allison (1958). Their data are shown in figure 8 as a function of the emergent deuteron energy. The original experiments were performed with proton beams, but as this is presumed to be a velocity-dependent effect, the data have been plotted at the equivalent deuteron energy. The ratio of the number of positively charged particles to the total number of particles in the emerging beam is shown in the figure. The ratio of the negatively charged particles to the total number of particles was also measured by Phillips and found to be less than or equal to $\sim 1\%$ for proton energies greater than 25 kev. Hall obtained the same charge equilibrium ratios for all materials measured except gold. However, Phillips observed different ratios for various materials, although identical equilibrium ratios for all surfaces after a length of time in the vacuum system. The values given by Phillips for old surfaces or "dirt" were generally used below deuteron energies of 0.400 Mev, while Hall's figures were used at higher energies. During the present experiment the charge exchange correction was often a significant one. A charge equilibrium ratio of 0.865 is expected for 0.400 Mev deuterons scattered at 90° in the center-of-mass system, while corrections as large as 30% were used at lower energies.

The scattering of charged particles will be further modified by the screening effects of the atomic electrons. This correction for a target of charge Z and incident protons has been given by Wenzel (1952) as

$$\frac{d\sigma/d\Omega}{d\sigma_R/d\Omega} = \left(1 - \frac{34Z^{7/5}}{E} \right), \quad (2)$$

where $\frac{d\sigma/d\Omega}{d\sigma_R/d\Omega}$ is the ratio of the observed scattering cross section to the Rutherford cross section, and E is the incident energy in the center-of-mass system expressed in ev. In the present experiment this correction was only of importance in the determination of the solid angle by means of scattering from copper.

The magnitude of the charge exchange and atomic screening corrections were checked by scattering deuterons from copper down to an incident energy of 150 kev. The ratio of the scattering cross section, after correction, to the Rutherford cross section is seen in figure 9. The average of the data shown is 1.003 with a standard deviation of about 3%. The dead-time of the 100-channel pulse height analyzer varied from about 3% to 10% while taking these low energy data. To within the accuracy of the experimental data, the values of the charge exchange and atomic screening corrections applied would seem to be adequate.

The elastic scattering of deuterons may be affected by the structure of the deuteron itself. The diffuse charge distribution of the deuteron results in different instantaneous radius vectors to the center-of-mass of the deuteron and to the proton. The radius vector of the center-of-mass is usually used in order to obtain the Coulomb scattering formula. A correction to the Rutherford scattering formula is then necessary as the positions of the center-of-mass and proton are non-coincident. Such a correction has been given by French et al. (1952). The magnitude of this

correction to the Rutherford cross section for the case of deuterons incident on lithium, was calculated. However, although an effect of about 4% near 2 Mev at the backward angles was calculated, the correction was less than 0.1% at 0.400 Mev. Therefore, this correction was not applied to the data.

5. Target Contamination

After making the corrections discussed in the last section to the experimental data, it was found that at low energies the measured scattering cross section was still less than the Rutherford cross section. At a bombarding energy of 0.400 Mev, the ratio of the scattering cross section to the Rutherford cross section varies from 0.92 to 0.69 as the scattering angle is changed from the most forward to the most backward angle at which data was taken. The failure of the cross section to approach the Rutherford value at low energies was extensively investigated.

The low energy scattering of deuterons from copper discussed previously indicates that this problem is probably not a detection problem, nor due to incorrect values for the charge exchange correction. Further, the stopping cross section for protons in lithium is known to within $\sim 3\%$ (Bader et al. 1956). The possibility of contaminants within the target reducing the yield must be considered as lithium is very chemically active. The $\text{Li}^7(p,p)$ profiles were used as a check on the target surface condition and on the amount of contaminants present. A sharply-rising edge of the profile, without an excess rounding off as the yield approaches the value on the plateau, was taken as indicating an acceptable target surface. Such a $\text{Li}^7(p,p)$ profile taken at an incident

proton energy of 0.401 Mev is shown in figure 10. The height of the oxygen and carbon peaks is strongly dependent on the incident energy as indicated by the profile of figure 11. The $\text{Li}^7(p, p)$ profiles gave a further check on the data taking procedure by allowing the measured cross section to be compared with previous experiments. Elastic scattering of protons by lithium-7 has been performed from 0.400 to 1.400 Mev by Warters (1953), and from 1.400 to 3.000 Mev by Malmberg (1956). Data taken during the present experiment at energies corresponding to the profiles in figures 10 and 11, as well as at the lowest energy reported in the previous work are shown plotted on the angular distributions, obtained by Warters, in figure 12. More recent determinations of the stopping cross sections have necessitated the lowering of Warter's data by 8.7% (Fowler 1960), and it is the corrected values which are shown in figure 12. It can be seen that the points taken in the present experiment appear to lie on the older angular distributions.

Profiles obtained from the elastic scattering of deuterons from lithium-7 are shown in figures 13, 14, and 15. The smaller slope of the rising edge of the profiles, as compared with those for proton scattering, is due to the larger center-of-mass motion resulting from deuteron bombardment. The larger center-of-mass motion produces a greater variation with angle of the energy of the scattered particle. For this reason a greater range of laminae within the target, including those nearer the surface, can scatter particles into the magnet when the incident particles are deuterons. However, the necessity of selecting a "following" point located in front of the Li^6 step on the plateau of the profile forces the

"following" point forward toward the Li^7 profile edge as the scattering angle is decreased. In addition the uncertainty as to the target smoothness, and the rapid increase in the size of the oxygen and carbon scattering peaks, as the scattering angle is reduced, also tend to make the data taken at very forward angles uncertain. Data were obtained, however, at 0.400 Mev down to a center-of-mass angle of 60° without any apparent increase in the ratio of the experimental to the Rutherford cross section. As the energy was reduced the ratio was observed to reach a maximum of about 0.85 somewhat below 0.400 Mev, and then slowly decrease to around 0.72 at 0.200 Mev for angles forward of 90° in the center-of-mass system.

In view of these results, the effect of the observed oxygen contamination on the yield of deuterons scattered from the lithium target was estimated. As the widths of the oxygen peaks measured were usually comparable to the magnet resolution, and as the oxygen distribution can be expected to be concentrated near the surface of the target, the sources of finite resolution of the magnet must be considered in obtaining the oxygen distribution and its effect. The computed distribution of oxygen throughout the target is therefore only an approximate one. The method used for including the sources of finite resolution in the yield calculations is given in Appendix I. While the oxygen peak calculated from the assumed oxygen distribution was about 11% lower than the measured peak in figure 10 used as the basis for the calculation, it was, nevertheless, fairly representative of measured oxygen peaks at the same energy and angle. A reduction in the $\text{Li}^7(d, d)$ yield of only a few percent at 0.400 Mev,

for a "following" point 4% back in energy, and a center-of-mass angle of 90° , was calculated using this oxygen distribution. However, a reduction in yield of about 20% at the same angle, at an incident energy of 0.300 Mev was computed. It is therefore felt that an oxygen contamination which produces a peak of the magnitude observed in figure 10 is capable of substantially reducing the $\text{Li}^7(d,d)$ yield for energies below 0.400 Mev.

In order to reduce the oxygen contamination, an effort was made to improve the vacuum within the scattering chamber. The chamber was carefully leak tested, the diffusion pump oil replaced, and various substances tried as getters. As there was evidence that the oxygen contamination was originally very small when the target was prepared, but then very rapidly built up as the target was bombarded, the effect of continuous evaporation of sodium, barium, and lithium on the walls of the scattering chamber during the target bombardment was investigated. However, neither the improvement of the scattering chamber vacuum by about a factor of five, nor the presence of the getters produced an appreciable change in either the oxygen or lithium yields.

As lithium is one of the lightest elements a thick target formed by a lithium compound is difficult to use. The profile step from the heavier element will precede, and be larger than, the step due to lithium. The possibility of using LiH as a target material was studied. Again, no appreciable improvement in the contamination problem was seen. In addition, the partial dissociation of the LiH , and difficulty in handling it made it an undesirable substance from which to make a large number of targets.

Above an incident energy of about 0.5 Mev the experimental data should be unaffected by target contamination. At lower energies it appears likely that the contaminants present have reduced the yields of scattered particles from the lithium below the correct values.

6. Error Analysis

The various sources of the estimated error in the measured scattering cross section, are tabulated in Table I. The total error is divided into two sections. That part of the error rising from fluctuations in the determination of quantities measured during the course of the experiment, and from the relative error of the stopping cross sections is given as the relative error. It is this quantity that is shown on the plots of the excitation functions and angular distributions. The additional error due to the normalization of the data is included with the relative error to obtain the absolute error. The figure given for all values of the error is the standard deviation.

A further explanation of the tabulated major errors may make their origin clearer.

Counting Statistics: The background Y_b is subtracted from the total yield Y to obtain the desired corrected yield Y_c . The error given as due to counting statistics is, therefore, $(Y+Y_b)^{1/2}/Y_c$. The total yield and background are functions of the incident particle energy and the scattering angle, but on the average produced an error of about 1 - 3%.

E_{20} : This error arises from the observed deviations of 0.3% from the average magnet calibration.

ϕ_L : The correction due to charge exchange was generally only significant for the case of $\text{Li}^7(d, d)$ scattering. The error in the ratio of positively charged to total number of particles has been taken as 3% at energies where ϕ is appreciably different from one, as given by Phillips (1955), and was assumed to enter the absolute error only.

Target Composition: The effect of unknown quantities of contaminants heavier than lithium on the yield of the elastically scattered deuterons is difficult to estimate. Based on the number of counts appearing at the foot of the lithium profile, the number of heavy atoms within the target was judged to be small. The uncertainty in yield due to contaminants was assumed to be of the order of 1% consistent with the effects calculated due to the oxygen contamination, for energies above 0.5 Mev.

$(\cos \theta_1 / \cos \theta_2) + \alpha[\epsilon(E_1) / \epsilon(E_2)]$: An error in this quantity, which appears in the equation for the differential cross section, can arise from uncertainties either in energy or in angle. The various determinations of the calibration of the magnetic spectrometer protractor, discussed in the section on the magnetic spectrometer solid angle calibration, had a spread of $\pm 0.5^\circ$. Therefore, all angles may be in error by as much as 0.5° . However, the method of normalizing the data by means of $\text{Cu}(p, p)$ scattering largely eliminates any error due to the angular dependence of $(\cos \theta_1 / \cos \theta_2) + \alpha[\epsilon(E_1) / \epsilon(E_2)]$. The uncertainties arising from the relative errors in the lithium and copper stopping cross sections are independent, however. The relative error of both stopping cross sections was assumed to be 2%.

$\epsilon(E_{20})$: The absolute error in the lithium and copper stopping cross sections was taken as 3% as determined by Bader et al. (1956).

Rutherford Cross Section for Cu: An error of 0.5° in the magnetic spectrometer protractor calibration introduces an error in the copper Rutherford cross section used to normalize the data, varying from 1% to 3% over the range of angles used.

Dead-time Correction: The correction for the electronic dead-time was appreciable only when copper was used as the target. The dead-time was assumed known to within 25%, introducing an uncertainty of 0.5% in the Cu(p, p) yield.

Combining the above sources of error the estimated relative error is about 3% over the range of energies and angles used in the present experiment. Over the same range the absolute error is of the order of 6%.

7. Summary of the Experimental Data

The excitation functions, measured at the zeros of the second, third, and fourth Legendre Polynomials, are shown in figure 16. The differential cross section is plotted as a function of the deuteron laboratory energy. There is an obvious anomaly near one Mev, but nothing conspicuous appears at either 0.800 or 1.400 Mev where resonances have been reported in the reaction data. The behavior of the cross sections near these energies, however, is consistent with broad levels in these regions. The indicated error in figure 16 is the relative error, while the arrows denote the energies at which angular distributions were taken.

The ratio of the scattering cross section to the Rutherford cross section is displayed in figure 17. As with the plots of the cross section, the anomaly near one Mev is the only prominent feature of the data, although at higher energies a great deal of non-Coulomb scattering is occurring which is consistent with broad levels in this region.

The angular distribution data is presented in Table II. In figure 18 are plotted the angular distributions passing over the region of 0.800 Mev where the first resonance is observed in the reaction data. The curves shown were obtained from the s-wave fit to the angular distributions discussed in the section on the theoretical analysis of the data.

The shapes of the 20 angular distributions taken are generally similar. Therefore, it was felt that plotting the angular distribution data as excitation functions, as in figures 19, 20, 21, and 22, would be more informative than plotting the separate angular distributions. In these figures a progressive modification of the excitation functions can be seen as the center-of-mass scattering angle is increased. The points for the angles at 90° , $125^\circ 16'$, and $140^\circ 46'$ were obtained from estimated curves of best fit to the points on figure 17. The entire set of data indicates significant deviations from the Rutherford cross section over the energy region investigated, but with a fairly sharp anomaly occurring only near one Mev.

IV. THEORY

1. General Formulae

Elastic scattering of charged particles from light nuclei in the low energy region often furnishes information concerning the properties of the excited levels of the compound nucleus. The analysis of such scattering data then attempts to determine a set of parameters of the compound states which reproduces the experimental cross sections, and is compatible with the reaction data. The theoretical expressions for the cross sections, into which the level parameters are inserted, have been fully described in the literature (Blatt and Biedenharn 1952; Christy 1956; Lane and Thomas 1958; Mozer 1956), and therefore only the relations required for an understanding of the analysis discussed in Section IV-4 will be included here. The definitions and notations used will primarily be those of Lane and Thomas (1958).

The incident particle and target nucleus can be considered to be in a state represented by the channel indices (a, l, s) . The internal states of excitation of the two nuclei and their types are given by a , and l is their relative orbital angular momentum. The channel spin s is obtained by vector addition of the intrinsic spins of the two nuclei, I_1 and I_2 ,

$$\vec{s} = \vec{I}_1 + \vec{I}_2 . \quad (1)$$

The total angular momentum is then given by coupling s and l ,

$$\vec{J} = \vec{s} + \vec{l} . \quad (2)$$

If the reaction products are described by (a', l', s') , the conser-

vation of angular momentum and its z-component give the following relations:

$$\vec{s} + \vec{l} = \vec{J} = \vec{s}' + \vec{l}' ,$$

and

(3)

$$m_s = M = m_s' + m_l' ,$$

since the z-axis is taken along the incident beam. The angular momentum conservation laws, and the conservation of parity then limit the complexity of the angular dependence of the cross section at any energy. If the incident beam and target nuclei are unpolarized, the differential cross section obtained by averaging over the initial, and summing over the final spin orientations is

$$\frac{d\sigma}{d\Omega} = \frac{1}{(2I_1+1)(2I_2+1)} \sum_{\substack{ss' \\ m_s m_s'}} \left| A_{a's'm_s',asm_s} \right|^2 . \quad (4)$$

The scattering amplitude, $A_{a's'm_s',asm_s}$, is given by

$$A_{a's'm_s',asm_s} = -f_c - \sum_{\substack{J M l \\ l' m_l'}} (s l m_s 0 | J M) (s' l' m_s' m_l' | J M) \\ \times f_{aa'll'ss'}^J Y_{l'}^{m_l'}(\theta, \phi) , \quad (5)$$

where

$$f_{aa'll'ss'}^J = -\frac{\sqrt{\pi}}{k} i(2l+1)^{1/2} T_{a'l's',als'}^J . \quad (6)$$

The quantity f_c , representing the amplitude for Coulomb scattering is, as defined by Christy (1956),

$$f_c = \sqrt{R} e^{i\xi}, \quad (7)$$

where R is the Rutherford scattering cross section given by equation III-1.22. The phase of the Coulomb amplitude is related to the center-of-mass scattering angle,

$$\xi = -\frac{Z_1 Z_2 e^2}{\hbar v} \ln \sin^2 \frac{\theta}{2}. \quad (8)$$

The matrix T , defined by Lane and Thomas (1958), has the following components:

$$T_{a'l's', als}^J = \delta_{a'l's', als} e^{2i\omega_{a'l'}} - U_{a's'l', asl}^J, \quad (9)$$

and

$$\omega_{al} = \sum_{n=1}^l \tan^{-1} \frac{Z_1 Z_2 e^2}{n\hbar v}. \quad (10)$$

The other quantities appearing in the expression for the scattering amplitudes are the Clebsch-Gordan coefficients, and k the wave number of the relative motion.

From the form of equations IV-1.4 and 1.5 it can be seen that while the different l -values that participate in the reaction can interfere, there is no interference between channels with different values of the channel spin or its z -component. Each matrix element of the scattering amplitude consists of a series of terms which are to be added coherently,

and which are then added incoherently to the terms of matrix elements with different initial or final channel spin configurations. For the case of elastic scattering of deuterons by lithium-7, a 12 x 12 matrix is obtained.

The sums over magnetic quantum numbers in the cross section equation can be eliminated by the technique described by Blatt and Biedenharn (1952). The differential cross section for the elastic scattering of charged particles can then be written in the following form (Overley 1961b):

$$\frac{d\sigma/d\Omega}{R} - 1 = \sum_L B_L \frac{P_L(\cos \theta)}{4k^2 R} + \sum_l (C_l \cos \xi + D_l \sin \xi) \frac{P_l(\cos \theta)}{k\sqrt{R}} \quad (11)$$

The angle-independent coefficient B_L is defined below and contains contributions from pure nuclear resonant scattering, potential scattering, and the interference between them. The interference between these nuclear scattering processes and the Coulomb scattering is given by the terms with the coefficients C_l and D_l . The coefficients depend on the elements of the T matrix in the following manner:

$$B_L = \sum_{ss'} (-1)^{s-s'} \sum_{\substack{J_1 J_2 \ell_1 \ell_2 \\ \ell_1' \ell_2'}} \frac{1}{(2I_1+1)(2I_2+1)} Z(\ell_1 J_1 \ell_2 J_2; sL) \times Z(\ell_1' J_1' \ell_2' J_2'; s'L) \left(T_{s'\ell_1', s\ell_1}^{J_1} \right) \left(T_{s'\ell_2', s\ell_2}^{J_2} \right)^*, \quad (12)$$

$$C_l = \sum_{J_s} \frac{2J+1}{(2I_1+1)(2I_2+1)} \operatorname{Im} T_{s_l, s_l}^J,$$

$$D_l = - \sum_{J_s} \frac{2J+1}{(2I_1+1)(2I_2+1)} \operatorname{Re} T_{s_l, s_l}^J.$$

The \bar{Z} -coefficients appearing in equations IV-1.12 are related to the Z -coefficients defined by Blatt and Biedenharn (1952) by a phase factor,

$$\bar{Z}(l_1 J_1 l_2 J_2; sL) = i^{l_1 - l_2 - L} Z(l_1 J_1 l_2 J_2; sL). \quad (13)$$

The expression for the differential elastic scattering cross section given in equation IV-1.11 is valid for any non-relativistic scattering mechanism involving two incident and two outgoing particles. The nature of the scattering force is contained in the collision matrix U , whose elements appear in equation IV-1.9. With the assumption that the scattering is produced by discrete levels of the compound nucleus, the single level approximation to the collision matrix is usually made. In this case, the elements of the collision matrix have the following form:

$$U_{s'l', s_l}^J = e^{i(\omega_l - \phi_l)} e^{i(\omega_{l'} - \phi_{l'})} \left\{ \delta_{s'l', s_l} + \frac{\Gamma_{s'l'd}^{J1/2} \Gamma_{s_l d}^{J1/2}}{\Gamma^J} (e^{2i\delta^J} - 1) \right\}. \quad (14)$$

This expression holds only when states of the same spin and parity do not appreciably overlap, although the quantities appearing in the expression can be so defined as to include the effect of distant levels of the same spin and parity. The interpretation of the quantity ϕ_l

contained in equation IV-1.14, for the case where the contribution of distant levels is not included, is the following:

$$\phi_l = \tan^{-1} \frac{F_l(ka)}{G_l(ka)} \quad (15)$$

Here the potential phase shift ϕ_l is obtained by evaluating the Coulomb wave functions at a radius a , of the order of the nuclear radius. The resonant phase shift is defined by the relation,

$$\delta^J = \tan^{-1} \frac{\Gamma^J}{2(E_R - E)} \quad (16)$$

where Γ^J is the level width, and $E_R = E_\lambda + \Delta_\lambda$, the sum of the characteristic energy of the level and the Thomas level shift. The partial width of the state for deuteron emission may be written in terms of the channel spin ratio,

$$\Gamma_{sld}^J = (a_{sl}^J)^2 \Gamma_{ld}^J, \quad (17)$$

where

$$\sum_s (a_{sl}^J)^2 = 1 \quad (18)$$

By means of equation IV-1.14 for the collision matrix the dependence of the scattering cross section on the level parameters is explicitly specified. The determination of a set of such parameters which will duplicate the energy and angular variations of the experimental cross sections is the goal of the analysis in the resonant region.

2. Broad Level Analysis

Although the sums over ℓ -values appearing in equation IV-1.11 in general are from 0 to infinity, in a practical case only a limited number of orbital angular momenta will be involved appreciably in the scattering process. The partial width of a level is related to the penetration factor by the following relation:

$$\Gamma_{\ell d}^J = \frac{2ka \gamma_{\ell d}^{J^2}}{F_{\ell}^2(ka) + G_{\ell}^2(ka)} \quad (1)$$

where $\gamma_{\ell d}^{J^2}$ is the reduced width of the compound state. In the low energy region the rapid decrease, with increasing orbital angular momentum, of the penetration factor,

$$P_{\ell} = \frac{ka}{F_{\ell}^2(ka) + G_{\ell}^2(ka)} \quad (2)$$

limits the number of ℓ values effectively participating in the scattering. The summation index L appearing in equation IV-1.11 is then also limited by the requirement that $L \leq 2\ell_{\max}$. Despite this limitation on the number of ℓ -values which need to be considered, the complexity of the expressions for the scattering cross section is such that it is difficult to determine the many level parameters involved from experiment, unless the reaction channels are energetically closed, or either or both of the nuclei involved have zero spins so that the collision matrix is simplified.

In cases where broad overlapping levels seem to be determining the form of the cross section, the most informative method of analyzing

the experimental data is by analysis of the angular distributions. In this type of analysis angular distributions are measured over the energy regions of suspected resonances. The number of angles which need to be included in such a distribution depends on the complexity of the scattering. The number of angle-dependent terms corresponding to pure s-wave scattering is three, to s- and p-wave scattering seven, and to s-, p- and d-wave scattering eleven. The determination of the coefficients of these angle-dependent terms in the differential cross section then requires at least as many angles in the angular distribution, and it was this fact that determined the number of angles chosen in the present experiment. The energy variation of these coefficients then furnishes further information on the level parameters involved.

However, the number of such angle-dependent terms, plus the difficulty in distinguishing between the terms arising from the interference with the Coulomb amplitude and those due to purely nuclear scattering, makes the determination of the coefficients of the angle-dependent terms generally unreliable except in the case of s-wave scattering. For this reason many angular distribution analyses of cross sections involving broad overlapping structure have been limited to a consideration of s-waves. The equation for pure s-wave scattering can be written (Christy 1956),

$$\frac{d\sigma/d\Omega}{R} - 1 = \left[\frac{\sin \xi}{k\sqrt{R}} - \frac{1}{2k^2R} \right] (X-1) - \frac{\cos \xi}{k\sqrt{R}} Y - \frac{U}{4k^2R} . \quad (3)$$

The coefficients of the three angle-dependent terms are

$$X = \sum_J \frac{2J+1}{(2I_1+1)(2I_2+1)} \left\{ \cos 2\phi_0 \left[1 - 2 \frac{\Gamma_{od}^J}{\Gamma^J} \sin^2 \delta^J \right] + 2 \frac{\Gamma_{od}^J}{\Gamma^J} \sin \delta^J \cos \delta^J \sin 2\phi_0 \right\}, \quad (4)$$

$$Y = - \sum_J \frac{2J+1}{(2I_1+1)(2I_2+1)} \left\{ \sin 2\phi_0 \left[1 - 2 \frac{\Gamma_{od}^J}{\Gamma^J} \sin^2 \delta^J \right] - 2 \frac{\Gamma_{od}^J}{\Gamma^J} \sin \delta^J \cos \delta^J \cos 2\phi_0 \right\}, \quad (5)$$

and

$$U = \sum_s \frac{2J+1}{(2I_1+1)(2I_2+1)} (1 - |U_{os, os}^J|^2) = \frac{k^2}{\pi} \sigma_r \quad (\text{Reaction for } s\text{-waves}). \quad (6)$$

These are related to the coefficients of equation IV-1.11 by the relations,

$$\begin{aligned} X &= D_0 + 1, \\ Y &= -C_0, \end{aligned} \quad (7)$$

and

$$U = -B_0 - 2D_0.$$

The values that X , Y , and U can assume are limited by the restrictions,

$$-1 \leq X \leq 1, \quad -1 \leq Y \leq 1, \quad X^2 + Y^2 \leq 1 - U. \quad (8)$$

If the s -wave reaction cross section is known, then at each angle the s -wave scattering differential cross section involves the two unknowns X and Y , and may be plotted in the (X, Y) plane as a straight line. The common intersection of the lines corresponding to the various

angles of the angular distribution furnishes the required solution for X and Y. An example of such a graphical analysis is shown in figure 24. If the uncertainty in the common intersection exceeds that deemed permissible by the experimental error, or if the conditions of equations IV-2.8 are not obeyed, then the data require that additional angular momentum waves be included in the analysis.

It may be seen from the s-wave form of equation IV-1.14 that the quantity

$$-T_{os,os}^J = e^{-2i\phi_o} \frac{\Gamma_{osd}^J}{\Gamma^J} (e^{2i\delta^J} - 1) + e^{-2i\phi_o} - 1, \quad (9)$$

may be plotted as a vector in the complex plane. As the energy is increased the vector then describes a clockwise motion if no resonance is present, while a counter-clockwise circular motion results when passing over the region of a resonance. The graph of the intersections (X, Y) as a function of the energy should then describe these motions, and the radius of the counter-clockwise motion will be related to the parameters of the level, while the center of the circular motion will be related to the reaction width and non-resonant contributions to the scattering (Christy 1956).

It is to be noted, however, that the general s-wave scattering of particles by nuclei is described by more than three parameters. Proton scattering requires four parameters in general, a resonant phase shift and the ratio Γ_p/Γ for each channel, while deuteron scattering requires six. Therefore, even a successful analysis of an s-wave angular distribution in the above manner may not specify uniquely all of the parameters of the compound levels involved.

3. Narrow Level Analysis

Another case where the scattering analysis is simplified is when a level is narrow enough so that the only quantity in the cross section equation varying appreciably with energy in the region about the resonance is the phase shift of that level. The equation for the differential cross section can be written in general as (Christy 1956),

$$\sigma(\theta, E) = \sigma_0(\theta, E) + A(\theta, E)\sin^2\delta + B(\theta, E)\sin\delta \cos\delta. \quad (1)$$

If δ is the phase shift passing through resonance and is the only strongly energy-dependent term in the region of the narrow resonance, the energy variation of the quantities $\sigma_0(\theta, E)$, $A(\theta, E)$ and $B(\theta, E)$ can be neglected. The background due to Coulomb scattering, and scattering in channels other than the one described by the phase shift, δ , is contained in $\sigma_0(\theta, E)$.

The analysis of such a narrow level can often be performed by measuring the excitation functions at relatively few angles. The phase shift used to fit the data is determined by the width and resonant energy of the level. The angle-dependence of the fitting parameters σ_0 , A , and B , which are slowly varying with energy can be compared with theoretical expressions to obtain further information concerning the level and background contributing to the scattering.

When the background is composed of Coulomb and s-wave scattering only, σ_0/R is given by equation IV-2.3. Expressions for the coefficients A and B have been given by Christy (1956) for the case of a single level formed by orbital angular momentum l only, and with a negligible poten-

tial phase shift,

$$\begin{aligned}
 A(\theta) &= A_{Rl} + A_{sl} + A_{ll}, \\
 B(\theta) &= B_{Rl} + B_{sl}, \\
 A_{Rl} &= \frac{2(2J+1)}{(2I_1+1)(2I_2+1)} \frac{\sqrt{R}}{k} \frac{\Gamma_d}{\Gamma} \sin(2\omega_l - \xi) P_l(\cos \theta), \\
 B_{Rl} &= \frac{-2(2J+1)}{(2I_1+1)(2I_2+1)} \frac{\sqrt{R}}{k} \frac{\Gamma_d}{\Gamma} \cos(2\omega_l - \xi) P_l(\cos \theta), \\
 A_{sl} &= -\frac{2J+1}{(2I_1+1)(2I_2+1)} \frac{1}{k^2} \frac{\Gamma_d}{\Gamma} \left[\left(\sum_s a_{s's}^2 f_s - 1 \right) \cos 2\omega_l \right. \\
 &\quad \left. + \sum_s a_s^2 g_s \sin 2\omega_l \right] P_l(\cos \theta), \\
 B_{sl} &= -\frac{2J+1}{(2I_1+1)(2I_2+1)} \frac{1}{k^2} \frac{\Gamma_d}{\Gamma} \left[\left(\sum_s a_{s's}^2 f_s - 1 \right) \sin 2\omega_l \right. \\
 &\quad \left. - \sum_s a_s^2 g_s \cos 2\omega_l \right] P_l(\cos \theta), \\
 A_{ll} &= \frac{4\pi(2l+1)}{(2I_1+1)(2I_2+1)} \left(\frac{\Gamma_d}{k\Gamma} \right)^2 \sum_{\substack{ss' \\ Mm_l'}} a_s^2 a_{s'}^2 \\
 &\quad \times \left[(slm_s 0 | JM)(s'l m_s, m_l | JM) \right]^2 |Y_l^{m_l'}(\theta, \phi)|^2.
 \end{aligned} \tag{2}$$

The subscripts (Rl), (sl), and (ll) refer to the l-wave interference with the Coulomb scattering, the l-wave interference with s-wave scattering, and pure l-wave resonant scattering, respectively. The

parameters describing the s-wave scattering, f_s and g_s , are related to the quantities defined in equations IV-2.4 and 2.5 by the relations,

$$X = \sum_s \frac{2J+1}{(2I_1+1)(2I_2+1)} f_s ,$$

(3)

and

$$Y = \sum_s \frac{2J+1}{(2I_1+1)(2I_2+1)} g_s .$$

In cases where the background is energy-dependent and its nature unknown, there may be an uncertainty in the proper background to be subtracted from the total experimental cross section to allow a determination of the coefficients A and B in the above manner. While the coefficients A and B can no longer be accurately determined from the experimental data in this case, it is still usually possible to determine the difference between the maximum and minimum values of the cross section minus the background with fair precision. This difference is

$$(\sigma_{\max} - \sigma_0) - (\sigma_{\min} - \sigma_0^{\dagger}) = (A^2 + B^2)^{1/2},$$

(4)

where σ_0 and σ_0^{\dagger} are the values of the background at the maximum and minimum values of the cross section. The interpretation of A and B in terms of theoretical expressions will then usually require some knowledge of the processes contributing to the background.

4. Application of the Theoretical Expressions to Li⁷(d, d) Scattering

(a) General Discussion

The fact that the deuteron is a spin one particle complicates the analysis by increasing considerably the number of parameters to be determined over the case of neutron, proton, or alpha-particle scattering. There are three possible channel spins which can be formed when deuterons are incident on a target with non-zero spin. Thus, for the case of deuterons, $I_1^\pi = 1^+$, incident on lithium-7 nuclei, $I_2^\pi = \frac{3}{2}^-$, we can form the channel spins,

$$s^\pi = \frac{1}{2}^-, \frac{3}{2}^-, \frac{5}{2}^- . \quad (1)$$

It is then possible to form states in Be⁹ with the above values of the spin and parity by means of s-wave deuterons, while states with angular momentum from $\frac{1}{2}^+$ to $\frac{7}{2}^+$ can be formed by p-wave deuterons. In the case of s-wave deuteron scattering each state which can be formed will be described by means of a phase shift and reaction amplitude resulting in six parameters in all, while the s-wave angular distribution contains only three angle-dependent terms. The number of parameters necessary to describe higher l -wave interactions is in general larger.

The relation given in equation IV-2.1 for the partial width of a state can be used to determine for which l -values individual levels effectively participate in the scattering, if the reduced width is assumed to have a maximum value given by the Wigner Limit (Teichmann and Wigner 1952),

$$\gamma^2 = \frac{3\hbar^2}{2\mu a^2} , \quad (2)$$

where μ is the reduced mass, and the interaction radius, a , is usually assumed to be of the form,

$$a = r_0 (A_1^{1/3} + A_2^{1/3}), \quad (3)$$

where

$$r_0 \simeq 1.4 \times 10^{-13} \text{ cm.}$$

In the present experiment the maximum allowed width at one Mev due to d-waves is about 100 kev as determined by the above relations, and the maximum width due to f-waves is approximately 5 kev. However, the effect of the stripping reactions on the reaction cross section may be large, and direct reactions are included in the dispersion theory of nuclear reactions by summing over distant levels. Therefore, the cumulative effect of high ℓ -values may need to be considered in the analysis of scattering which is competing with direct reactions.

Not only the magnitude of the reaction cross section measurements, but also the structure of the scattering cross sections suggests the presence of a number of broad levels in the energy region under investigation. There is evidence from the reaction data that s-wave deuterons are responsible for the processes below one Mev (see Section I). The symmetry of the scattering cross section about one Mev, at 90° in the center-of-mass system, as seen in figure 16 and 17, suggests that interference terms due to p-wave or other odd angular momenta are vanishing at this angle. The increase in the interference terms as the scattering angle is increased can be observed in figures 19 through 22. At a center-of-mass angle of $140^\circ 46'$ where interference terms due to

$l = 3$ waves would be expected to vanish, no appreciable reduction in the interference term is visible. This fact, plus the limits imposed on the possible l -values by equations IV-4.2 and 4.3, led to the assumption of a p-wave level near one Mev in the analysis to be discussed. This analysis can be expected to be difficult in view of the broad overlapping structure observed, and the lack of knowledge concerning the many parameters involved.

(b) Analysis Procedure

As a first step in the data analysis, an attempt was made to fit the angular distributions with the theoretical expressions for purely s-wave processes contained in equations IV-2.3 through IV-2.7. The determination of the quantity U depending on the total s-wave reaction cross section is uncertain, however. The measured values for the (d,p) reaction cross section differ appreciably among the various experimenters, and have large uncertainties attributed to each measurement. In addition the (d,n) cross section, involving detection of all neutrons emitted, has been measured only at 90° and about 0° (see Section I). The integrated (d,n) cross section was therefore approximated by multiplying the experimental cross section measured at 90° by 4π . The total reaction cross section then obtained by summing the integrated cross sections for the various observed reactions was found to exceed the maximum allowable value for s-waves, π/k^2 , at a number of energies. A further difficulty in obtaining a reasonable value for U was the need to extract from the total reaction cross section that portion due to s-waves only.

The procedure adopted to estimate the s-wave contribution to the total reaction cross section was to remove the penetration factors from the cross section measurements of Baggett and Bame (1952), symmetrize the resultant peak near 0.750 Mev to which was added a constant background to account for the distant s-wave levels, and then re-introduce the penetration factors to obtain the desired cross section. The total s-wave reaction cross section computed in this manner is shown in figure 23.

Plotted in the (X, Y) plane the lines corresponding to the various angles of the angular distributions then met in a common intersection within the deviations to be expected from the experimental error, for energies between 0.400 and 1.000 Mev. Above one Mev the s-wave fit abruptly fails. While this is to be expected if the level just above one Mev is a p-wave state, the s-wave fit remains inadequate up to the highest energy at which an angular distribution was taken, 1.500 Mev.

The reaction cross section of figure 23 is large enough, however, so that the condition on U expressed in equations IV-2.8 is not satisfied for the graphical intersections obtained at a number of energies. It was therefore necessary arbitrarily to reduce the assumed value for σ_r . The values of X and Y determined by graphical analysis generally lay inside the circle $(1 - U)^{1/2}$ if the summed reaction cross section was multiplied by a factor ≤ 0.75 . Examples of the analysis of the angular distributions by the graphical technique are shown in figures 24, 25, and 26 with the reaction cross section of figure 23 reduced to five-eighths. The uncertainty in the position of the lines as determined by the experi-

mental relative error is shown on the diagrams. The presence of the resonance located just above 1.0 Mev appears to have begun to affect the diagram at 1.000 Mev in figure 26. The points of intersection were estimated from the (X, Y) plots from 0.400 to 1.000 Mev and were used to compute the s -wave cross section by means of equation IV-2.3. The calculated angular distributions in the region of 0.800 Mev are shown with the experimental points in figure 18. The error bars, located at intervals along the ordinate, represent the estimated absolute error of 6%. Over most of the angular range the experimental data lie well within the estimated error. The energy variation of the s -wave parameters determined in the above case is displayed in figure 27. While a general counterclockwise motion of the points is observed over the region of the state reported near 0.8 Mev in the reaction data, the variation of the intersections (X, Y) is at least partially determined by the magnitude of the total reaction cross section itself as required by the condition expressed in IV-2.8. The s -wave fit of the angular distributions in this energy region then appears to be consistent with a level at 0.8 Mev, but does not require such a level.

The inclusion of p - or d -waves improves the fit of the angular distributions above 1 Mev, but the accuracy with which the coefficients of the angle-dependent terms can be determined is not high enough to furnish any reliable information as to which angular momenta are involved.

Once a set of intersections (X, Y) was obtained, the possible determination of level parameters which would reproduce the values of

X and Y was investigated. The values of X and Y, obtained from the s-wave analysis by using $5/8$ and $3/4$ of the total reaction cross section in figure 23, were used in the computations. The magnitude of the reaction cross section makes it unlikely that only one channel is contributing to the s-wave processes, and it was indeed not possible to fit the values of X and Y by using reasonable values for the phase shift and ratio of the deuteron width to full width for only one channel in equations IV-2.4 and 2.5. Each channel involves two parameters, the phase shift and the ratio of the deuteron width to the full width for the state formed by that channel, and, therefore, the number of unknown parameters is at least four if more than one channel is assumed to be participating in the scattering. With the inclusion of more than one channel, therefore, it is possible to duplicate X and Y. However, a unique set of channel parameters could not be extracted.

As the total reaction cross section is so poorly known, the values of X and Y obtained are likewise somewhat uncertain. Further, as the deuteron s-wave scattering may depend on six nuclear parameters, the analysis of the angular distributions does not furnish sufficient information to allow a unique description of the scattering in terms of level parameters. More accurate reaction data is necessary to clarify the situation in this energy region.

The prominent anomaly located near one Mev appears to be superimposed upon a background principally due to non-Coulomb scattering. As a description of the region below one Mev in terms of level parameters was not possible, the complete analysis of the interval near the one-Mev

state was not feasible. However, the fact that the width of this level has been estimated at 50 kev from the reaction data, (Ajzenberg-Selove and Lauritsen 1959), suggests the possibility of subtracting the background and performing a narrow level analysis in the manner described in Section IV-3, thus partially overcoming the difficulties caused by the lack of knowledge concerning the background. The plots of the ratio of the differential cross section to the Rutherford cross section shown in figure 17 were used to perform the background subtractions. Straight lines were drawn as the estimated background subtraction from about 0.840 or 0.880 Mev, depending on the angle, on one side of the anomaly to about 1.100 or 1.200 Mev on the other side. The difference was then analyzed by means of the equations, contained in Section IV-3 assuming the level was formed by p-wave deuterons.

The present situation is sufficiently confused as to the proper background to be subtracted, that the values of A and B in equation IV-3.1 cannot be determined with accuracy. Therefore, although for the subtraction used, the data at the three angles in figure 17 could be fitted by the same phase shift, it was felt that only the quantity appearing in equation IV-3.4 could be determined with acceptable precision. The uncertainties in A and B due to the experimental error and background subtraction were then sufficient to allow the parameters in equations IV-3.2 to vary adequately to reproduce, for all the various J-values possible with p-wave deuterons, the value of $(A^2 + B^2)^{1/2}$ obtained from the difference of the maximum and minimum values of the experimental cross section after making the background subtraction. A further error

in handling the background subtraction in this fashion might be due to the assumption that only s-waves are contributing to the background, as the angular distributions could not be fitted with s-waves at any energy above one Mev. The determination of the parameters of the one-Mev level would, therefore, seem to require further knowledge of the background processes than was available.

Further attempts to fit the data were made using calculations performed by an electronic computer, programmed for equation IV-1.11 by Dr. Jack C. Overley, in this laboratory. The parameters of up to four levels being formed by channels with orbital angular momentum less than or equal to two can be inserted into the program, whereupon the computer evaluates the differential cross section. Calculations were performed on the assumption that either an s-wave state at 0.800 Mev, or a p-wave state at 1.020 Mev, or both contributed to the scattering. All possible values for the spin of the s-wave level were tried, while the parameter Γ_d/Γ was varied from 0.1 to 0.5 assuming Γ equaled 0.200 Mev. As computing the cross section for all possible combinations of the parameters for the assumed s- and p-wave levels was unmanageable, the width of the p-wave state was taken as 50 kev with Γ_d/Γ equal to 1/3, and the spin was assumed to be $\frac{7}{2}^+$ since this spin value can be formed in only one channel and so involves the least number of parameters. While the possible choices and combinations of parameters for the two levels were, therefore, by no means exhausted, the values tried were not capable of fitting the data.

The assumption of an s-wave level at 0.8 Mev and a p-wave level

at 1 Mev does not seem to permit a fit of the scattering data. The magnitude of the reaction cross section and its possible non-resonant form due to stripping suggest that more than the above limited number of levels are contributing to the collision matrix in this energy region. The scattering angular distributions, and the ratio of the experimental to the Rutherford cross section above one Mev also support this view. The addition of broad higher-energy levels, or non-resonant contributions therefore seems to be necessary to adequately describe the observed scattering.

(c) Conclusions

Although it was not clear at the commencement of this work that deuteron elastic scattering would show resonant-type anomalies, the data of the present experiment show clearly that large variations of the scattering cross section, from that expected from purely Rutherford scattering, do occur. These strong deviations from Coulomb scattering preclude the possibility of searching for small effects to be associated with the loose structure of the deuteron.

The scattering analysis performed appears to support the impression obtained from the reaction data (see Section I) that any level below one Mev is an s-wave state. The form of the scattering cross section at 90° and $140^\circ 46'$ indicates that the level near one Mev is formed by odd orbital angular momentum, and most likely by p-waves. The value of the penetration factor which limits an f-wave width to around 5 kev, also supports the view that this is a p-wave level. This assignment is in agreement with the narrow level analysis performed. No evidence of

a level near 1.4 Mev is observed although the data do not exclude such a level.

Due to the many parameters involved, a more complete description of the nuclear parameters in the energy region investigated will require much more accurate measurements of the competing reactions than have been carried out up to the present. In particular the measurements of the (d, α) excitation function, and the angular distribution of the first alpha particle as a function of energy would be desirable. As it is difficult to investigate this energy region in Be^9 by means of reactions initiated by alpha-particles, protons, or neutrons, the analysis of experiments involving these levels will be complicated. Although, the interpretation of (He^3 , p) reactions is at present somewhat uncertain, a more complete understanding of the reaction mechanism involved may make this process a significant tool for the spectroscopic analysis of the residual nucleus formed. If this should become the case, the $\text{Li}^7(\text{He}^3, \text{p})$ reaction would be useful as an alternate method of determining the parameters of the levels in this region of Be^9 .

APPENDIX I

Thick Target Yield for a Non-Uniform Target

The previous derivation for a thick target yield assumed a uniform target composition, and must be modified if the composition is a function of the depth in the target at which the scattering occurs. Equation III-1.10 was obtained by also assuming that the quantities which determine the yield do not vary appreciably over the angle and energy acceptance windows of the magnetic spectrometer. However, the kinematics resulting from a large center-of-mass motion may be such that the yield contains contributions from a considerable range at depths in the target. In this case, as the spectrometer window has finite resolution in angle and energy the angle and energy variations over the spectrometer window of the quantities appearing in the yield equation may be appreciable, and need to be included in the yield calculation. These modifications to the yield calculation of Section III-1 need to be included in order to determine the effect of an oxygen contamination on the yield of deuterons scattered from lithium.

The yield obtained from a non-uniform target has been derived by Powers (1962). The rate of energy loss is now a function of both energy and depth within the target:

$$\begin{aligned} \frac{dE}{dx}(E, x) &= n_T(x)\epsilon_T(E) + n_I(x)\epsilon_I(E) \\ &= \epsilon_T(E) \left[n_T(x) + n_I(x) \frac{\epsilon_I(E)}{\epsilon_T(E)} \right] \end{aligned} \quad (A1)$$

where $n_T(x)$ and $n_I(x)$ denote the number of target and impurity atoms per unit volume respectively; and $\epsilon_T(E)$ and $\epsilon_I(E)$ denote the stopping cross sections for the target material and impurity, respectively.

The variables in this relation can be separated if $\epsilon_I(E)/\epsilon_T(E)$ is assumed to be independent of energy. In this case we have

$$\int_0^{s/\cos \theta_1} \left[n_T(x) + n_I(x) \frac{\epsilon_I(E)}{\epsilon_T(E)} \right] dx = - \int_{E_{1B}}^{E_1} \frac{dE}{\epsilon_T(E)} \quad (A2)$$

and

$$\int_0^{s/\cos \theta_2} \left[n_T(x) + n_I(x) \frac{\epsilon_I(E)}{\epsilon_T(E)} \right] dx = - \int_{E_2}^{E_{20}} \frac{dE}{\epsilon_T(E)} \quad (A3)$$

where E_1 and E_2 are again the energies at the lamina at depth s . Proceeding as with a uniform target by taking the partial derivative of s with respect to E_{20} we obtain

$$\left| \frac{n_T(s) ds}{\cos \theta_1} \right| = \frac{\epsilon_T(E_2) dE_{20}}{\epsilon_T(E_{20}) \left\{ a_T \left[\epsilon_T(E_1) + \frac{n_I(s)}{n_T(s)} \epsilon_I(E_1) \right] + \frac{\cos \theta_1}{\cos \theta_2} \left[\epsilon_T(E_2) + \frac{n_I(s)}{n_T(s)} \epsilon_I(E_2) \right] \right\}} \quad (A4)$$

The $Li^7(d, d)$ yield per incident particle can then be written as

$$Y \approx \int_{E_f - (\Delta E_{20}/2)}^{E_f + (\Delta E_{20}/2)} \int_{\theta_o - (\delta\theta/2)}^{\theta_o + (\delta\theta/2)} \frac{\frac{n_{Li^7}}{n_{Li}} \frac{\Omega}{\delta\theta \sin \theta_o} W(E_{20}) dE_{20}}{\epsilon_{Li}(E_{20}) \left[1 + \frac{n_O}{n_{Li}} \frac{\epsilon_O(E_2)}{\epsilon_{Li}(E_2)} \right]} \times \frac{w(\theta) \sigma(E_1, \theta) \sin \theta d\theta}{a_{Li}(\theta) \frac{\beta_1}{\beta_2} + \frac{\cos \theta_1}{\cos(\pi - \theta - \theta_1)}} \quad (A5)$$

where the subscripts refer to the element or isotope in question. The

quantity β_1 is given by

$$\beta_1 = \epsilon_{\text{Li}}(E_1) + \frac{n_{\text{O}}}{n_{\text{Li}}} \epsilon_{\text{O}}(E_1) \quad (\text{A6})$$

and similarly for β_2 . The nominal values of the spectrometer window are E_f and θ_0 , while ΔE_{20} and $\delta\theta$ are the widths of the windows. The transmission functions of the magnet in energy and angle are given by $W(E_{20})$ and $w(\theta)$. In the present calculations a square window was adopted for the energy, while $w(\theta)$ was taken as parabolic. The parabolic window was normalized so that

$$\frac{1}{\delta\theta} \int_{\theta_0 - (\delta\theta/2)}^{\theta_0 + (\delta\theta/2)} w(\theta) d\theta = 1, \quad (\text{A7})$$

where $\delta\theta$ is 3° , the full width of the angular window. The assumed shapes of both the energy and angular windows are probably only approximately correct, but are reasonable choices in view of the entrance and exit slits used with the magnet. The ratios of the stopping cross sections $\epsilon_{\text{O}}(E_2)/\epsilon_{\text{Li}}(E_2)$ and β_1/β_2 are not strongly energy dependent and were assumed to be constant during the calculations. The cross section was assumed to be given by the Rutherford formula for both the O^{16} and Li^7 yield determinations, which should be a good assumption at low energies.

Relations similar to III-1.7 and 1.8 can be obtained and used to give approximate solutions for E_1 and s ,

$$s \approx \frac{\cos \theta_1}{n_{\text{T}}} \frac{(E_{1\text{B}} - E_1)}{\beta_1} \quad (\text{A8})$$

and

$$E_1 \approx \frac{\eta \frac{\beta_2}{\beta_1} E_{1B} + E_{20}}{\alpha_T + \eta \frac{\beta_2}{\beta_1}}, \quad (A9)$$

where $\eta = \cos \theta_1 / \cos \theta_2$, and where averaging must be performed in the manner described in Section III-1.

The profile shown in figure 10 was used to estimate the oxygen distribution. Equation A5, rewritten so as to treat the oxygen as the target nucleus, was used to determine n_O/n_{Li} at a number of points on the low energy side of the oxygen peak. As the oxygen distribution was unknown the variation of the integrand over the spectrometer window was neglected. The distribution obtained was extrapolated to a value of 1/2, corresponding to Li_2O , at the target surface. Equations A8 and A9 can then be used to determine n_O/n_{Li} , as a function of s , the depth within the target. The calculated oxygen distribution was then used to recompute the oxygen peak. The integration over the spectrometer windows was done numerically, first over angle giving a series of energy-dependent terms, and then over energy for each term. The computed peak was 11% lower than the one obtained experimentally, which is taken as reasonable agreement considering the approximations which have been made above.

The equations A8 and A9 can be used to determine n_O/n_{Li} as a function of the energy E_{20} of deuterons scattered from lithium, and the numerical integration repeated as before to obtain the $Li^7(d, d)$ yield. As expected the range of depths in the target from which the magnet accepts particles is greater for deuterons incident on lithium,

than for the case of protons incident on oxygen used to estimate the oxygen distribution. The results of the $\text{Li}^7(d, d)$ yield calculations were discussed in Section III-5, and indicated that the yields measured below a bombarding energy of about 0.4 Mev were likely to have been substantially reduced from their correct values. These calculations illustrate that great care must be exercised in the preparation of easily contaminated targets. Even, if a contaminant-free target has been successfully prepared, deterioration under bombardment by the beam may limit the extent to which the target may be used.

APPENDIX II

Sample Calculation of the Elastic Scattering Differential Cross Section
From Experimental Thick Target Data

The differential cross section for the elastic scattering of deuterons from lithium-7 can be determined from the profiles of figures 5 and 14. The Cu(p, p) profile of figure 5 and the Li⁷(d, d) profile of figure 14 were taken on the same run.

The equation for the differential cross section in the laboratory system is

$$\sigma_L(E_1, \theta) = \frac{eZ}{2CV} \frac{N_s R}{n\Omega_{sp}} \frac{\epsilon(E_{20})}{E_{20}} \left[\frac{\cos \theta_1}{\cos \theta_2} + \frac{\epsilon(E_1)}{\epsilon(E_2)} \frac{\partial E_2}{\partial E_1} \right] Y. \quad \text{III-1.11}$$

The yield at the fluxmeter setting of $V_m = 0.670$ volts, on the plateau of the Cu(p, p) profile, is 60,235 counts, which, corrected for the electronic dead-time, gives a total of 60,589 counts. The magnetic spectrometer constant obtained from this profile is 0.3829 Mev-volts² corresponding to particles with an energy $E_{20} = 0.8526$ Mev traversing the magnetic spectrometer at the fluxmeter setting $V_m = 0.670$ volts. From Whaling (1958) the stopping cross section at this energy is found to be $\epsilon(E_{20}) = 13.8 \times 10^3$ Mev-barns. Given the bombarding energy of $E_{1B} = 0.9032$ Mev, the energy of the particle at scattering is found from equation III-1.13 to be $E_1 = 0.8964$ Mev. The other stopping cross sections entering equation III-1.11 are estimated to be

$$\epsilon(E_1) = 13.4 \times 10^3 \text{ Mev-barns,}$$

$$\epsilon(E_2) = 13.7 \times 10^3 \text{ Mev-barns.}$$

As the given profile corresponds to scattering angles in the laboratory

and center-of-mass systems of

$$\theta_L = 109^{\circ}34'$$

and

$$\theta_{cm} = 110^{\circ}26'$$

we have from equation II-4.3

$$\frac{\partial E_2}{\partial E_1} = a = 0.9582.$$

Therefore, the expression involving the stopping cross sections is

$$\epsilon(E_{20}) \left[\frac{\cos \theta_1}{\cos \theta_2} + \frac{\epsilon(E_1)}{\epsilon(E_2)} \frac{\partial E_2}{\partial E_1} \right] = 26.73 \times 10^3 \text{ Mev-barns.}$$

The transformation from the laboratory system to the center-of-mass system, given by equation III-1.18, is

$$\frac{\Omega_L}{\Omega_{cm}} = 1.0109.$$

The Rutherford cross section, given by equation III-1.22, is

$$\frac{d\sigma_R}{d\Omega} = \frac{1.1249}{(0.8964)^2 (0.8213)^4} = 3.0768 \text{ barns/steradian.}$$

Therefore, as $N_s/n = 1$, we have

$$\frac{eZ}{2CV} \frac{R}{\Omega_{sp}} = \frac{(3.0768)(0.8526)}{(26.73 \times 10^3)(1.0109)(60,589)} = 1.602 \times 10^{-9} / \text{steradian.}$$

Referring now to the $\text{Li}^7(d,d)$ profile of figure 14 and selecting the

"following" point at $V_m = 0.7006$, the total yield is 1045 counts, and sub-

tracting the background of 25 counts gives a corrected yield of 1020 counts. The stopping cross section, $\epsilon(E_{20})$, evaluated at the energy of the detected deuterons, $E_{20} = 0.3901$ Mev, is 7.08×10^3 Mev-barns. The reaction energy is then $E_1 = 0.8936$ Mev, and

$$\epsilon(E_1) = 4.50 \times 10^3 \text{ Mev-barns}$$

$$\epsilon(E_2) = 7.00 \times 10^3 \text{ Mev-barns.}$$

The $\text{Li}^7(d, d)$ profile of figure 14, measured at the same laboratory scattering angle as the previous copper profile corresponds, however, to a different center-of-mass angle, and the values for the scattering angles in the two systems are now

$$\theta_L = 109^\circ 34'$$

and

$$\theta_{\text{cm}} = 125^\circ 16'$$

giving

$$a = 0.4533$$

and

$$\frac{\Omega_L}{\Omega_{\text{cm}}} = 1.2817.$$

Therefore, we have

$$\epsilon(E_{20}) \left[\frac{\cos \theta_1}{\cos \theta_2} + \frac{\epsilon(E_1)}{\epsilon(E_2)} \frac{\partial E_2}{\partial E_1} \right] = 9.143 \times 10^3 \text{ Mev-barns.}$$

The differential cross section in the center-of-mass system is then

$$\frac{d\sigma}{d\Omega} = \frac{(1.602 \times 10^{-9})(9.143 \times 10^3)(1020)(1.2817)(1.0813)}{(0.951)(0.3901)}$$

$$= 0.0558 \text{ barns/steradian,}$$

as $N_s/n = 1.0813$ for a natural lithium target, and the charge exchange correction is taken from figure 9 as 0.951.

The Rutherford cross section is now

$$\frac{d\sigma_R}{d\Omega} = \frac{0.01932}{(0.8936)^2(0.8881)^4} = 0.0389 \text{ barns/steradian.}$$

The ratio of the scattering cross section to the Rutherford cross section is then

$$\frac{d\sigma/d\Omega}{d\sigma_R/d\Omega} = 1.434.$$

A computer program was written for the calculation of the scattering cross section from the experimental data. The input data to the Burroughs 220 digital computer consisted primarily of the fundamental constants appearing in the cross section equation, the calibration constants of the electrostatic analyzer, and magnetic spectrometer, and the raw data obtained during the experiment such as the yield, electrostatic analyzer and magnetic spectrometer settings. The computer was programmed to calculate the necessary values of the stopping cross sections and charge exchange correction from a polynomial fit of the published measurements of these quantities in energy regions where semi-empirical formulae were not already available.

REFERENCES

- S. K. Allison, 1958, *Revs. Modern Phys.* 30, 1137.
- F. Ajzenberg-Selove and T. Lauritsen, 1959, *Nuclear Physics* 11, 1.
- M. Bader, R. E. Pixley, F. S. Mozer, and W. Whaling, 1956, *Phys. Rev.* 103, 32.
- L. M. Baggett and S. J. Bame, Jr., 1952, *Phys. Rev.* 85, 434.
- W. C. Barber, F. Berthold, G. Fricke, and F. E. Gudden, 1960, *Phys. Rev.* 120, 2081.
- R. K. Bardin, 1961, Ph. D. Thesis, California Institute of Technology.
- J. Benveniste, R. G. Finke, and E. A. Martinelli, 1956, *Phys. Rev.* 101, 655.
- S. Bashkin, 1954, *Phys. Rev.* 95, 1012.
- J. M. Blatt, and L. C. Biedenharn, 1952, *Revs. Modern Phys.* 24, 258.
- A. B. Brown, C. W. Snyder, W. A. Fowler, and C. C. Lauritsen, 1951, *Phys. Rev.* 82, 159.
- J. Catala, R. Font, F. Senent, J. A. y M de la Cuadra, 1958, *Nuovo Cimento* 9 Supplement No. 2, 377.
- R. F. Christy, 1956, *Physica* 22, 1009.
- F. J. M. Farley, and R. E. White, 1957, *Nuclear Physics* 3, 561.
- W. A. Fowler, 1960, Private Communication.
- W. A. Fowler, C. C. Lauritsen, and T. Lauritsen, 1947, *Rev. Sci. Instr.* 18, 818.
- J. B. French and M. L. Goldberger, 1952, *Phys. Rev.* 87, 899.
- E. Guth, 1960, Private Communication.
- T. Hall, 1950, *Phys. Rev.* 79, 504.
- E. Kashy, R. R. Perry, and J. R. Risser, 1960, *Phys. Rev.* 117, 1289.
- R. W. Kavanagh, 1960, *Nuclear Physics* 15, 411.

- A. M. Lane and R. G. Thomas, 1958, *Revs. Modern Phys.* 30, 257.
- R. L. Macklin and H. E. Banta, 1955, *Phys. Rev.* 97, 753.
- P. Malmberg, 1956, *Phys. Rev.* 101, 114.
- J. B. Marion, 1961, *Revs. Modern Phys.* 33, 139.
- E. A. Milne, 1953, Ph.D. Thesis, California Institute of Technology.
- F. B. Morinigo, 1961a, Private Communication.
- F. B. Morinigo, 1961b, To be published.
- F. S. Mozer, 1956, Ph.D. Thesis, California Institute of Technology.
- J. C. Overley, 1961a, Ph.D. Thesis, California Institute of Technology.
- J. C. Overley, 1961b, Private Communication.
- J. A. Phillips, 1955, *Phys. Rev.* 97, 404.
- R. L. Powers, 1962, Ph.D. Thesis, California Institute of Technology.
- A. C. Riviere, 1956/57, *Nuclear Physics* 2, 81.
- A. C. Riviere and P. B. Treacy, 1957, *Australian J. Phys.* 10, 209.
- J. P. F. Sellschop, 1960, *Phys. Rev.* 119, 251.
- J. C. Slattery, R. A. Chapman, and T. W. Bonner, 1957, *Phys. Rev.* 108, 809.
- C. W. Snyder, S. Rubin, W. A. Fowler, and C. C. Lauritsen, 1950, *Rev. Sci. Instr.* 21, 852.
- T. Teichmann and E. P. Wigner, 1952, *Phys. Rev.* 87, 123.
- C. C. Trail, 1956, Ph.D. Thesis, A. and M. College of Texas.
- W. D. Warters, 1953, Ph.D. Thesis, California Institute of Technology.
- W. A. Wenzel, 1952, Ph.D. Thesis, California Institute of Technology.
- W. Whaling, 1958, The Energy Loss of Charged Particles in Matter; in Handbuch der Physik, S. Flugge, ed., Bd. XXXIV, pp. 193 ff., Springer Verlag, Berlin.

TABLE I
Sources of Error in the Scattering Cross Section

| | <u>% Error</u> |
|--|----------------|
| 1. RELATIVE ERROR | |
| A. Errors in Cu Yield | |
| 1. Counting Statistics | 0.4 |
| 2. Firing Voltage Fluctuations | 0.5 |
| B. Errors in Li Yield | |
| 1. Counting Statistics | |
| Forward Angles | 1.0-2.0 |
| Back Angles | 1.0-3.0 |
| 2. Firing Voltage Fluctuations | 0.5 |
| 3. Target Composition | 1.0 |
| C. Errors in Energy Dependent Terms | |
| 1. Determination of E_{20} for Cu | 0.3 |
| 2. Determination of E_{20} for Li | 0.3 |
| 3. Uncertainty in Cu Rutherford Cross Section due to 0.2% error in E_1 | 0.4 |
| D. Errors in Angle and Stopping Cross Section Dependent Terms | |
| 1. Uncertainty in $(\cos \theta_1 / \cos \theta_2) + a[\epsilon(E_1) / \epsilon(E_2)]$ for Cu due to a 2.0% relative error in ϵ_{Cu} | 1.0 |
| 2. Uncertainty in $(\cos \theta_1 / \cos \theta_2) + a[\epsilon(E_1) / \epsilon(E_2)]$ for Li due to a 2.0% relative error in ϵ_{Li} | 1.0 |
| 3. Uncertainty in Cu Rutherford Cross Section due to 0.5° error in angle (Angular Distributions Only) | |
| Minimum Forward Angle | 3.0 |
| Maximum Back Angle | 1.0 |
| Combined Relative Error | 2.0-3.5 |

TABLE I (Continued)

| | <u>% Error</u> |
|---|----------------|
| 2. ADDITIONAL SOURCES OF ERROR CONTRIBUTING TO THE ABSOLUTE ERROR | |
| A. Uncertainty in Cu Stopping Cross Section | 3.0 |
| B. Uncertainty in Li Stopping Cross Section | 3.0 |
| C. Uncertainty in Charge Exchange Correction ϕ_L for $E_{20} \leq 0.200$ Mev | 3.0 |
| D. Uncertainty in Dead-time | 0.5 |
| Combined Absolute Error | 5.5-6.3 |

Table II
The Li⁷ (d, d) Angular Distributions

| σ_x | θ cm | | | | | | | | | | | | | | |
|------------|-------------|--------|--------|--------|--------|---------|---------|---------|--------|---------|--------|---------|--|--|--|
| | 66°25' | 72°33' | 78°28' | 84°16' | 95°44' | 101°32' | 107°27' | 113°35' | 120°0' | 134°26' | 154°9' | 163°44' | | | |
| 0.400 | 1.236 | 0.873 | 0.660 | 0.478 | 0.329 | 0.256 | 0.233 | 0.171 | 0.153 | 0.115 | | | | | |
| 0.500 | 0.791 | 0.544 | 0.396 | 0.298 | 0.192 | 0.156 | 0.132 | 0.100 | | 0.073 | 0.049 | | | | |
| 0.600 | 0.475 | 0.316 | 0.227 | 0.170 | 0.099 | 0.082 | 0.067 | 0.059 | | 0.037 | 0.035 | | | | |
| 0.700 | 0.316 | 0.214 | 0.156 | 0.123 | 0.082 | 0.067 | 0.059 | 0.053 | | 0.042 | 0.038 | | | | |
| 0.750 | 0.284 | 0.197 | 0.147 | 0.113 | 0.077 | 0.065 | 0.058 | 0.052 | | 0.044 | 0.042 | | | | |
| 0.800 | 0.254 | 0.176 | 0.134 | 0.106 | 0.073 | 0.062 | 0.057 | 0.051 | | 0.049 | 0.048 | | | | |
| 0.850 | 0.221 | 0.151 | 0.117 | 0.098 | 0.067 | 0.061 | 0.057 | 0.052 | | 0.053 | 0.051 | | | | |
| 0.900 | 0.191 | 0.139 | 0.107 | 0.088 | 0.066 | 0.061 | 0.058 | 0.056 | | 0.052 | 0.054 | | | | |
| 0.950 | 0.177 | 0.133 | 0.105 | 0.086 | 0.068 | 0.063 | 0.059 | 0.056 | | 0.048 | 0.051 | | | | |
| 0.980 | 0.176 | 0.132 | 0.108 | 0.088 | 0.070 | 0.065 | 0.058 | 0.055 | | 0.051 | 0.052 | | | | |
| 1.000 | 0.184 | 0.141 | 0.114 | 0.091 | 0.071 | 0.064 | 0.060 | 0.054 | | 0.051 | 0.056 | | | | |
| 1.020 | 0.192 | 0.148 | 0.118 | 0.090 | 0.069 | 0.064 | 0.059 | 0.056 | | 0.062 | 0.072 | | | | |
| 1.050 | 0.183 | 0.136 | 0.104 | 0.085 | 0.064 | 0.060 | 0.060 | 0.058 | | 0.079 | 0.117 | | | | |
| 1.100 | 0.158 | 0.120 | 0.092 | 0.076 | 0.064 | 0.061 | 0.063 | 0.063 | | 0.084 | 0.106 | | | | |
| 1.200 | | | 0.086 | 0.068 | 0.062 | 0.061 | 0.062 | 0.060 | | 0.077 | 0.091 | | | | |
| 1.300 | | | | | 0.061 | 0.059 | 0.058 | 0.058 | 0.062 | 0.071 | 0.085 | 0.090 | | | |
| 1.350 | | | | | 0.059 | 0.056 | 0.055 | 0.057 | 0.058 | 0.069 | 0.081 | 0.084 | | | |
| 1.400 | | | | | 0.056 | 0.054 | 0.051 | 0.053 | 0.056 | 0.064 | 0.081 | 0.083 | | | |
| 1.450 | | | | | 0.052 | 0.050 | 0.050 | 0.051 | 0.054 | 0.063 | 0.076 | 0.081 | | | |
| 1.500 | | | | | 0.048 | 0.047 | 0.045 | 0.048 | 0.050 | 0.061 | 0.074 | 0.080 | | | |

Table II

The $\text{Li}^7(d, d)$ Angular Distributions

The $\text{Li}^7(d, d)$ differential cross sections in barns per steradian obtained during the angular distribution measurements are shown for the energies in Mev given in the first column. The center-of-mass angles at which the data were taken are listed at the heads of the columns. See text pp. 41.

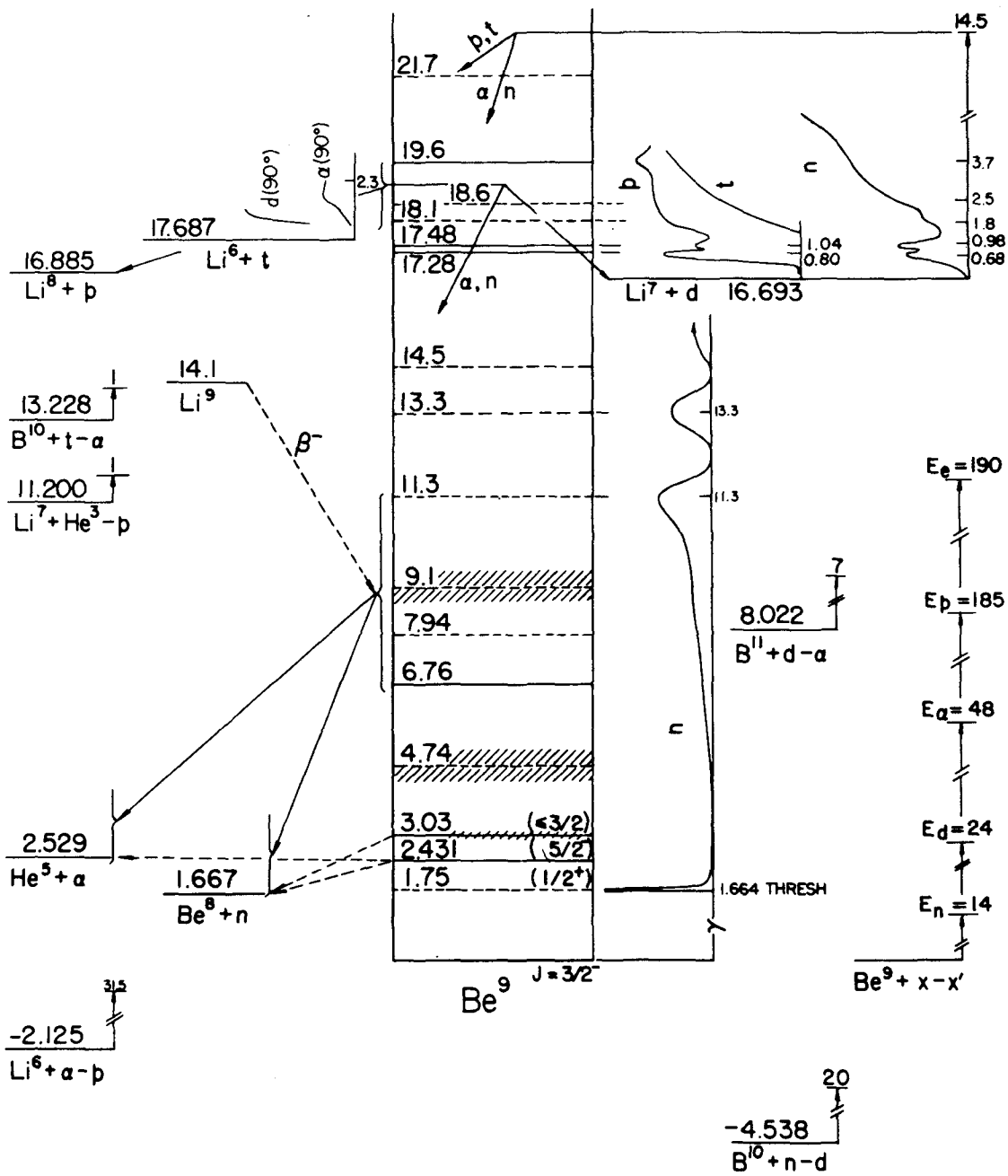


Figure 1
Energy Levels of Be^9

The energy levels of the compound nucleus Be^9 formed in the bombardment of lithium-7 by deuterons are shown in the energy level diagram on the opposite page. The excited levels above the binding energy of 16.693 Mev of the deuteron in the Be^9 nucleus are the states investigated in the present experiment. A number of measured excitation functions for the competing reactions are also shown. See text p. 5.

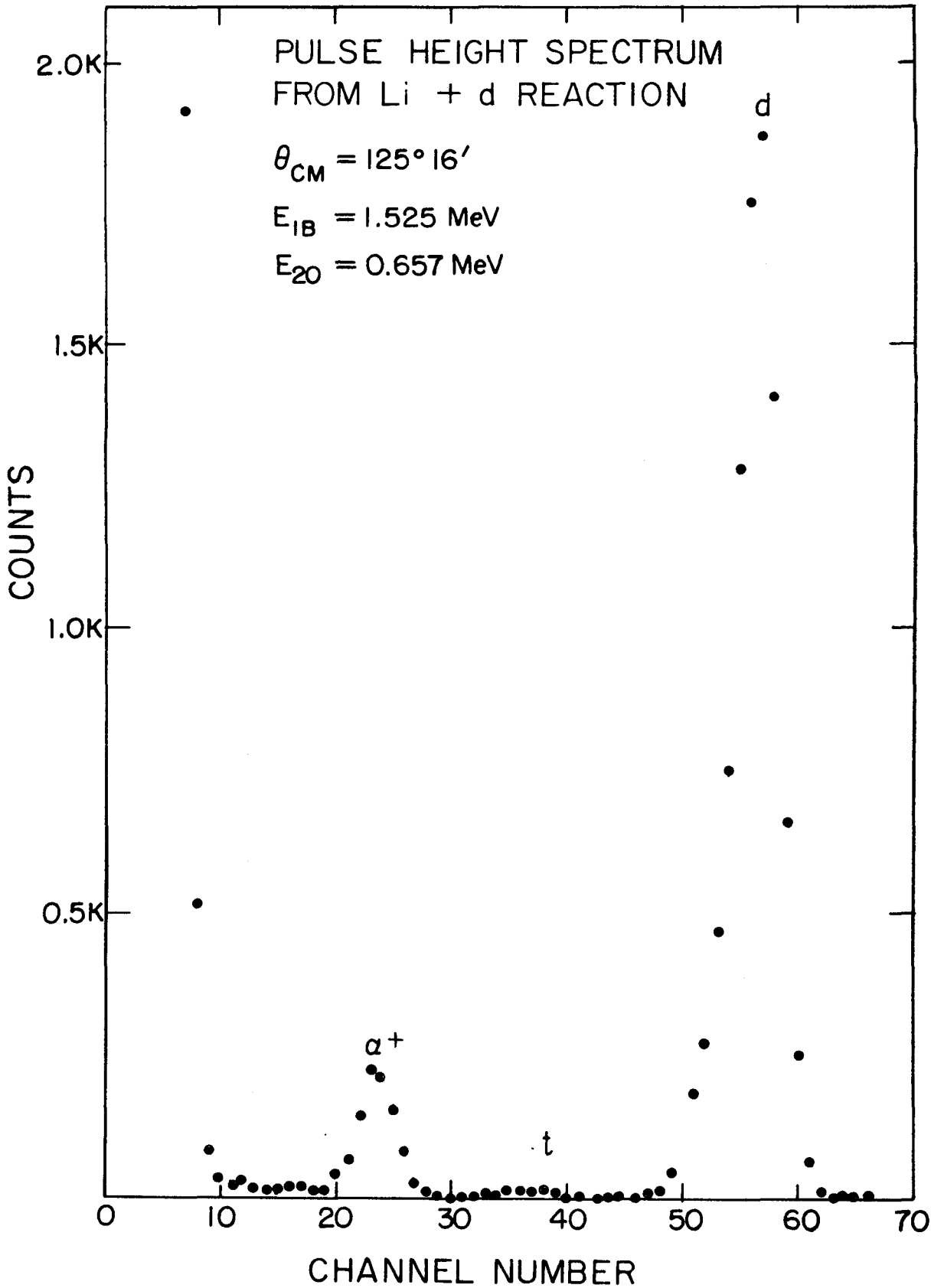


Figure 2

The Pulse Height Spectrum Resulting
from Bombardment of Lithium by Deuterons

A pulse height spectrum as recorded on a RIDL 100-channel pulse height analyzer, displaying the particle groups emitted from a thick target of natural lithium bombarded by 1.525 Mev deuterons. The singly-charged alpha-particle, triton, and deuteron peaks may be seen, while the doubly charged alpha-particle, and proton peaks occur at twice the energy of the deuteron peak and so were not recorded by the multichannel analyzer. See text p. 10.

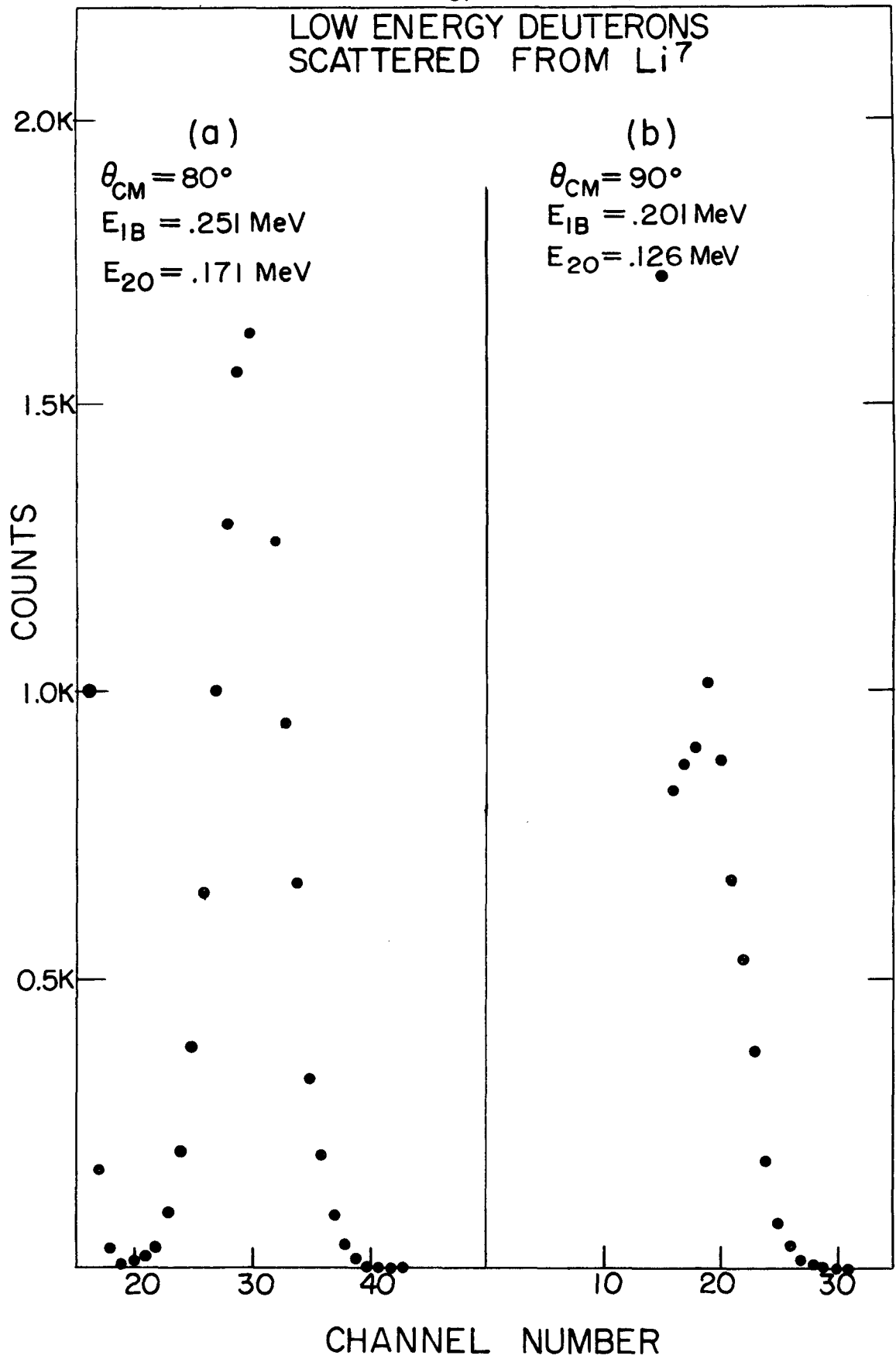


Figure 3

Low Energy Deuterons Scattered from Li^7

The large center-of-mass motion resulting from the bombardment of lithium by deuterons produces scattered deuterons of low energy. The spectra displayed in figure 3(a) and (b), corresponding to scattered deuterons with energies of 0.171 Mev and 0.126 Mev respectively, illustrate the limitation imposed by the electronic noise on the particle energy which could be detected. These spectra were recorded on a RIDL 100-channel pulse height analyzer. See text pp. 10, 11.

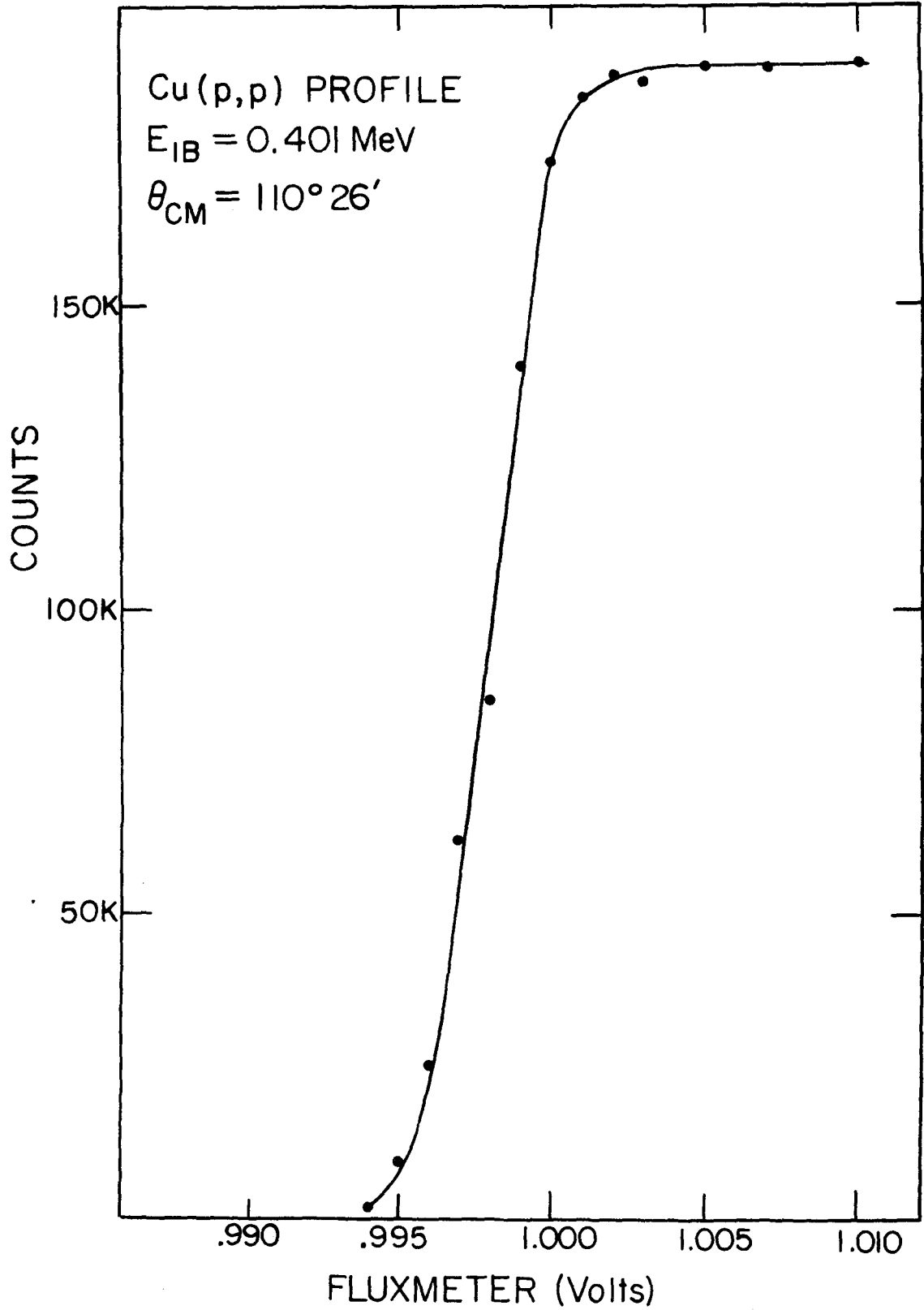


Figure 4

Cu(p,p) Profile at 0.401 Mev

The momentum distribution of protons elastically scattered from a thick copper target. The abscissa represents the fluxmeter setting of the high-resolution double-focussing magnetic spectrometer used to analyze the reaction products formed within the thick target. The energy scale, therefore, increases to the left. The mid-point of the profile rise corresponds to the energy of the particles scattered from the target surface. It was profiles such as this that were used to determine the magnetic spectrometer calibration constant, and solid angle. See text pp. 14, 17.

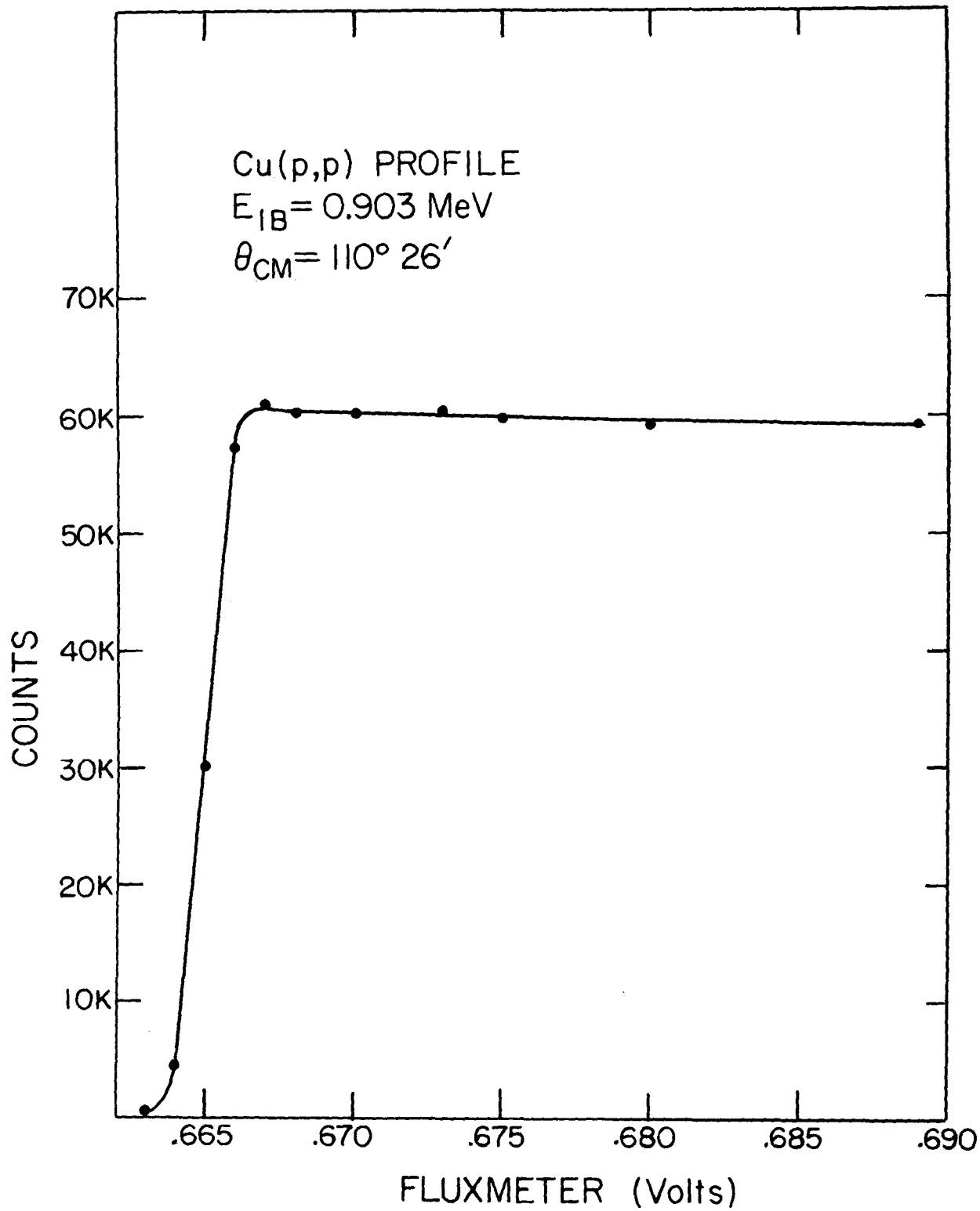
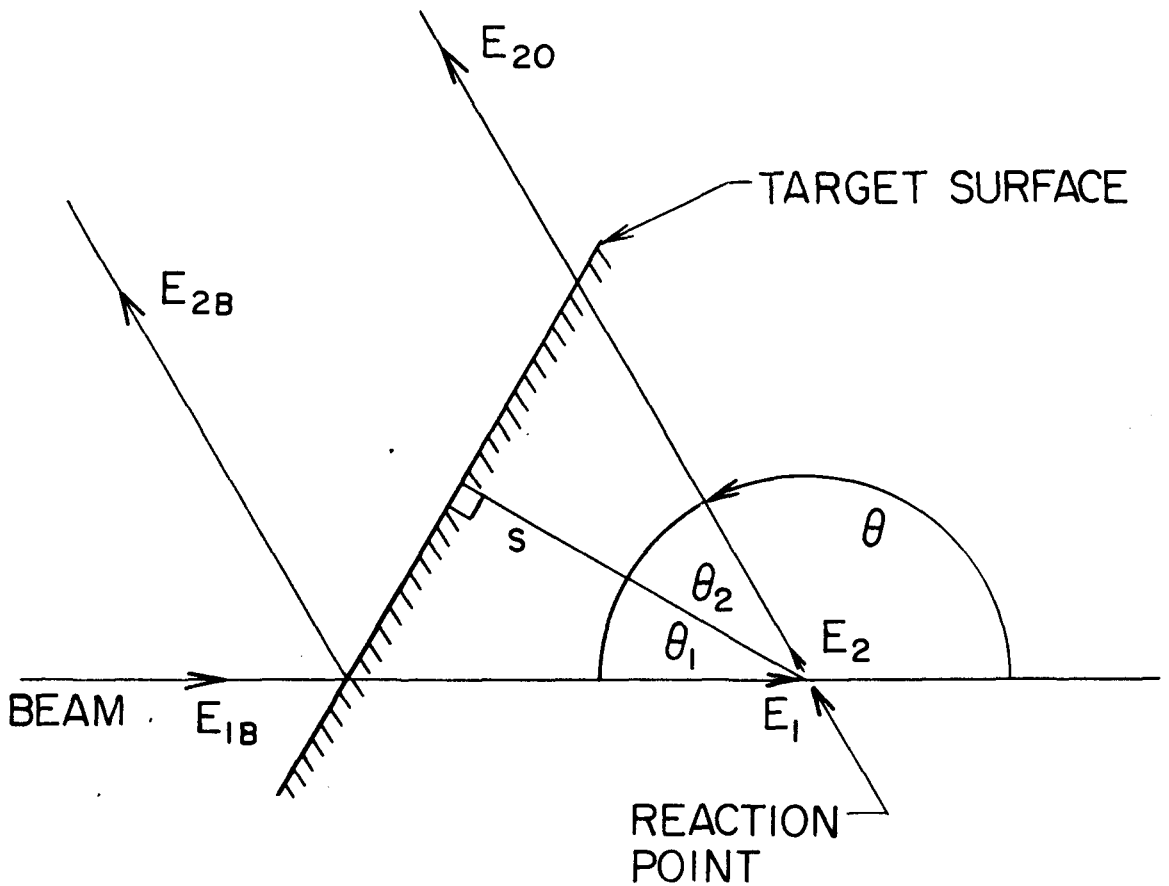


Figure 5

Cu(p,p) Profile at 0.903 Mev

Another copper profile measured at the identical angle as the one in figure 4, but at a higher incident proton energy. This profile is used as the basis for the sample calculations contained in Appendix II. See text pp. 14, 70.



SCATTERING OF PARTICLES
FROM A THICK TARGET

Figure 6
Scattering of Particles
from a Thick Target

The various energies at different depths within the thick target are illustrated in the accompanying diagram. The incident beam with energy E_{1B} may be scattered at a laboratory angle θ from the target surface resulting in particles with energy E_{2B} given by the relation

$$E_{2B} = \alpha E_{1B} .$$

The particles also penetrate the target and are subsequently degraded in energy to a value E_1 before reaction, resulting in scattered particles of energy E_2 , which are further reduced in energy by the target material to the value E_{20} as measured by the magnetic spectrometer. The magnetic spectrometer selects particles from a lamina of width ds at the depth s . The angles θ_1 and θ_2 are measured between the incoming and outgoing beams, and the normal to the target surface. See text p. 18.

THE FURNACE - COLD TRAP
APPARATUS

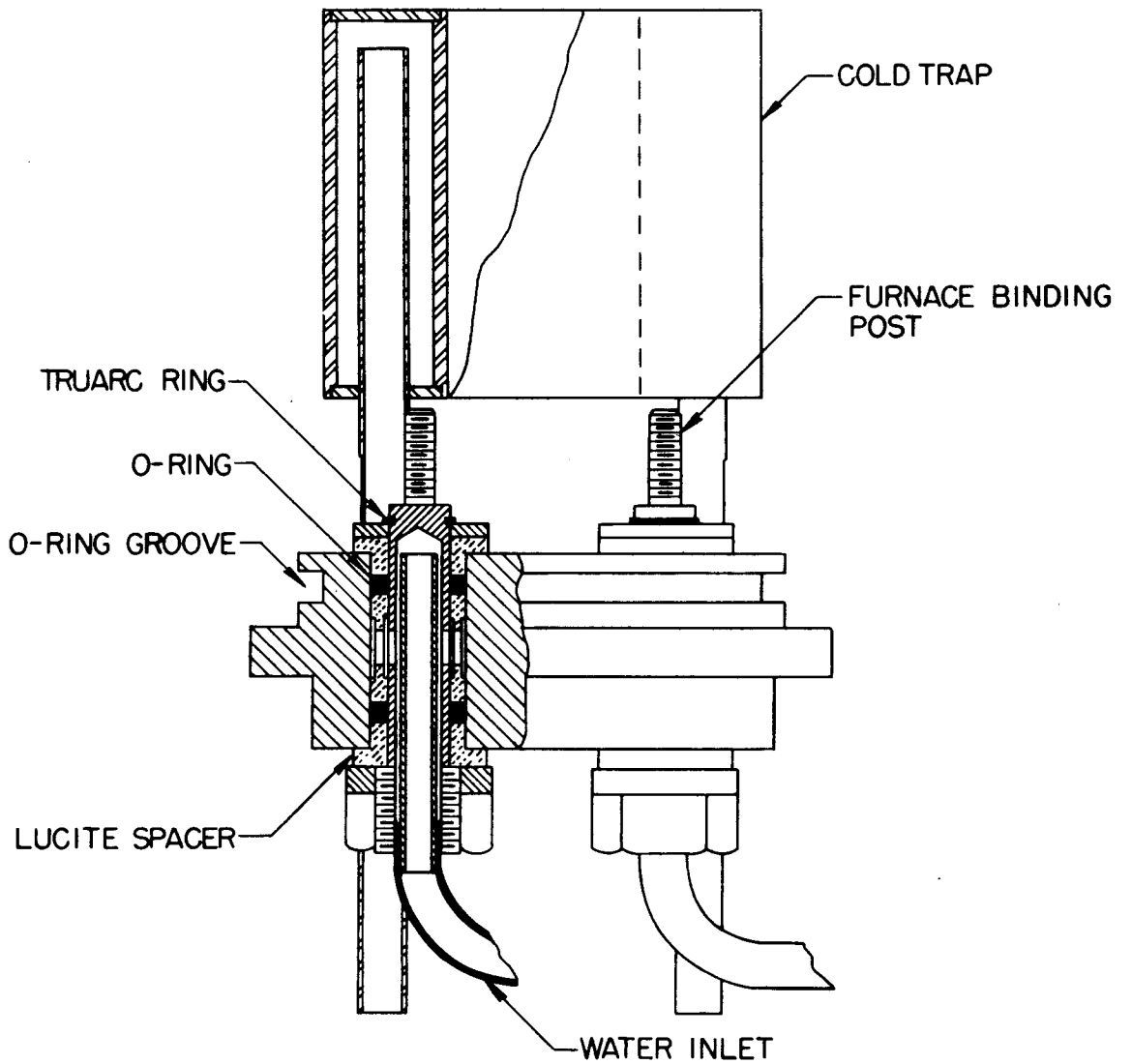


Figure 7

The Furnace - Cold Trap Apparatus

The furnace - cold trap apparatus consists of a cylindrical cold trap with a ring shaped cross section as viewed from above. A cross sectional view is shown of the left portion of the apparatus to illustrate its construction. The cold trap was constructed of stainless steel, and could be filled and emptied by means of the two tubes seen in the diagram. The binding posts for the furnace used in the lithium evaporation can be seen below the cold trap, and consist of two water cooled brass terminals insulated from the brass body of the apparatus by means of lucite spacers. The cooling water passed from one terminal to the other by means of a horizontal hole drilled through the brass body. The target holder was lowered through the cold trap into a cup in the bottom of the apparatus to position the copper target blank in front of the furnace. When bombarded by the incident beam the target was situated just above the cold trap. See text p. 29.

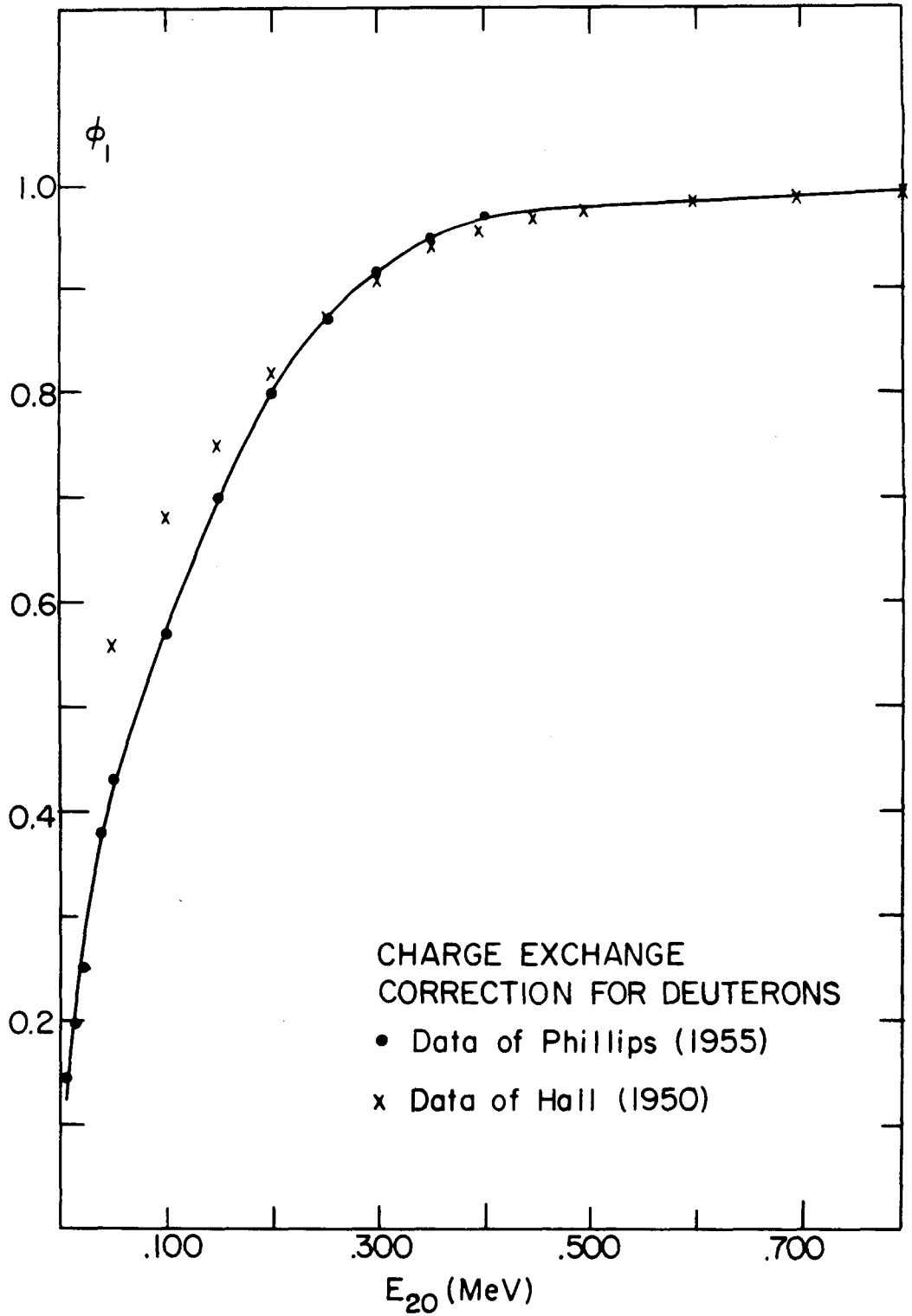


Figure 8

Charge Exchange Correction for Deuterons

The charge equilibrium ratios measured by Hall (1950), and Phillips (1955) are plotted as a function of the outgoing deuteron energy E_{20} . The quantity ϕ_1 represents the ratio of positively charged particles to the total number of particles in the exit beam. The data shown for Phillips is that measured for old surfaces or "dirt". See text p. 32.

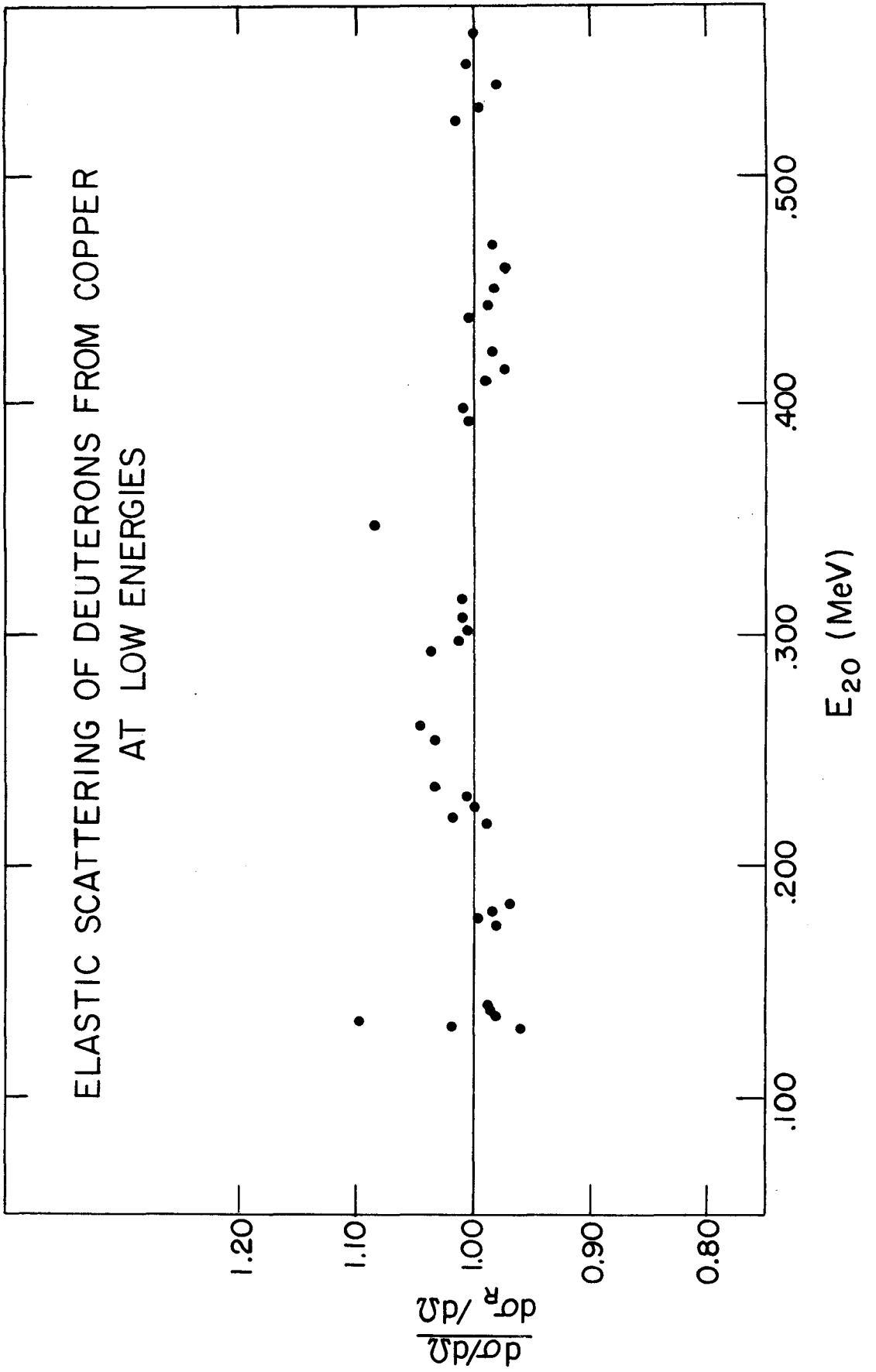


Figure 9

Elastic Scattering of Deuterons
from Copper at Low Energies

The ratio of the measured cross section, after correction for atomic screening and charge exchange, to the Rutherford cross section is shown for scattered deuterons with energies less than 0.600 Mev. The average and standard deviation of the data is 1.003 and 3%. The values used for the charge exchange ratios were those of Phillips (1955) shown in figure 8. See text pp. 33, 34, 73.

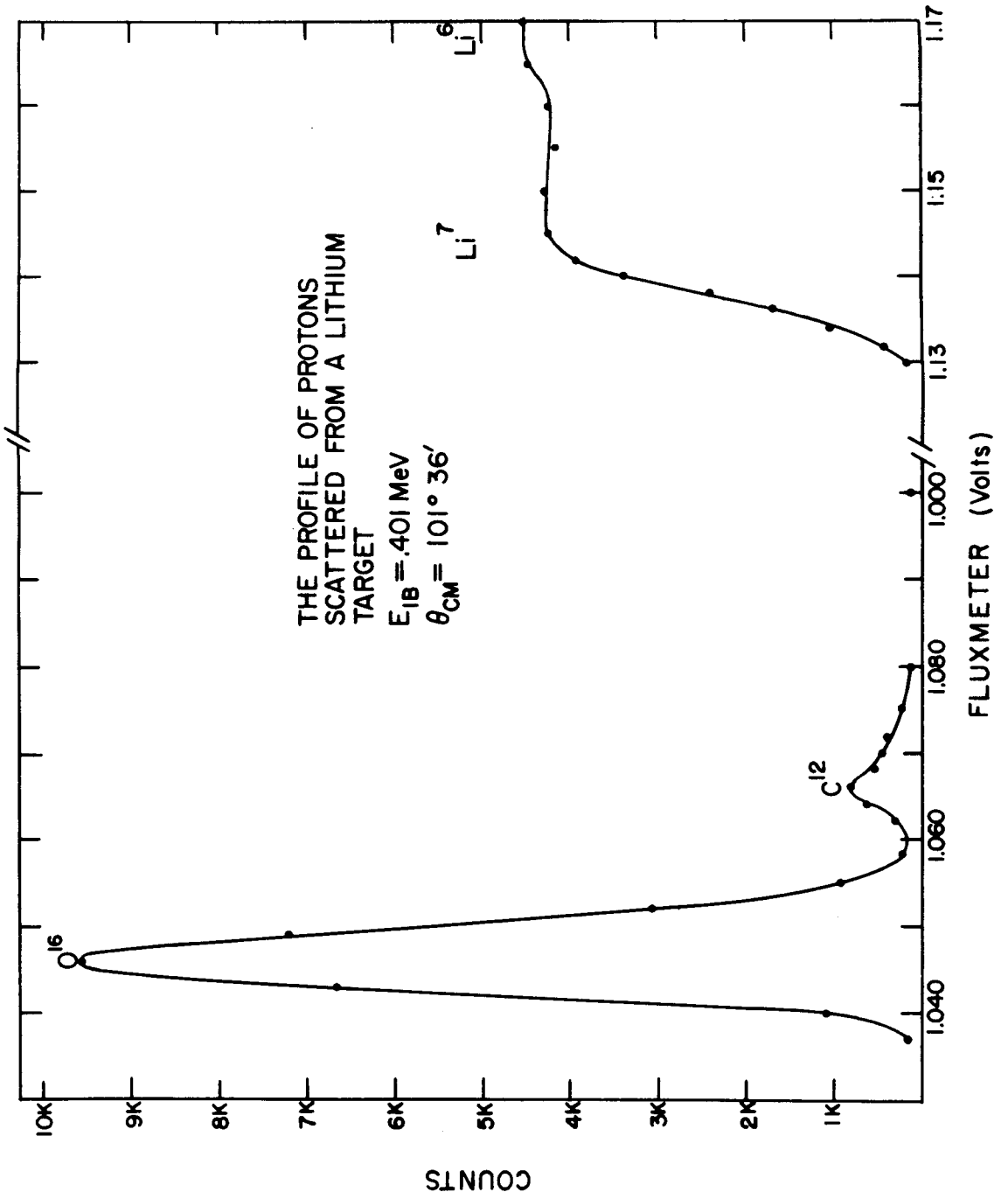


Figure 10

The Profile of Protons Scattered
from a Lithium Target

This profile taken by scattering protons from a thick target of natural lithium at an incident energy of 0.401 Mev is typical of the profiles measured during the course of each experimental run to determine the condition of the lithium target. The position of the particle groups scattered from the lithium-6 and -7, as well as from the oxygen-16, and carbon-12 nuclei within the target can be seen. Again, as the abscissa represents the magnet fluxmeter setting, the energy of the scattered particles increases to the left. The oxygen peak of this profile was used to estimate the distribution of oxygen throughout the target, as described in Appendix I. See text pp. 34, 35, 36, 37, 68.

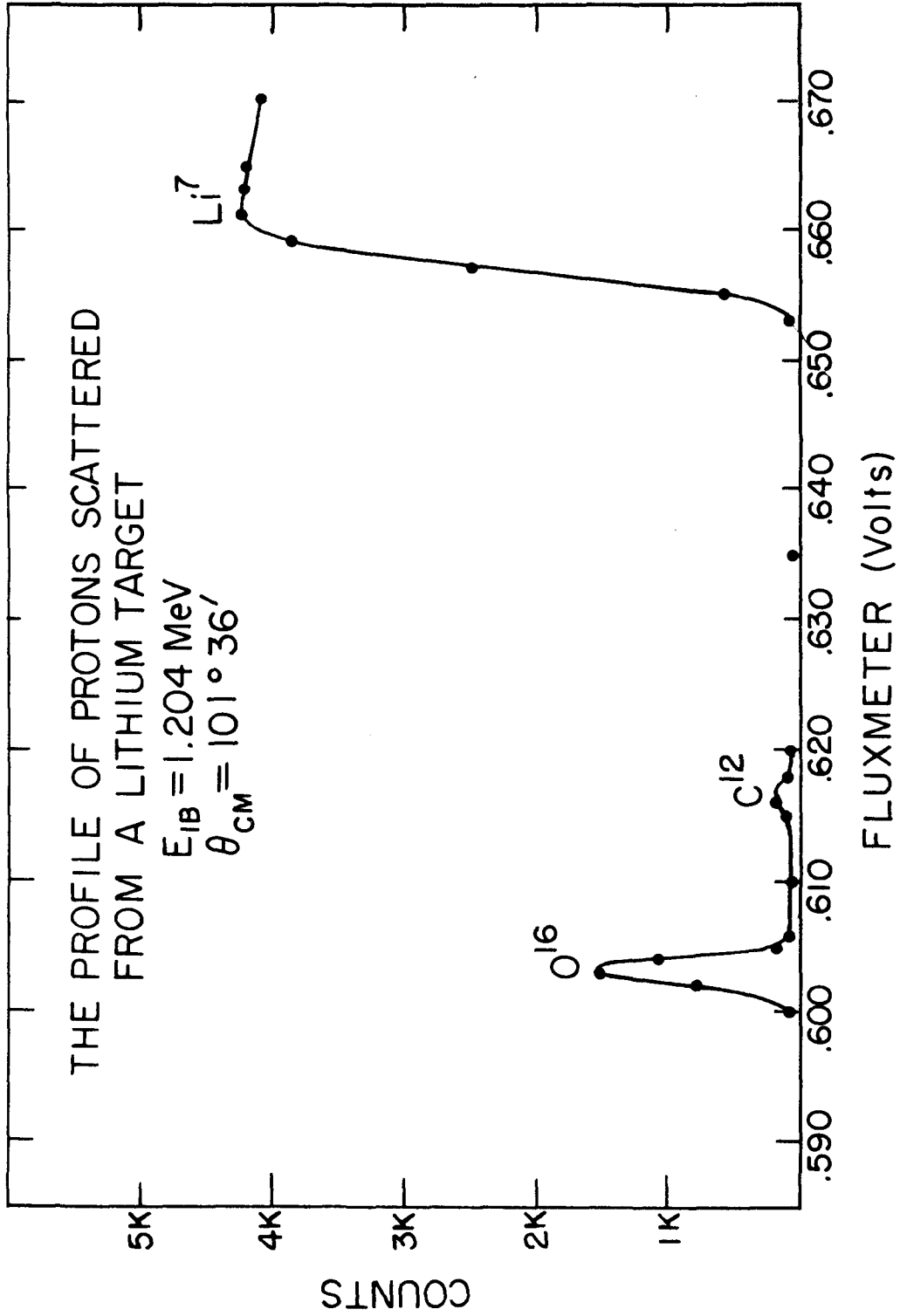


Figure 11

The Profile of Protons Scattered from
a Lithium Target

Here a profile similar to the one presented in figure 10, but at a higher incident proton energy is shown. The strong energy dependence of the height of the O^{16} and C^{12} peaks is seen. The lithium-6 step is not shown, but appears at a higher fluxmeter setting than the lithium-7 step. See text p. 35.

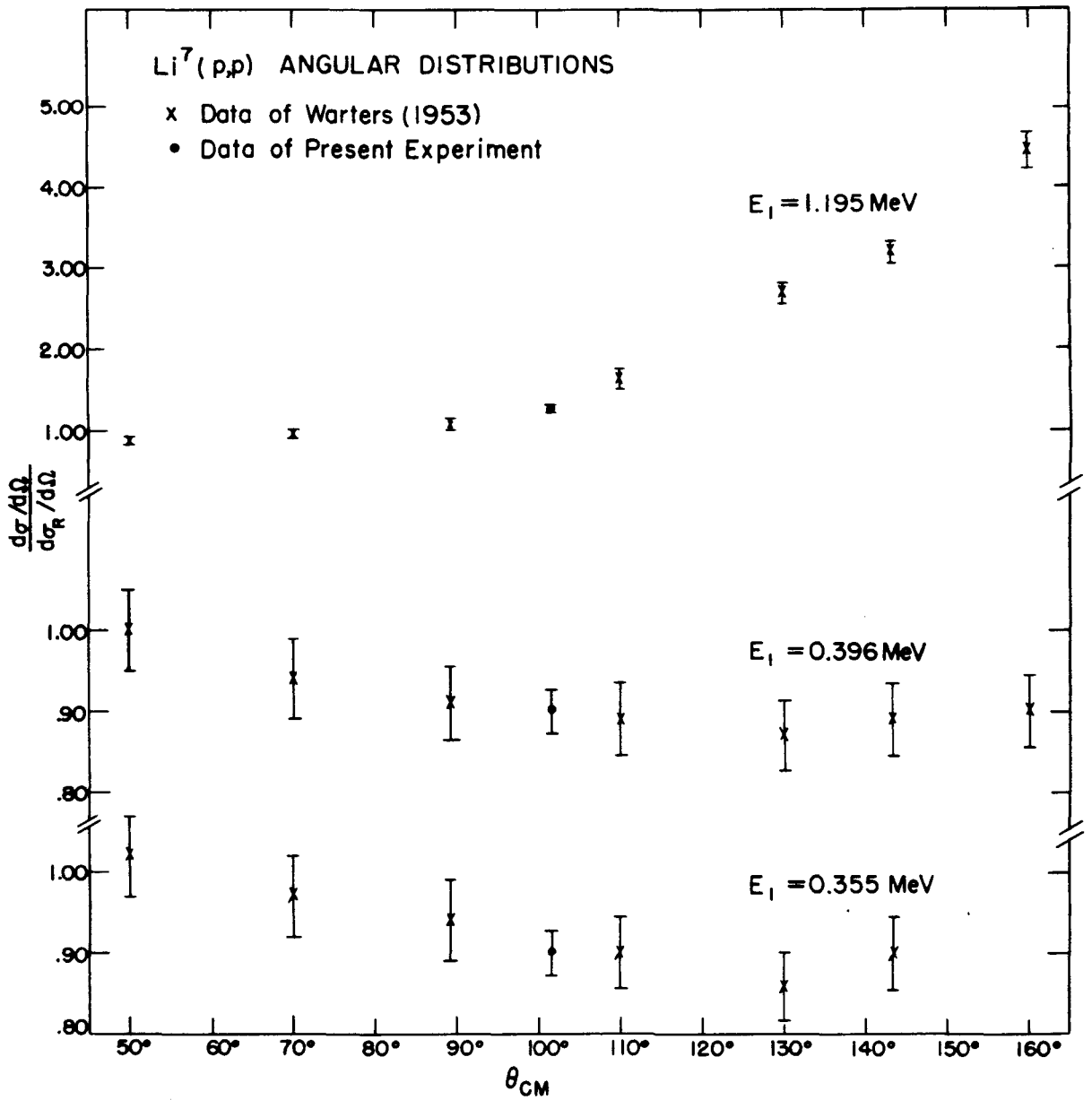


Figure 12

$\text{Li}^7(p,p)$ Angular Distributions

The cross sections obtained from the profiles of figures 10 and 11, as well as at $E_1 = 0.355$ Mev are shown plotted on the angular distributions measured by Warters (1953). The errors indicated are the relative errors of 5% for Warters' data, and 3% for the present experimental data. The cross sections of Warters have been reduced by 8.7% due to the remeasurement of the stopping cross sections involved. Note the suppressed zero. See text p. 35.

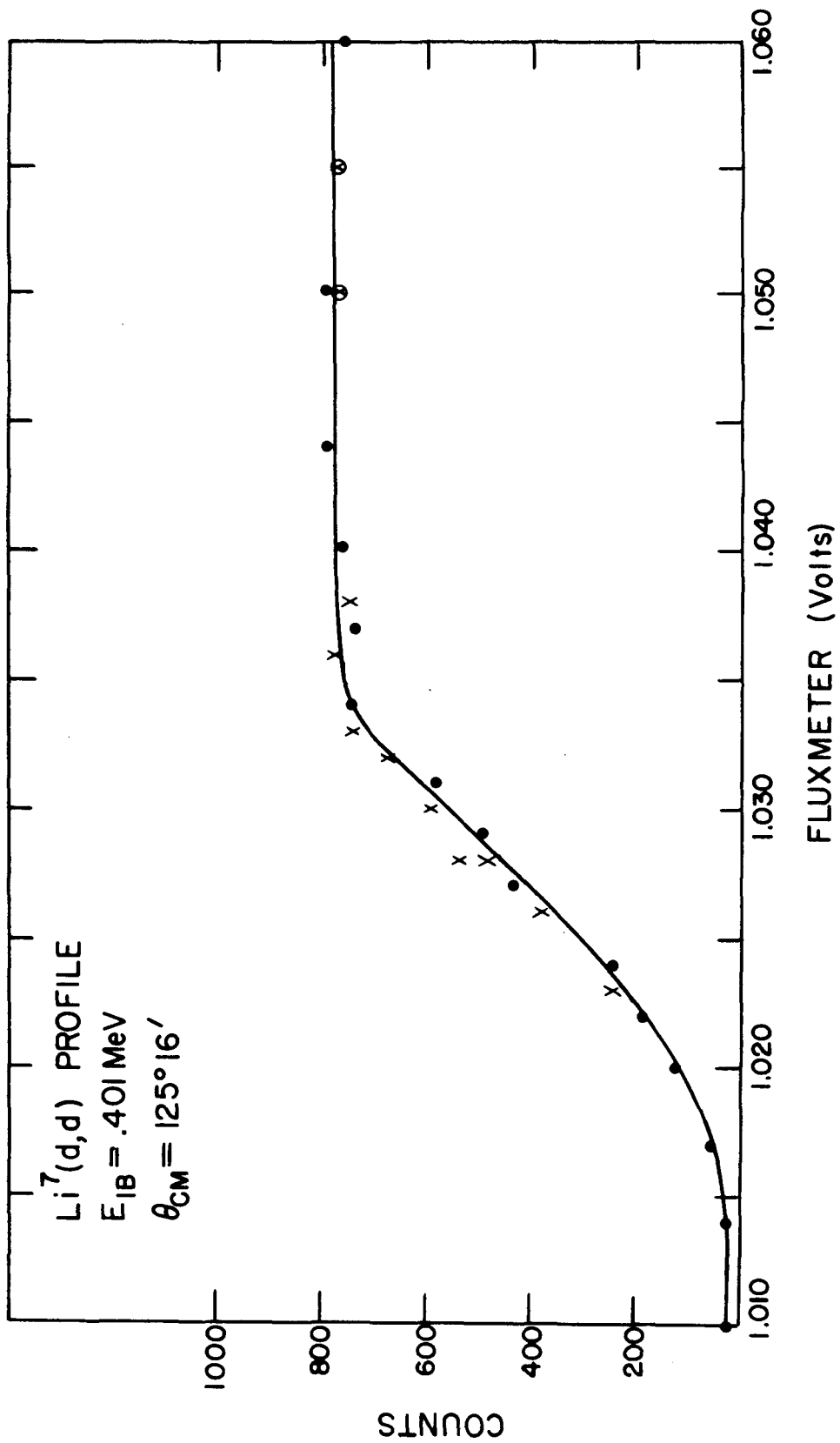
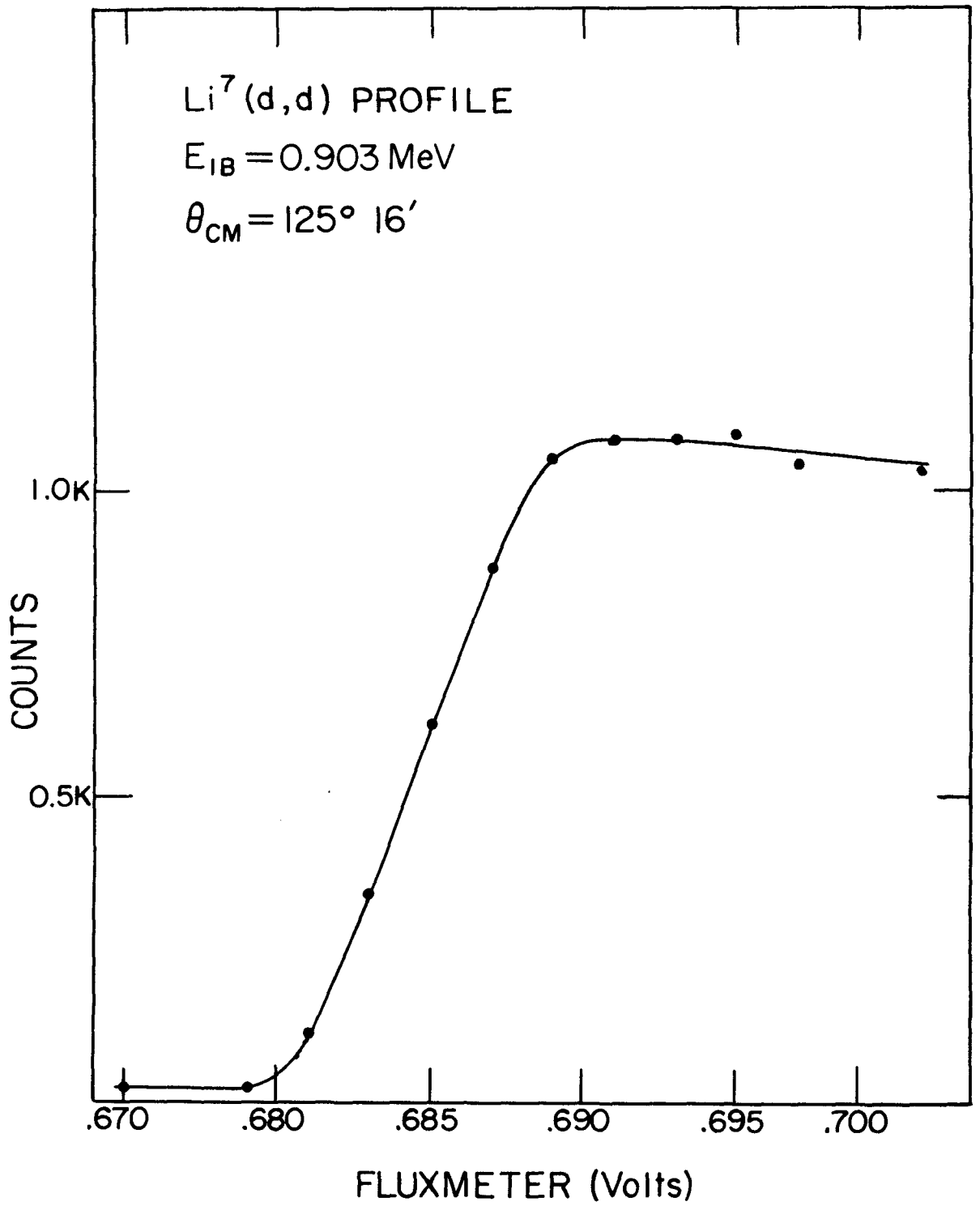


Figure 13

$\text{Li}^7(\text{d}, \text{d})$ Profile

The momentum profile of deuterons elastically scattered from lithium-7 nuclei as measured at an incident deuteron energy of 0.401 Mev. The various symbols on the plot represent different target spots. The lithium-6 step occurs at a higher fluxmeter setting than plotted in the figure. See text p. 35.



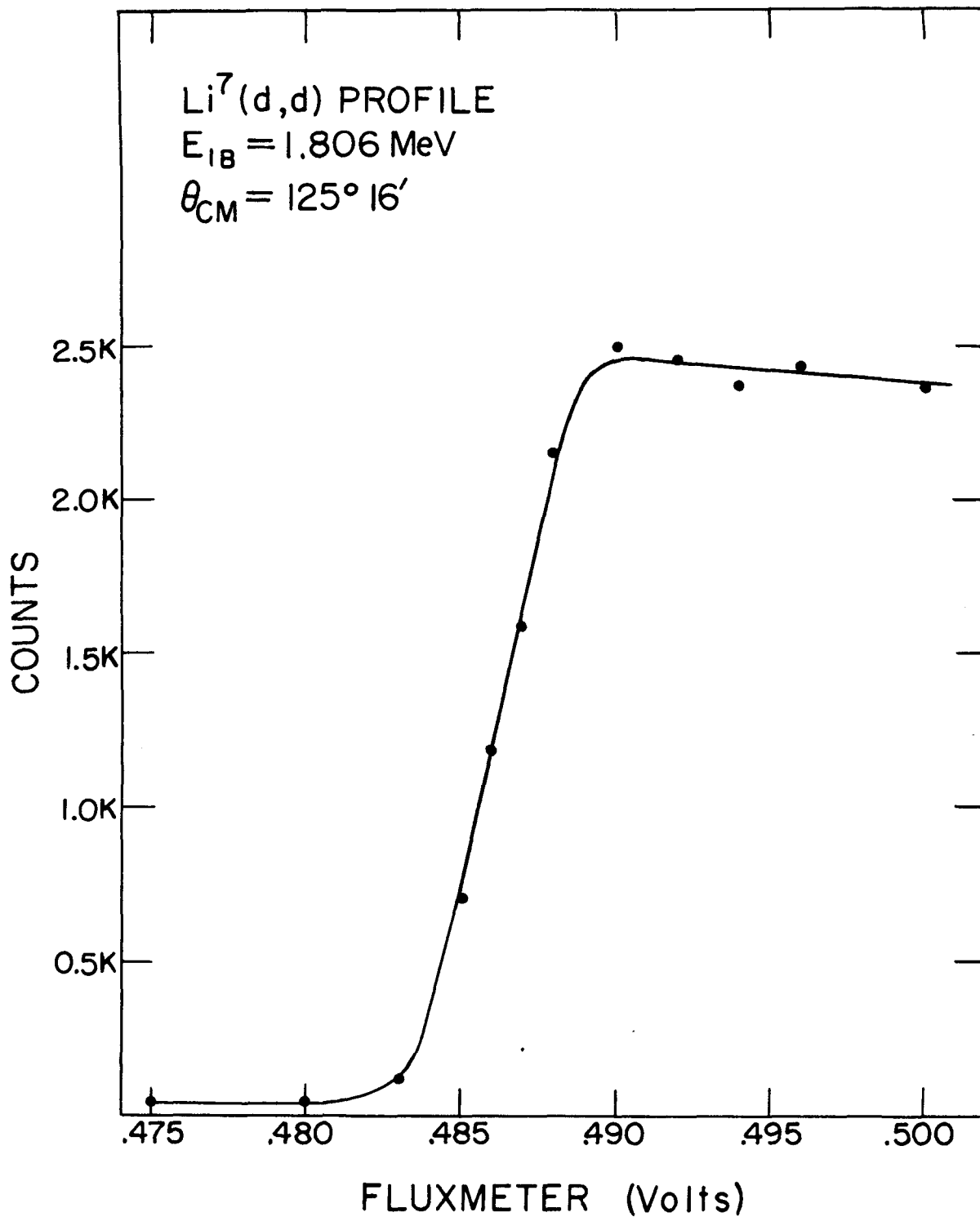


Figure 15

$\text{Li}^7(d,d)$ Profile

This $\text{Li}^7(d,d)$ Profile was measured at the highest bombarding energy at which data was obtained during the present experiment. Care had to be taken in the production of targets at the higher energies to insure that they were sufficiently thick. See text p. 35.

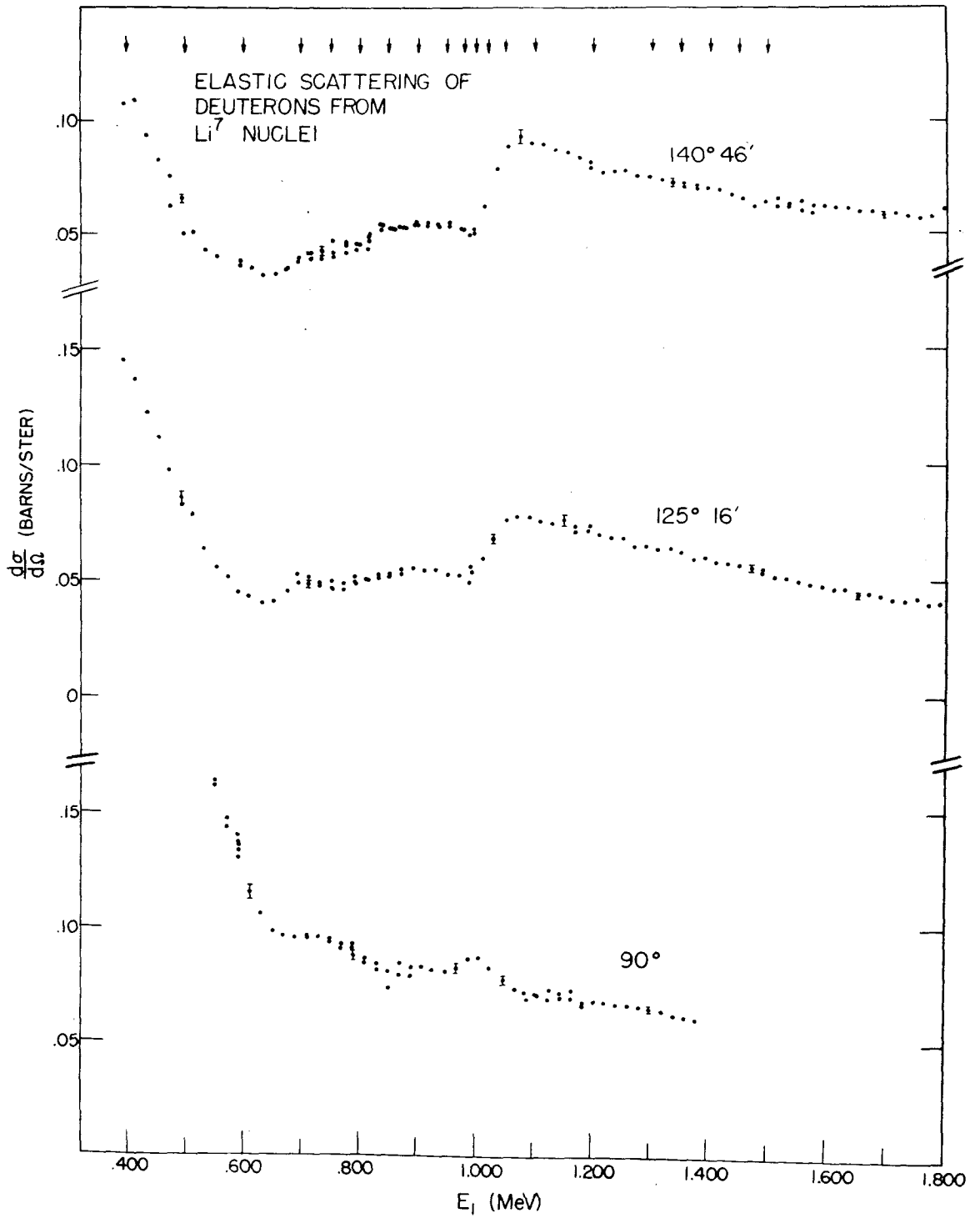


Figure 16

The $\text{Li}^7(d,d)$ Excitation Functions

The excitation functions were measured as a function of the deuteron energy in the laboratory system at the angles corresponding to the zeros of the second, third, and fourth Legendre Polynomials. The relative error shown is of the order of 3%. The symmetric nature of the cross section near one Mev at 90° is to be noted. The arrows indicate the energies at which the angular distributions were taken. See text pp. 40, 56.

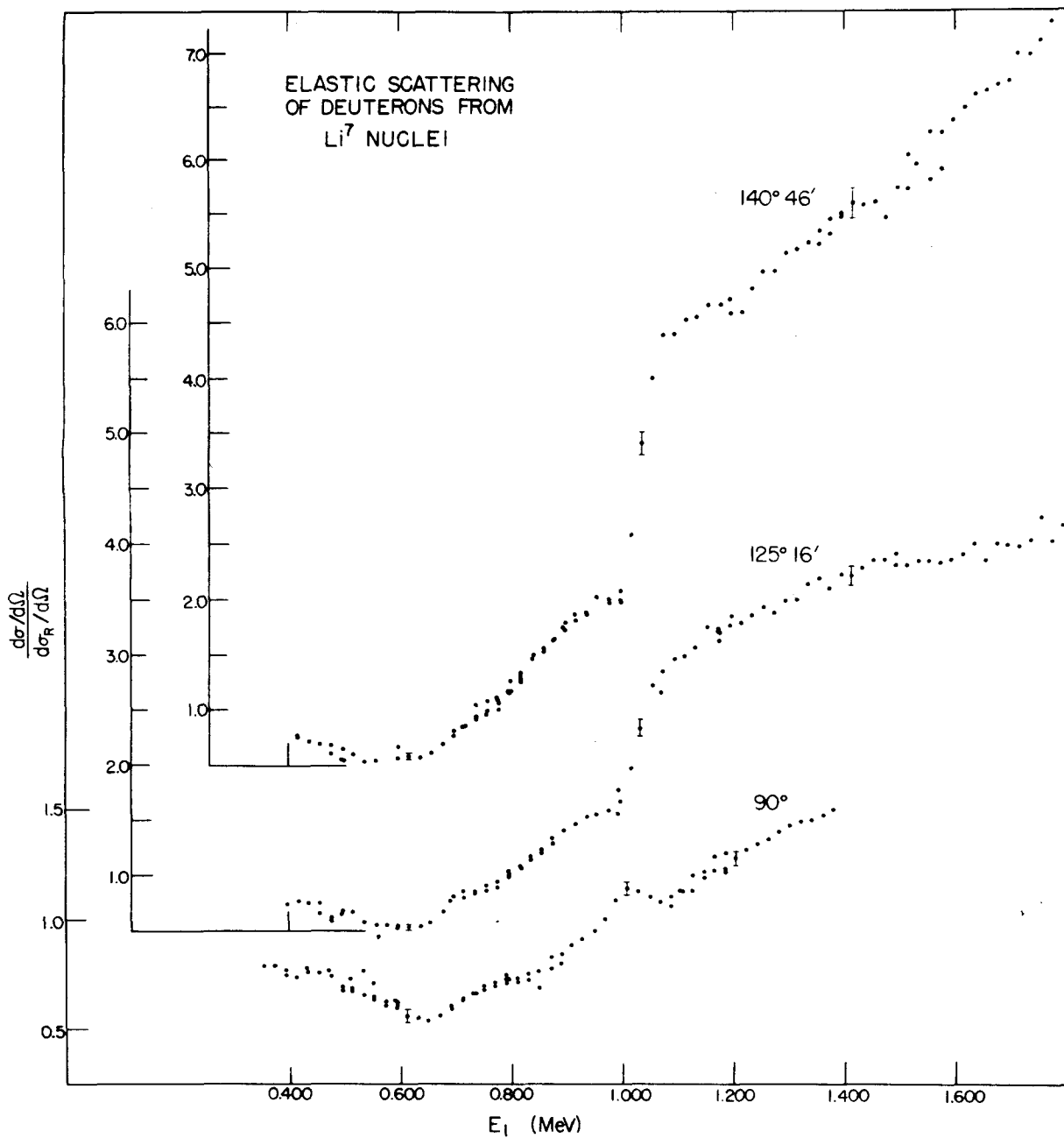


Figure 17

The Ratio of the Excitation Functions
to the Rutherford Cross Section

The ratios of the differential scattering cross sections to the Rutherford cross sections illustrate the large magnitude of the non-Coulomb scattering occurring above one Mev. The error indicated is again the relative error. As with figure 16 nothing conspicuous appears at 0.8 or 1.4 Mev, although there is a strong anomaly near one Mev. Note the suppressed zero. See text pp. 41, 56, 61.

Li⁷(d,d) ANGULAR DISTRIBUTIONS IN THE REGION OF 0.800MeV

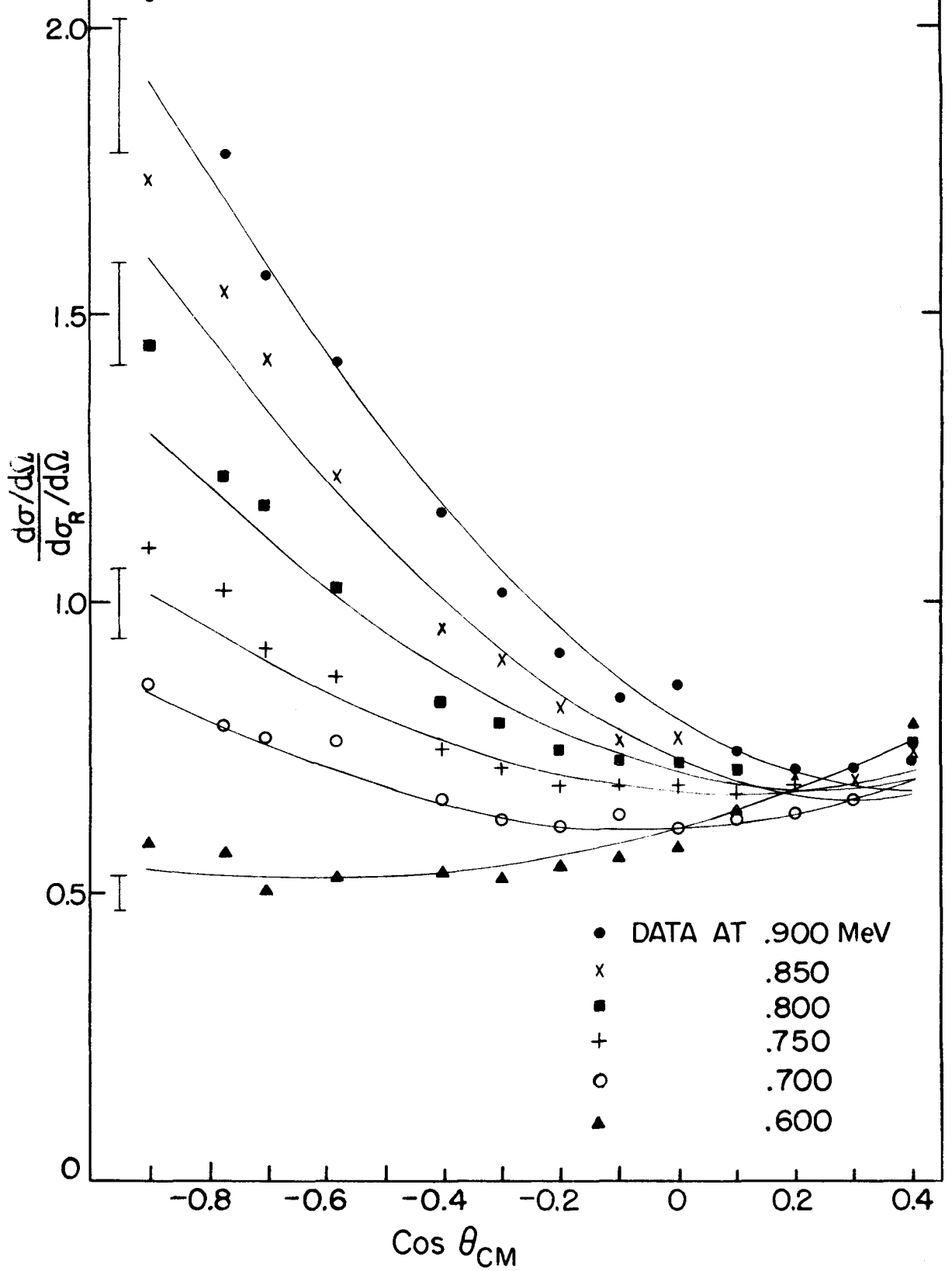


Figure 18

The Angular Distributions
in the Region of 0.800 Mev

The angular distributions passing over the region where the first resonance is observed in the reaction cross sections are presented in figure 18. The points represent the experimental data, while the curves were calculated using the parameters obtained from the s-wave fit discussed in Section IV-4-(b). The error bars represent the estimated absolute error of 6%, and are located at convenient points along the ordinate. The increase in the ratio of the measured cross section to the Rutherford cross section as the energy is increased is to be noted. See text pp. 41, 59.

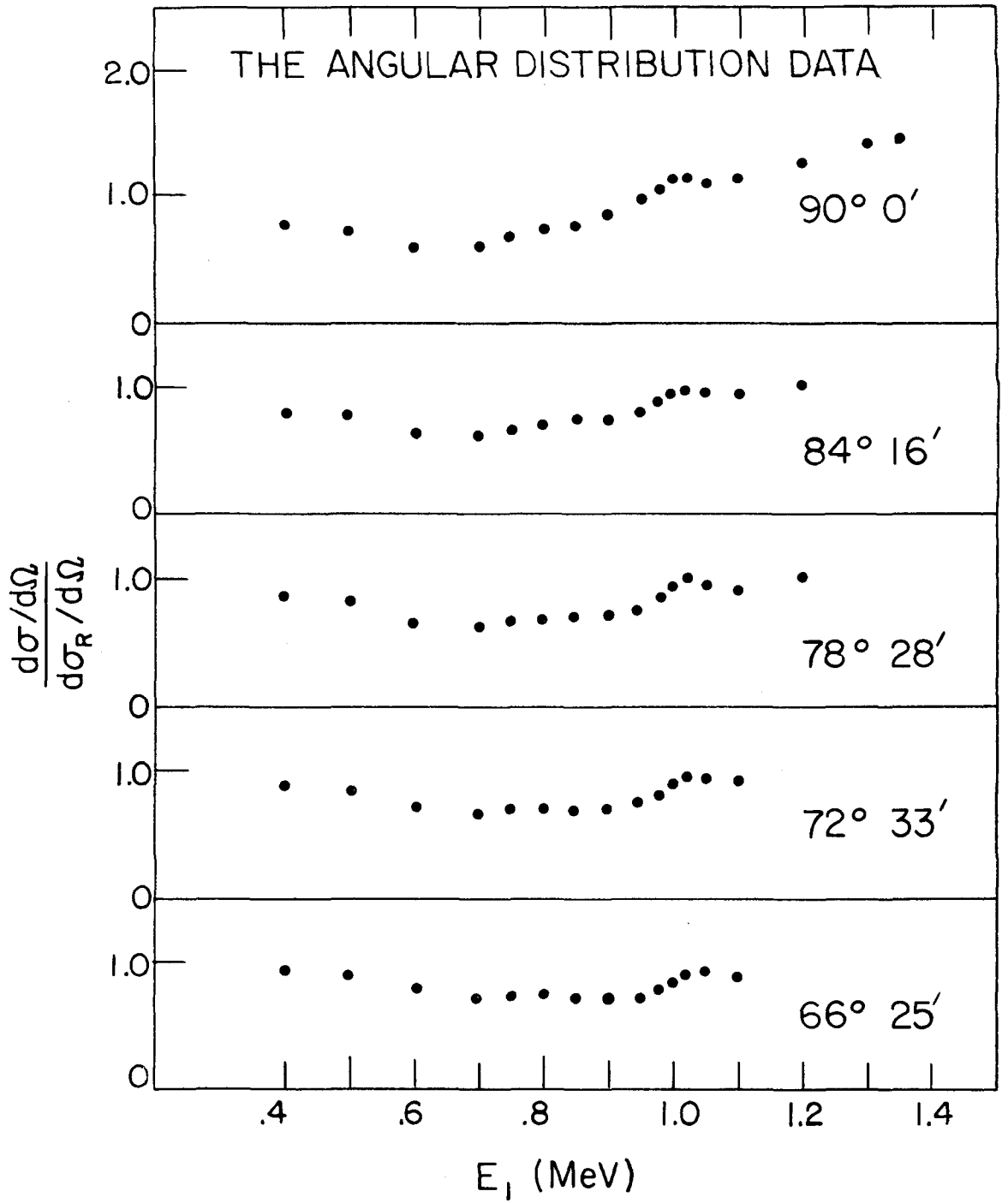


Figure 19

The Angular Distribution Data

The $\text{Li}^7(d,d)$ cross sections which were measured as angular distributions are presented for convenience as excitation functions in figures 19, 20, 21, and 22. The errors indicated in these figures are the relative errors. The progressive modification of the form of the excitation functions as the scattering angle is increased can be observed. In figure 19 the angular distribution data taken over the angles $66^\circ 25'$ in the center-of-mass system to 90° are shown. The points plotted for the angles 90° , $125^\circ 16'$, and $140^\circ 46'$ were obtained from the estimated curve of best fit to the excitation function data of figure 17. See text pp. 41, 57.

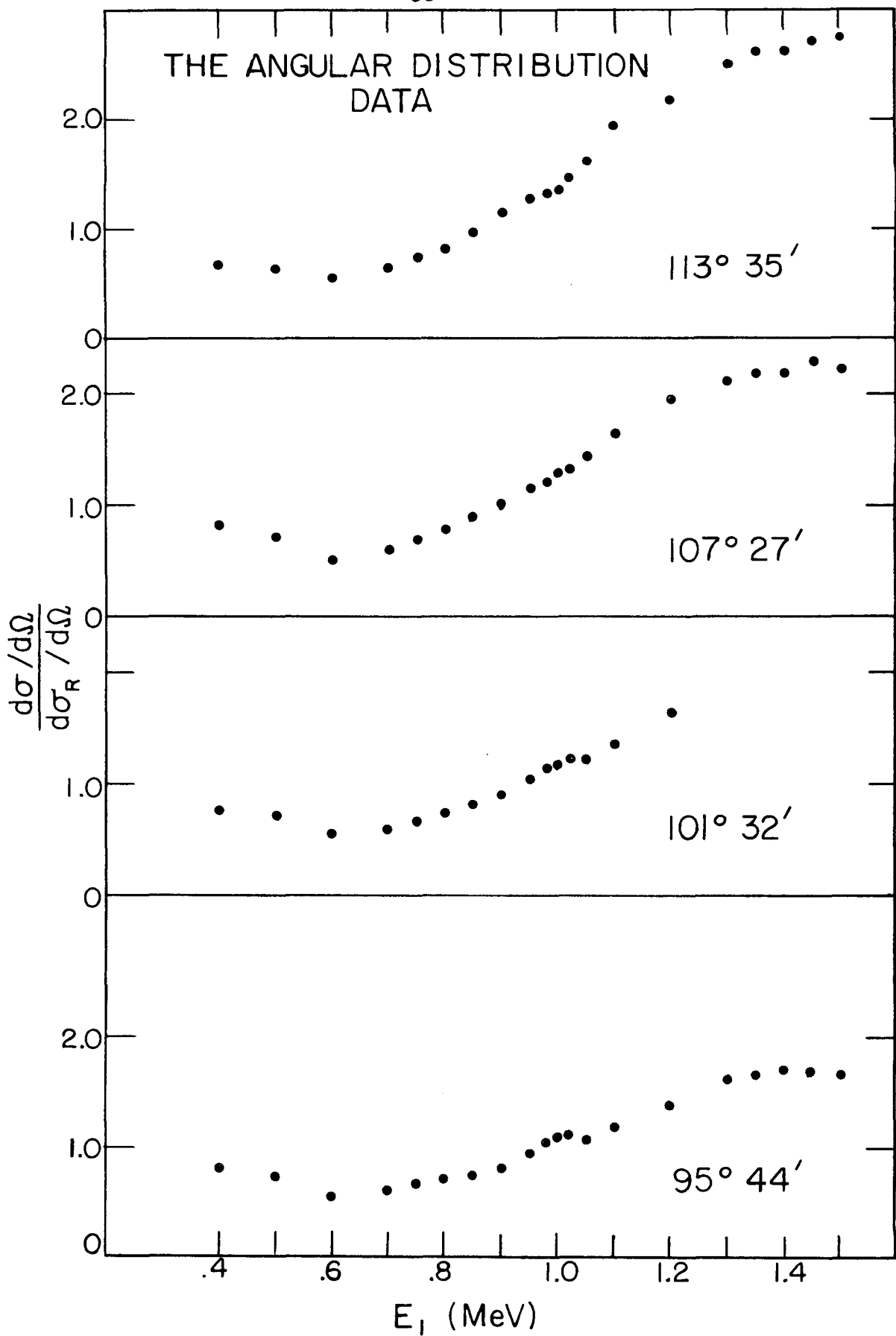


Figure 20

The Angular Distribution Data

The data obtained during the angular distribution measurements over the angles $95^{\circ} 44'$ to $113^{\circ} 35'$ in the center-of-mass system are presented in figure 20. See figure 19, and text pp. 41, 57.

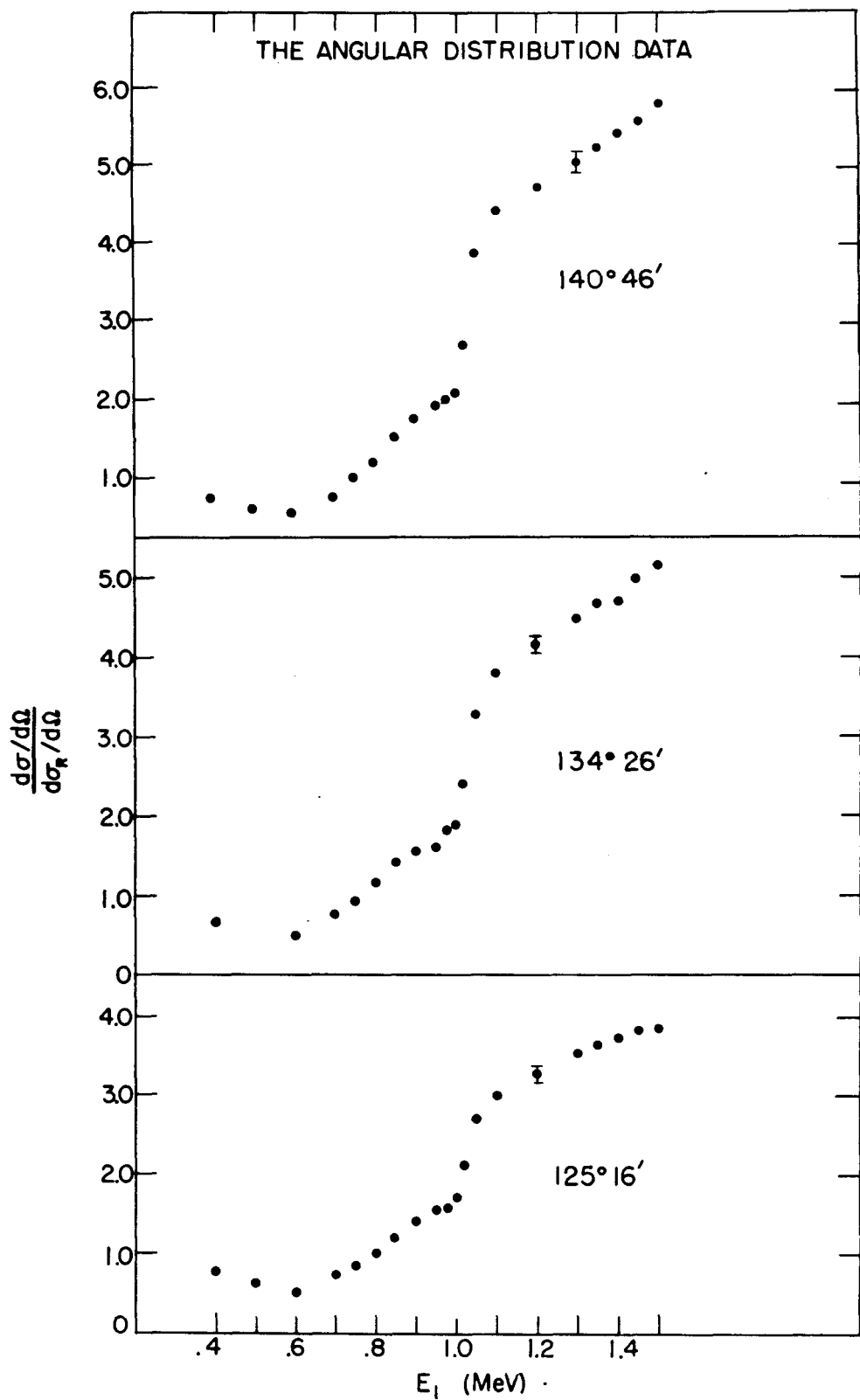


Figure 21

The Angular Distribution Data

The data obtained during the angular distribution measurements over the angles $125^{\circ} 16'$ to $140^{\circ} 46'$ in the center-of-mass system are presented in figure 21. See figure 19, and text pp. 41, 57.

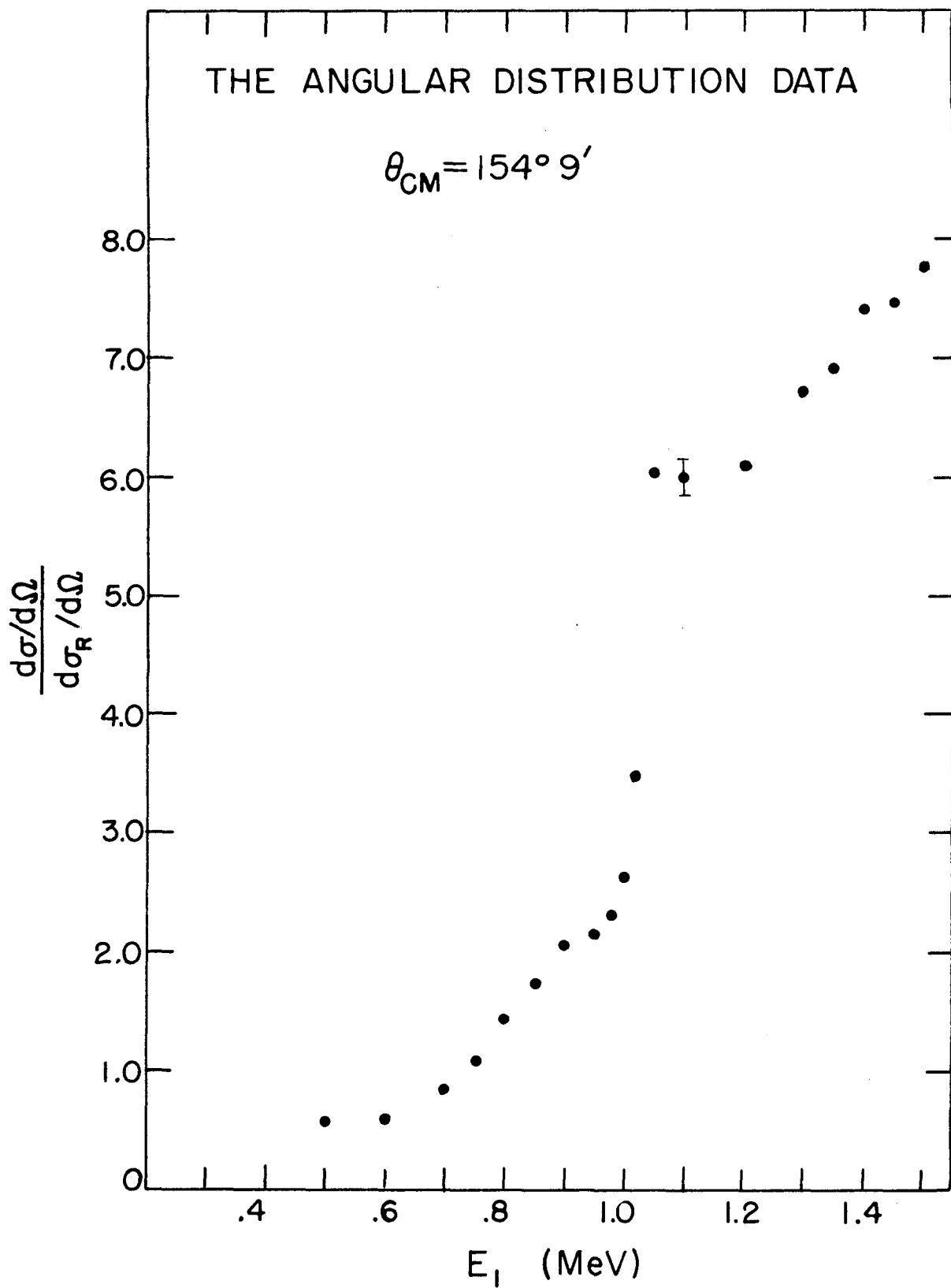


Figure 22

The Angular Distribution Data

The data obtained during the angular distribution measurements at the angle $154^{\circ} 9'$ in the center-of-mass system are presented in figure 22. See figure 19, and text pp. 41, 57.

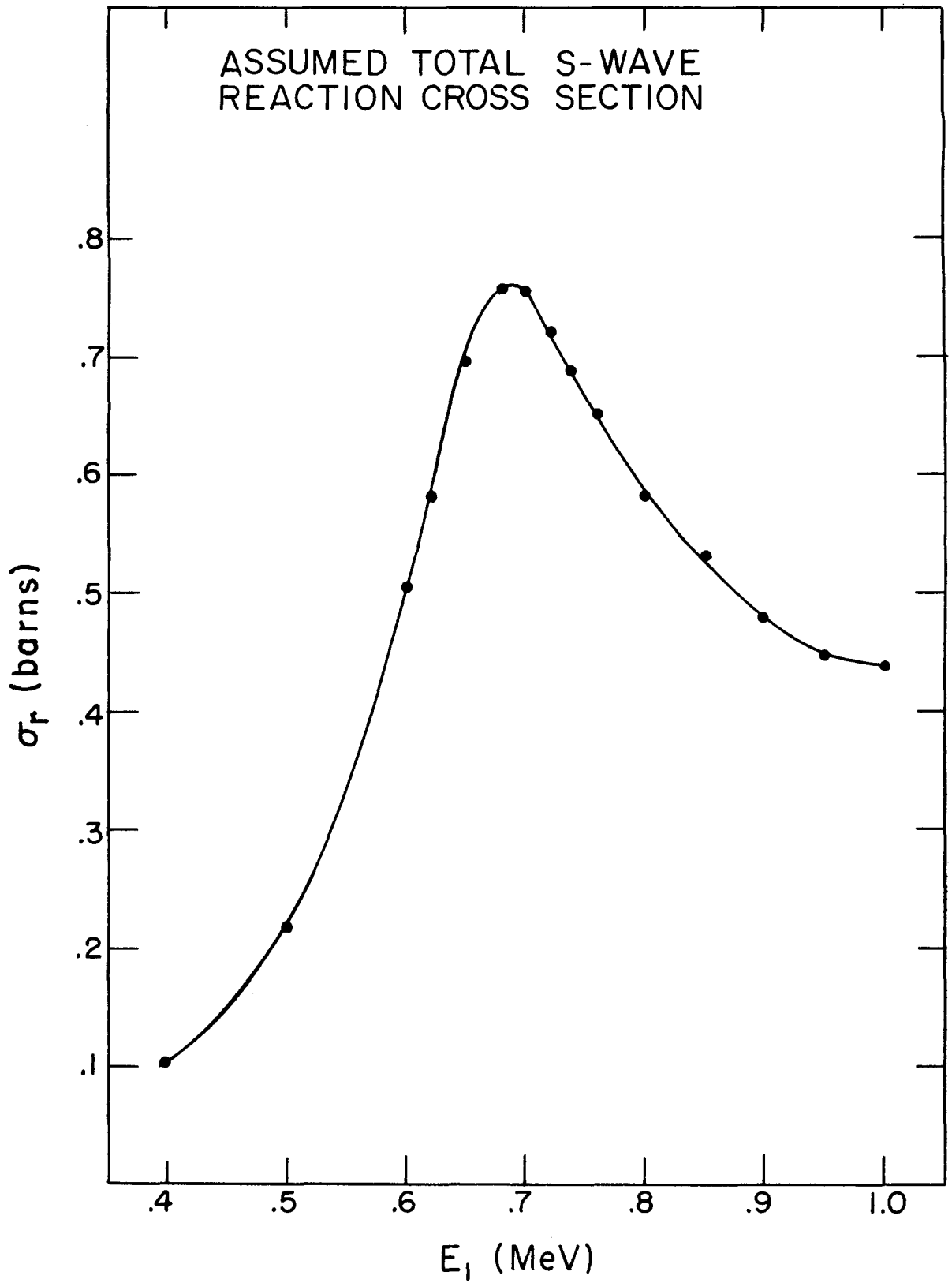


Figure 23

Assumed Total S-Wave

Reaction Cross Section

The total s-wave reaction cross section for deuterons incident on lithium-7 shown in figure 23 was estimated from the reaction data of Baggett and Bame (1952). This estimate was obtained by removing the penetration factors from the measured cross sections about the 0.8 Mev resonance, and symmetrizing the result as explained in Section IV-4-(b). It was necessary to reduce the cross section of figure 23 to obtain a satisfactory s-wave analysis. See text pp. 58, 60.

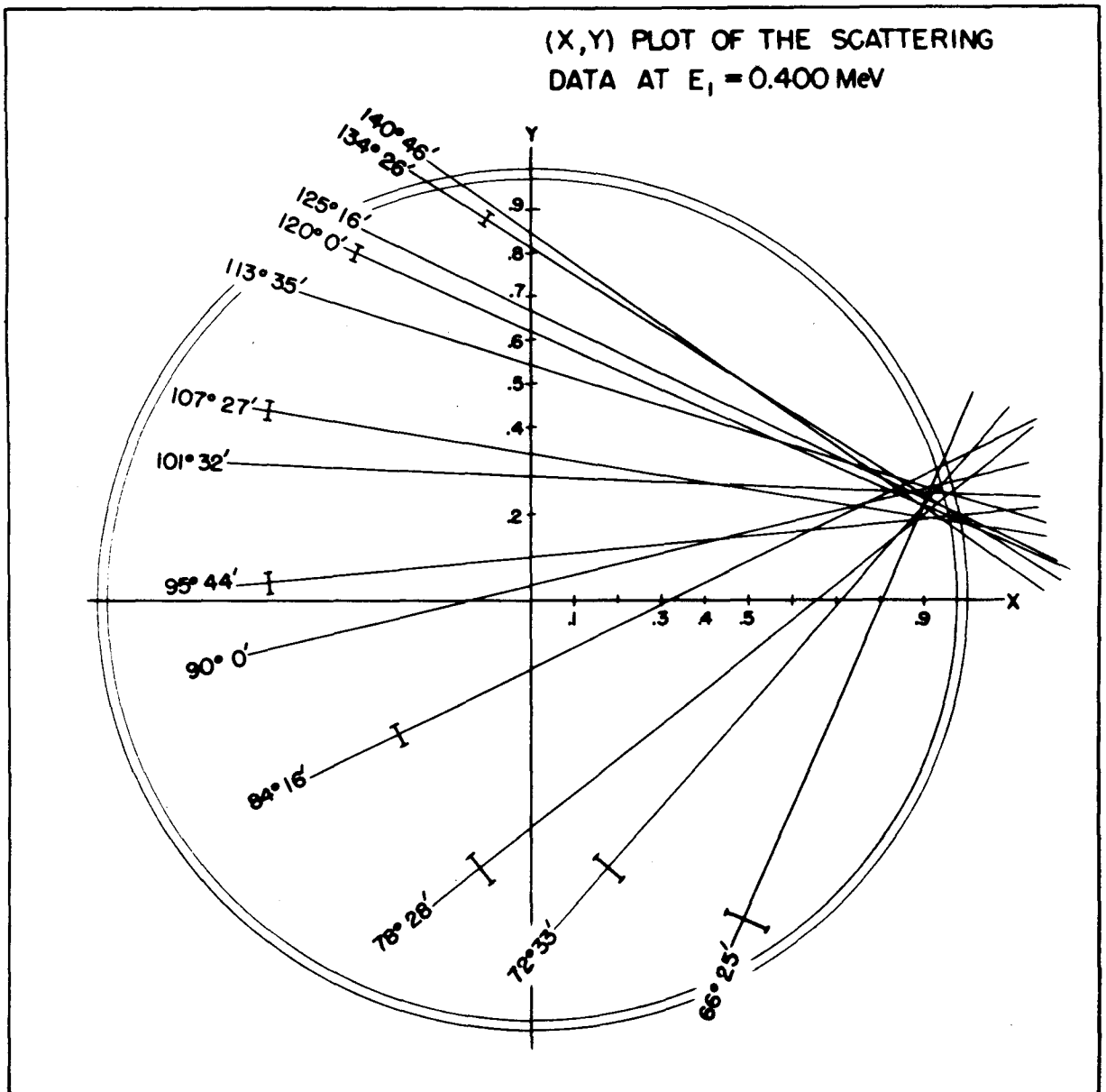


Figure 24

(X, Y) Plot of the Scattering

Data at $E_1 \approx 0.400$ Mev

The value of U used in the s-wave analysis, of the $\text{Li}^7(d, d)$ scattering data, demonstrated in figures 24, 25, 26, and 27 was obtained by multiplying the cross section of figure 23 by five-eighths. In this figure the lines corresponding to the angles comprising the lowest energy angular distribution measured are plotted. The common intersection of the lines was taken as $X \approx 0.91$, $Y \approx 0.24$. This intersection must lie within the inner circle determined by $\sqrt{1-U}$. The error bars are due to the experimental relative error. See text pp. 51, 58.

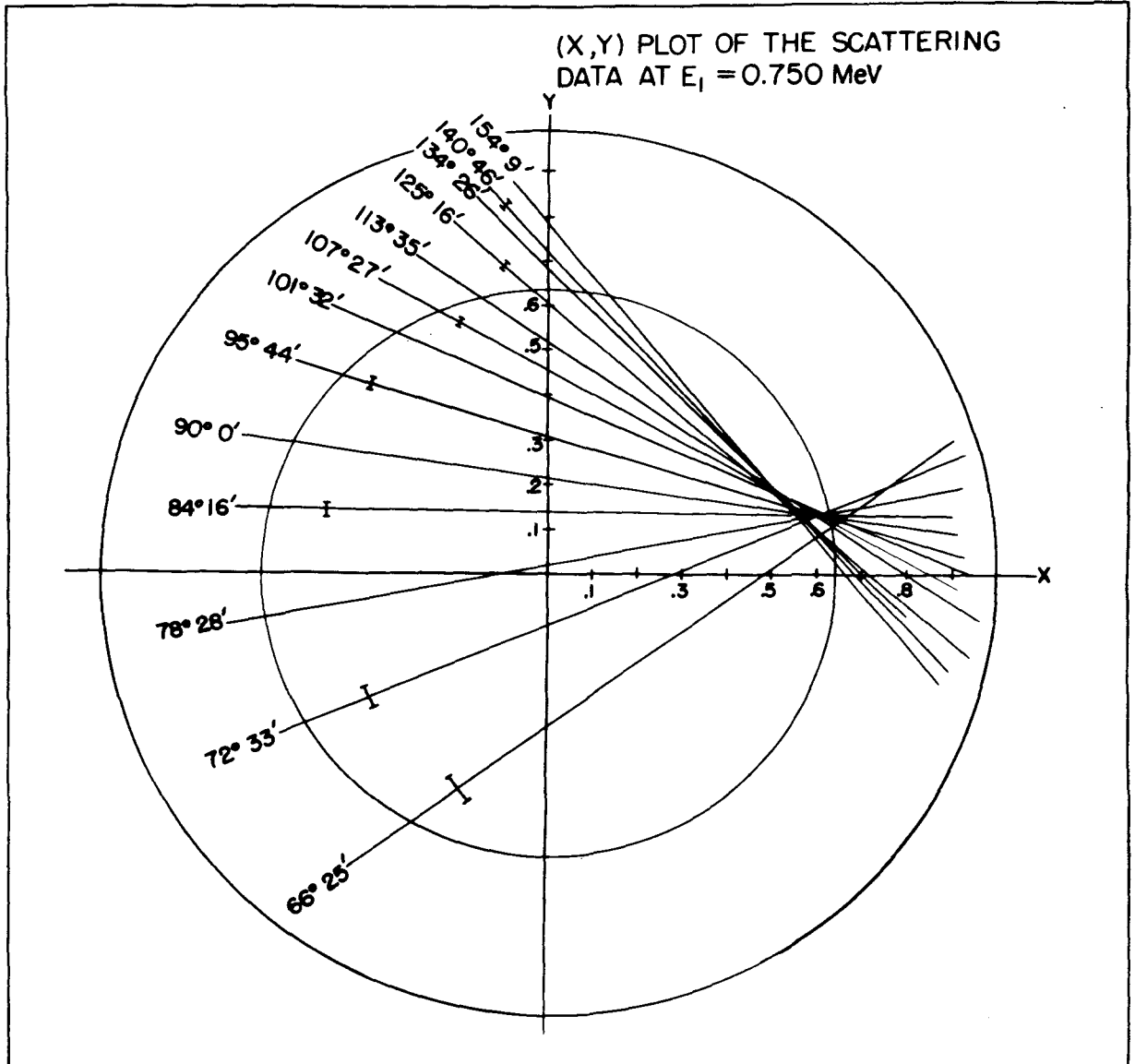


Figure 25

(X, Y) Plot of the Scattering

Data at $E_1 = 0.750$ Mev

The diagram seen here corresponds to an energy approximately that of the first resonance observed in the reaction data. The common intersection was taken as $X = 0.57$, $Y = 0.14$, and lies within the inner circle determined by $\sqrt{1-U}$. See figure 24 and text p. 58.

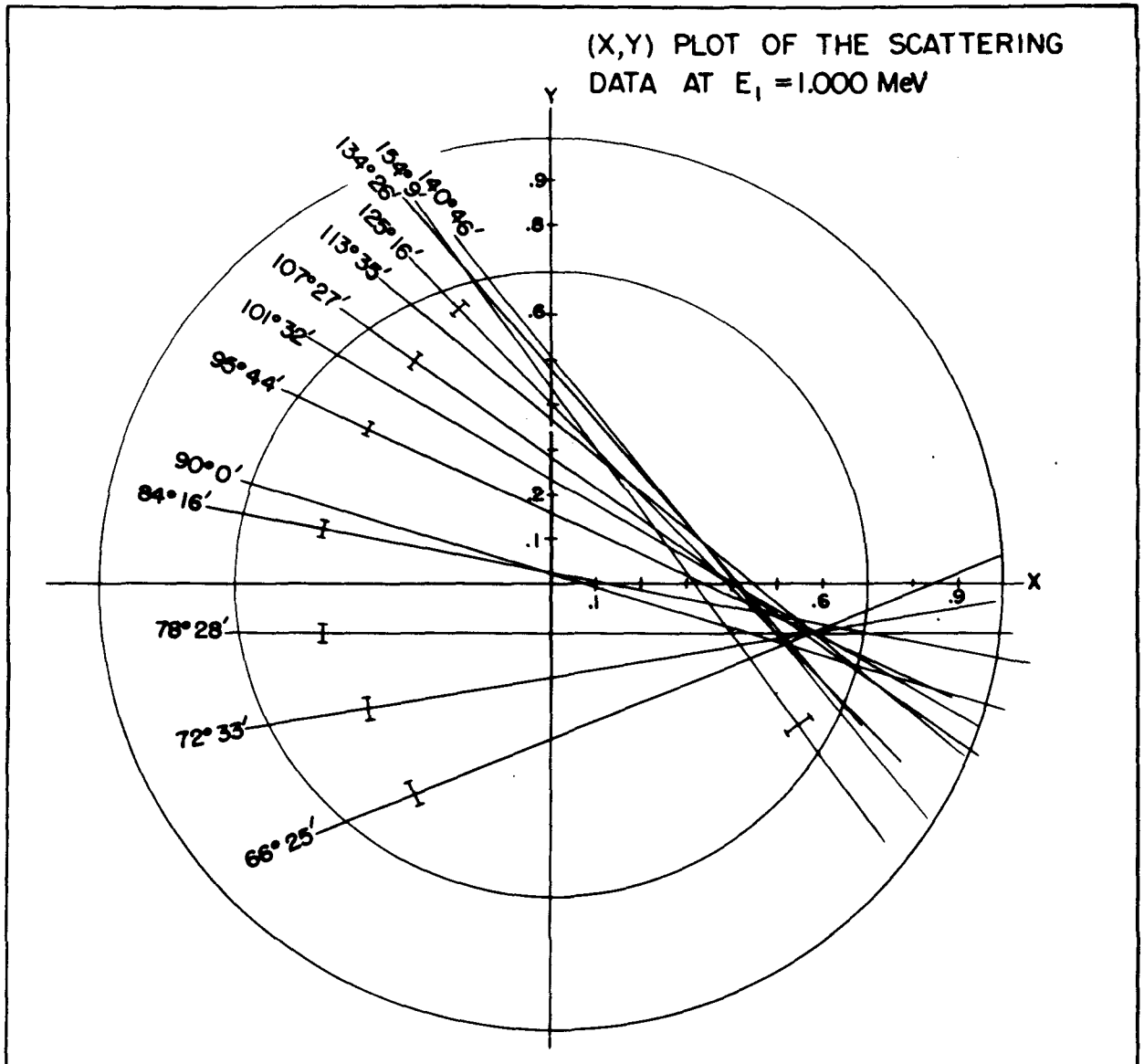


Figure 26

(X, Y) Plot of the Scattering

Data at $E_1 = 1.000$ Mev

The highest energy at which an adequate common intersection of the straight lines determined from the angular distributions could be found, was 1.000 Mev. The pattern formed by the lines suggests that the presence of the anomaly just above one Mev is being felt at this energy. Above one Mev the s-wave fit to the angular distribution data abruptly fails. The intersection of the 1.000 Mev diagram was taken as $X = 0.50$, $Y = -0.09$. See figure 24, and text pp. 58, 59.

THE ENERGY VARIATION OF THE S-WAVE FITTING PARAMETERS

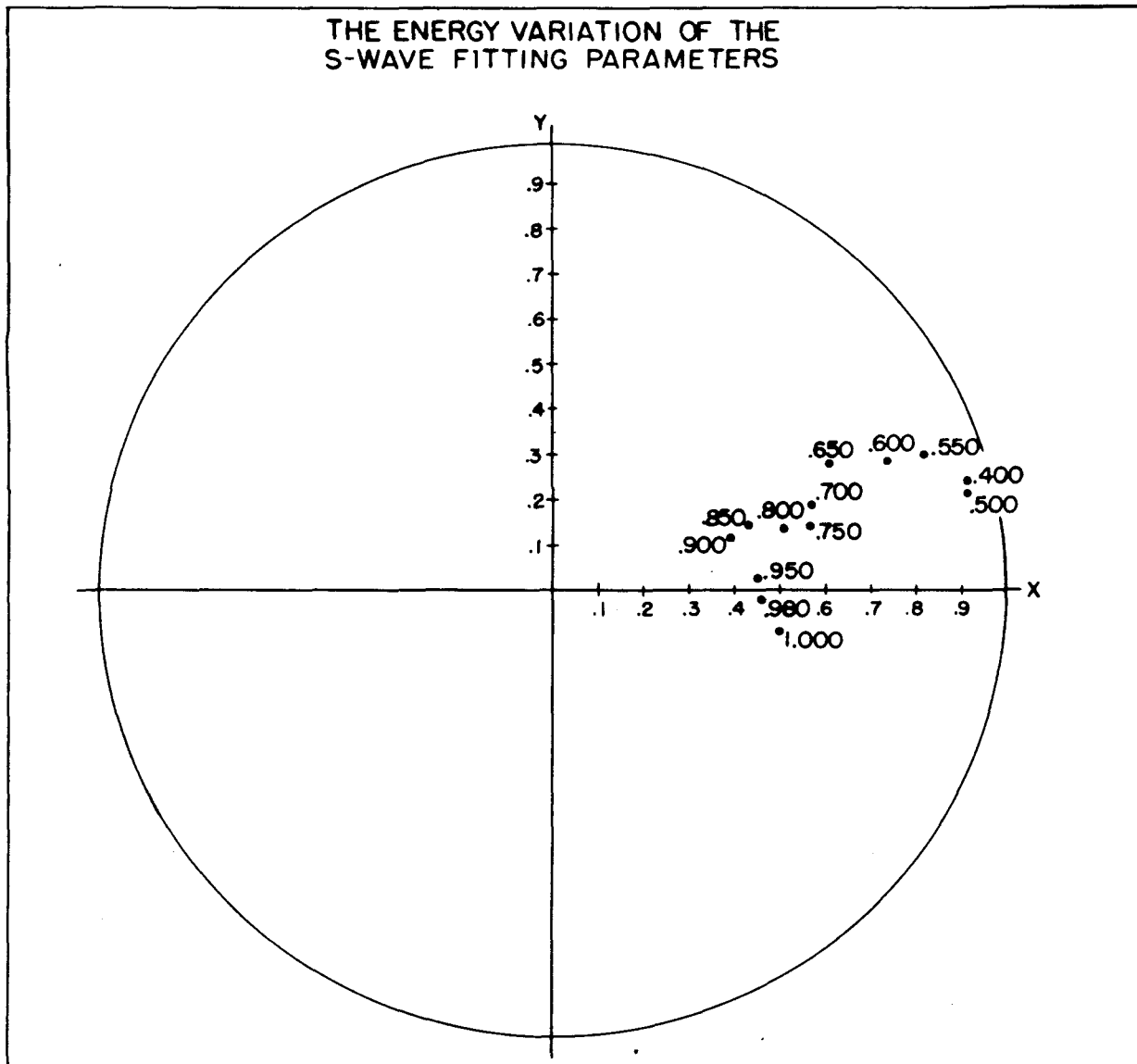


Figure 27

The Energy Variation of the
S-Wave Fitting Parameters

The energy variation in the (X, Y) plane of the points of common intersection is seen in figure 27, for the choice of the total s-wave reaction cross section discussed in figure 24. The energy at which each angular distribution was measured is shown next to the point (X, Y) in the diagram. The points at the energies 0.400, 0.750, and 1.000 Mev were taken from figures 24, 25, and 26. The intersections at 0.550 and 0.650 Mev were obtained from the data of the excitation functions of figure 16 only. Although the plot describes a general counter-clockwise motion in the region of 0.8 Mev where the first resonance is observed in the reaction data, the energy variation is at least partly determined by the form of the total reaction cross section itself, as seen from equation IV-2.8. See figure 24, and text p. 59.